# INVERSE OPTIMIZATION AND DESIGN OF THERMO-MECHANICAL PROCESSING PATHS FOR IMPROVED FORMABILITY OF MG ALLOYS

A Dissertation by

WAHAZ NASIM

Submitted to the Office of Graduate Studies and Professional Studies of
Texas A&M University
in fulfillment of the requirements for the degree of

DOCTOR OF PHILOSOPHY

| | |
|---|---|
| Committee Chair, | Ibrahim Karaman |
| Committee Members, | Amine A. Benzerga |
| | Jyhwen Wang |
| | Bilal Mansoor |
| | Ricardo A. Lebensohn |
| Head of Department, | Ibrahim Karaman |

May 2021

Major Subject: Materials Science and Engineering

# ABSTRACT

Commercial Mg alloys' demand in aerospace and automotive applications have significantly increased due to its lightweight properties and higher mechanical strength than its aluminum counterparts. Processing Mg alloys into functional grades for industrial use, could reduce our carbon footprint by increasing the fuel efficiency of all modes of transportation. However, Mg alloys' use in such applications is hindered by the lack of formability due to its lack of active slip systems at room temperature and increased twinning effects that promotes tension-compression yield asymmetry for the material. Therefore, forming Mg alloys into complex geometrical shapes such as a car bumpers, can lead to premature failures of the material at room temperature during forming.

Multiple studies were conducted on Mg alloys to reduce the CRSS difference between basal and non-basal slip systems, but a different approach was considered in this study, instead of mitigating the difference in CRSS, steps were taken to engineer the anisotropy of the material using texture alterations to engineer the formability of these alloys. Equal Channel Angular Pressing (ECAP) has been used to alter the texture of Mg alloys to maximize formability. A relationship between texture anisotropy to ductility was considered that related Lankford coefficient measurements or R-value measurements to a single invariant parameter called the anisotropy effect on ductility (AED) parameter.

Using AED, we can relate mechanical R-value measurements of ECAP materials to formability. To find the best route with highest formability a novel inverse optimization method was used to automatically derive ECAP routes from the plasticity properties of Mg alloys. The Visco-Plastic Self Consistent (VPSC) crystal plasticity model was used to simulate and predict mechanical properties and textures. New Optimization methods were used to calibrate the model with experimental results which revealed further improvements were required to model ECAP with good accuracy. With the addition of grain fragmentation and Hall-Petch effect to further improve the VPSC crystal plasticity model, texture, and mechanical property predictions after ECAP was conducted at a much higher accuracy than what was

done before. This in turn improved the novel inverse optimization method in predicting new ECAP routes with superior formability.

# ACKNOWLEDGMENTS

First, I would like to acknowledge Dr. Ibrahim Karaman, who has continuously supported me in the professional research field and as a good friend. I will always remember his efforts on my behalf from the countless paper reviews, group meetings and all the networking opportunities he has provided me.

Dr. Amine Benzerga for being my mentor and mechanics teacher who has taught an experimentalist how to think in terms of modelling. I like to credit him for driving home the concept behind everything in my research.

Dr. Jyhwen Wang for his expertise in manufacturing and cup drawing. I hope in the very near future we will have a cup drawing paper done. I hope I have set up the roadwork for future collaborations between our groups.

Dr. Bilal Mansoor for making me feel comfortable and always welcomed, being a good advisor and a friendly professor and all-around cool person through all the professional settings. I have not forgotten my 2 years of High temperature Aluminum work.

Dr. Ricardo Lebensohn for giving me the opportunity of being part of the Los Alamos National Lab family and helping me understand the inner and outer workings of VPSC.

Dr. Miroslav Zecevic, the hidden member of my research dissertation who taught me everything I know about VPSC and its implementation of grain fragmentation in Mg Alloys.

Of course, this work would not be possible with our fantastic MESAM lab group, we were 20 strong at one point during my PhD. Special thank you to Robert Barber for the countless long ECAP sessions and conversations, Michael Elverud for all the help with machining tasks and fixing all lab equipment failures that he had to put of up with. I would also like to acknowledge my close lab group members who had a significant contribution to this research in terms of experimental and simulation help and understanding.

Ebubekir Dogan and Nick Barta for being my sub advisors when I first started my PhD. Abhinav Srivastava, Matthew Vaughan, and Sezer Picak for working with me on multiple projects and collaborations between the three of us on both Mg and High entropy alloys. Jahanzaib Malik, Dinc Erdeniz and Dr. David Dunand for helping me with the Novel High temperature Aluminum Project that never made it into this thesis unfortunately. Daniel Salas and Tejas Umale for always being there when I needed some odd job help here and there that added up over time. Hande Ozcan and Taymaz Jozaghi for being the best advice giver I needed for emotional support and work etiquette for the last 5 years.

I understand I am missing a lot of people here but there are more than 20 of you but I appreciate all the help you have given me and will not forget any of you. Our group is one of the best communities, families, friends, and colleagues I have ever been a part of. Thank you to every single person who has allowed me to get here. And thank you God.

# CONTRIBUTORS AND FUNDING SOURCES

## Contributors

This work was supervised by the dissertation committee consisting of Ibrahim Karaman of the Materials Science and Engineering Department and Professors, Amine A. Benzerga from Aerospace Engineering Department, Jywhen Wang from Engineering Technology and Industrial Distribution Department and finally Ricardo A. Lebensohn from Los Alamos National Laboratory.

## Funding Sources

Graduate study was supported by a fellowship from Texas A&M University and a dissertation research fellowship from National Science Foundation (CMMI Award No. 1563580). This work was also made possible by National Laboratory Office, Los Alamos National Laboratory and Texas A&M Engineering Experiment Station. Its contents are solely the responsibility of the authors and do not necessarily represent the official views of the National Science Foundation, Texas A&M University, National Laboratory Office and Los Alamos National Laboratory.

TABLE OF CONTENTS

Page

LIST OF FIGURES

Page

LIST OF TABLES

# CHAPTER I

# INTRODUCTION AND LITERATURE REVIEW

## 1.1 Motivation

Mg alloys can be beneficial in automotive and aerospace structural components due to their superior strength to weight ratio compared to conventional aluminum and steel alloys [1-4]. However, most of their applications does require some extent of forming the alloy into parts or frames with varying degrees of geometric complexity. This introduces large anisotropic stresses during the forming operations, along multiple orientations leading to failure of Mg alloys due to the complex play between crystallographic texture, stress state, and available deformation mechanisms [5-8]. Poor formability of Mg alloys prevents its use in simple forming and deep drawing operations at ambient temperatures [9]. For example, in a simple cup drawing process, tangential and radial stresses within the sheet can cause it to wrinkle and ear around the top clamped edge of the cup [9, 10]. During drawing, plastic flow anisotropy of the alloys with strong basal texture can also cause large variations in thickness in the formed cups and can act as nucleation points for fracture as shown in Fig. 1.1 [3, 10-15]

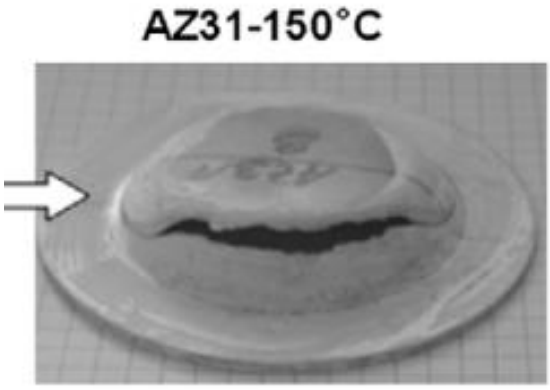


**Figure 1.1: Mg AZ31 Drawing at 150ºC causing failure during the cup drawing process [9]**

This poor formability is extensively due to the lack of active slip systems present at low temperatures (below 200ºC). At room temperature mainly basal slip dominant deformation is observed at due to the differences in critical resolved shear stresses (CRSS) between basal and non-basal slip systems 2which limit the deformation under complex loading systems. The lack of sufficient active deformation systems is amplified due to the strong texture of rolled Mg alloys, tension-compression asymmetry, and high strain hardening caused by the formation of extension and contraction twins in the microstructure [16-20]. The conjunction effect of anisotropic slip and twinning causes orientation dependent mechanical properties with tension-compression asymmetry leading to excessive earing and thinning during forming [21].

Presently, two main approaches to reduce Mg's asymmetric plastic behavior have been proposed. First approach utilizes solute additions in Mg alloys to reduce the difference in CRSS of basal, prismatic and pyramidal slip systems to increase slip activity and improve formability [22]. Alternatively, the second approach utilizes altering the texture of the Mg alloy favoring more orientations that favor slip to accommodate multiaxial deformation during forming [23].

Focusing on texture alterations, various studies have shown better formability by reducing the inherent strong basal texture of rolled Mg alloys [24] [12]. Multiple different rolling and extrusion processes at various temperatures have been used to weaken the basal texture leading to higher drawing values. An inverse correlation was observed between R-values and drawability meaning texture alterations reduced the R-value along the main rolling axes. On the contrary, Agnew et al. showed the opposite correlation where higher R-values showed better cup drawing properties for both Mg AZ31 and rare earth Mg alloys [10].

Forming at elevated temperatures can also greatly improve formability due to the activation of non-basal slip systems. Mg AZ31 normally shows good drawability at temperatures of 150$^{o}$C-300$^{o}$C. Twinning is also suppressed at high temperatures leading to a slip-dominant deformation. The presence of pyramidal slip at high temperatures contributes to dynamic recrystallization along grain boundaries forming necklace like grain structures which can improve formability from the formation of dislocation free recrystallized grains [16]. In one study, simple slow extrusion of pure Mg at 80$^{o}$C produced an equiaxed grain structure that was super-formable at room temperature due to the extensive dynamic recrystallization during drawing and rolling process. It was shown for the pure Mg case higher temperature extrusions lead to larger grain structures leading to the formation of twins during room temperature decreasing the overall formability of pure Mg [25].

Various rolling techniques have also been proven to alter the strong basal texture present in commercial alloys to improve formability. Rolling Mg AZ31B at 450$^{o}$C have shown to improve formability more so than commercial rolling techniques conducted at lower temperatures [26]. Similarly, other rolling techniques such as differential speed rolling on Mg AZ31 at a temperature of 300$^{o}$C was used to move basal poles toward the rolling direction by only 7$^{o}$ which improved formability by 1.5 times [3].

Elevated temperatures can also improve the formability of Mg alloys due to the activation of sufficient non-basal slip systems such as pyramidal slip [27, 28]. AZ31 exhibits good drawability at temperatures between 150$^{o}$C and 300$^{o}$C [9, 14]. Twinning is suppressed at high temperatures leading to a slip-dominant deformation and mitigation of tension-compression asymmetry. Furthermore, the presence of non-basal prismatic or pyramidal slips at high temperatures contributes to dynamic recrystallization along grain boundaries forming dislocation free necklace type grain structures which improve formability [16, 28-30] as shown in Fig. 1.2.

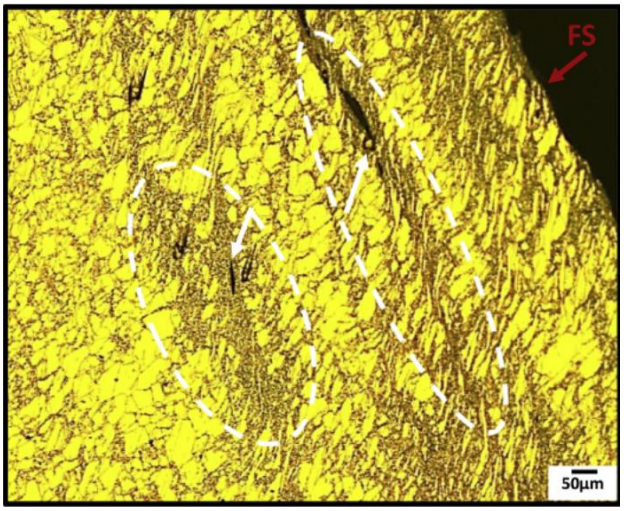


**Figure 1.2: Dynamic recrystallized grain regions (circled) near the fracture surface (FS) after tensile failure at 200$^{o}$C [28]**

In one study, simple slow extrusion of pure Mg at 80$^{o}$C produced a refined micron-range equiaxed grain structure that was formable at room temperature, due mainly to dynamic recrystallization, grain boundary sliding and suppression of twinning and slip [25]. It was also shown that extrusions at temperatures higher than 80$^{o}$C resulted in larger grain sizes, which caused twinning during lower temperature forming, decreasing the formability of pure Mg [25]. Rare-earth containing Mg alloys, in comparison to AZ31, exhibit much better formability at lower

temperatures. For example, somewhat successful cup drawing of Mg ZE10 alloy was possible at 100$^{o}$C [9]. This was mainly due to the diffuse texture of the alloy allowing basal dominant deformation at various orientations.

Controlling twinning deformation during various forming processes provides an alternate method of controlling formability in Mg alloys. Three main forms of twinning systems are observed in Mg alloys: extension ($[10\bar{1}2]$, with the reorientation of 86$^{o}$), contraction ($[10\bar{1}1]$, with the reorientation of 56$^{o}$) and double twinning (extension twins inside contraction twins, with a reorientation of 38$^{o}$) [6, 16-20]. For instance, a rolled Mg AZ31 alloy was pre-twinned prior to Erichsen tests using compressive strains along the rolling direction. This nucleated new basal texture orientations for additional slip directions along the transverse direction which lowered the R-values and improved the drawing height [31]. Similarly, coupling short annealing treatments with pre-twinning were used to reduce the dislocation density which allowed further slip and twinning in these newly formed basal pole orientations, thus enhancing formability [13]. Mg AZ31 alloy with larger grain sizes and more random grain orientations was reported to exhibit better formability due to more grains where slip deformation is favored, leading to a larger work hardening capacity [32]. Thus, it is possible to furnish other processing paths to activate twinning and thus, achieve twinning induced texture randomization in Mg alloys which should improve formability.

Many successful attempts have been made to improve the formability of Mg alloys at room temperature using mechanical processing techniques such as dynamic rolling, ECAP, extrusion, drawing etc. The limitations in improving formability from these processing techniques arise from the lack of knowledge in what type of processing design is needed to maximize formability properties for Mg alloys. An optimization driven method has been proposed that not only predicts

the formability using simulation techniques but is also able to smartly design processing paths using optimization tools that tailor formability. This would greatly reduce the required experimental processing required to produce highly formable Mg alloys.

## 1.2 Research Objectives

To achieve tailored formability for Mg alloys a robust design method needs to be developed to find the limits of Mg formability using available processing techniques. This cannot be achieved with trial-and-error experimental methods that would require multiple tests to find these limits of formability for Mg alloys. Simulation methods such as the Visco-Plastic Self Consistent (VPSC) crystal plasticity model can accurately portray the mechanical response and texture evolution under high plasticity deformation paths which is necessary to predict formability using anisotropy. R-value calculations are also available in VPSC which can be calculated at any iteration of strain increment. To test multiple processing paths various optimization methods, need to be developed to test multiple processing paths in order to tailor the formability.

### 1.2.1 Calibration of the mechanical response in the VPSC model

First the mechanical response in VPSC needs to be calibrated to match experimental properties of rolled Mg AZ31. Experimental tests from various temperatures from 25$^{o}$C to 200$^{o}$C need to be fitted with simulated VPSC results to obtain the correct voce hardening parameters. Due to the anisotropic mechanical behavior of Mg AZ31 various orientations need to be considered to fully calibrate the mechanical responses accurately for each temperature. This should ensure deformation at different orientations activate the correct slip and twinning systems in simulation. Five deformation systems are considered for Mg AZ31, basal, prismatic, pyramidal, extension twinning and contraction twinning. Each of these deformation systems require 4 hardening parameters in VPSC to portray the mechanical response. In total 20 hardening parameters need to

be calibrated. By altering the voce hardening parameters the simulated tensile responses could be fitted to experimental responses. To simplify this process 20 hardening parameters were calibrated using a forward optimization model was developed to minimize the error between the simulated and experimental tensile tests along three different orientations (RD, ND and 45 to ND). The optimization was then repeated for every temperature, 25$^{o}$C, 100$^{o}$C, 150$^{o}$C and 200$^{o}$C, to get a discretized range of voce hardening parameters.

### 1.2.2 Calibration of the Texture response of the VPSC model

Under Objective 1, the mechanical stress-strain responses for 200$^{o}$C were calibrated for rolled Mg AZ31. These voce hardening parameters were then used to simulate ECAP 4 pass routes 4A and 4C. The textures did not show a full agreement with prior experimental texture responses for these respective routes. The evolution of hardening and texture responses are known to be more severe in ECAP than simple tensile testing used for calibration resulting in a discrepancy in texture evolution in ECAP. Firstly, to match the experimental ECAP texture with simulated ECAP texture small changes in prismatic and pyramidal slip CRSS values were required. This allowed good agreement between experimental and simulated texture for 4A and 4C routes.

Later for enhanced texture calibration an optimization tool was used to further calibrate the voce hardening parameters by minimizing the error between experimental and simulated textures for new ECAP routes. This optimization method used Orientation Distribution Functions (ODFs) of the textures to represent the discrete VPSC and experimental XRD texture into a functional form. Further details on this method are mentioned in the Results section.

### 1.2.3 Inverse optimization to develop ECAP routes that maximize formability

An Inverse optimization tool was developed to utilize the calibrated VPSC model from prior objectives. This tool would be able to design ECAP routes at 200$^{o}$C with high AED

parameters (high formability) at room temperature using simulated ECAP plasticity behavior and texture evolution at 200$^{o}$C and tensile plasticity behavior at 25$^{o}$C. In order to control Anisotropy effect on Ductility at 200$^{o}$C the optimization tool would have control over the over the rotation of the alloy between each pass to alter the texture. The texture change would cause the formability to increase or decrease effecting the next iteration step of the optimization. This provides an automated system that would go over hundreds of different route combination before reaching an ECAP route that provides the highest formability parameter.

Two main ECAP rotations were considered to portray two different types of ECAP tools. In ECAP of Mg billets, texture control is given by the rotation implemented along the extrusion direction. The second type of ECAP uses plates and considers rotations along the longitudinal direction and would allow development of sheet metals for deep drawing processes.

### 1.2.4 Experimental verification of inversely optimized ECAP routes

The inverse optimization simulation tool from the prior objective would be used to predict a few routes with a range of formability parameters that can be tested using experimental formability tests. Under the billet optimization tensile samples from five different directions will be taken and strained under strain-controlled test and R-values for each direction will be measured. The formability parameter could then be calculated from the R-value measurements. The experimental textures will also be confirmed and compared to the simulated ECAP textures. Some annealing treatments were considered to improve the formability of these allows further to ensure grain refinement effects are removed from experimental measurements since the current VPSC tool does not consider grain fragmentation or recrystallization.

Please note the next section was part of the original proposal but was not finished during the dissertation but will be continued for future work section of this study.

The second part would consider the inversely optimized plate results with Longitudinal rotation. The plates will then be tested under a constant displacement rate cup drawing setup at room temperature. Forming limit diagrams and anisotropy earing measurements will be made for each route and relationship to AED will be considered. Texture measurements will also be conducted for these routes. This will test the correlation of formability parameter with a proper cup drawing formability tests which has not been done before. Further Finite Element simulations and cup drawing of Mg alloys were also considered using the R-value numbers from predicted simulation results. If the formability parameter theory correlates with cup drawing a powerful FEA simulation tool could be developed to test thinning and warping of geometric parts made from ECAP Magnesium alloys.

### 1.2.5 Implementation of Grain Fragmentation and Hall Petch Model in VPSC

The original VPSC model produced discretized textures that did not match experimental texture results after ECAP. A new grain fragmentation version of the VPSC crystal plasticity code was used to implement the multi slip and twin system of Mg alloy system. The new model used second order stress fluctuation calculations to calculate distributions of misorientation of grains resulting in a more accurate representation of texture. The model was able to use a critical misorientation angle to fragment the grain to portray grain refinement in experimental materials.

Further errors were found where the mechanical properties after ECAP did not evolve in the VPSC model accurately. A custom Hall Petch model was used to relate grain size to the VPSC grain fragmentation predicted mechanical tests to provide a more accurate evolution of formability. This new model was then used to redo the inverse optimization objective to develop novel ECAP routes with maximum formability.

## 1.3 Background and Literature Review

### 1.3.1 Severe Plastic Deformation of Magnesium Alloys

Only one special processing technique was chosen to alter the texture of Mg alloys to engineer anisotropy through texture control. Equal channel angular processing/extrusion (ECAP/ECAE) is a severe plastic deformation (SPD) technique which involves extruding a billet through an angular die creating a large simple shear deformation in the billet as shown in Fig. 1.3 [33-51]. Maximum shear on the billet per pass can be attained by using a $90^{o}$ die angle which accounts to approximately 100% of applied plastic strain on the billet per deformation pass in the die. In between passes, the rotation of the billet along the extrusion direction can be altered (leading to so-called different ECAP routes) to control texture, grain shape and misorientation, and grain refinement level. Many works on ECAP of commercial Mg alloys have been reported to control grain size and alter texture in order to improve formability [16, 23, 52-62].

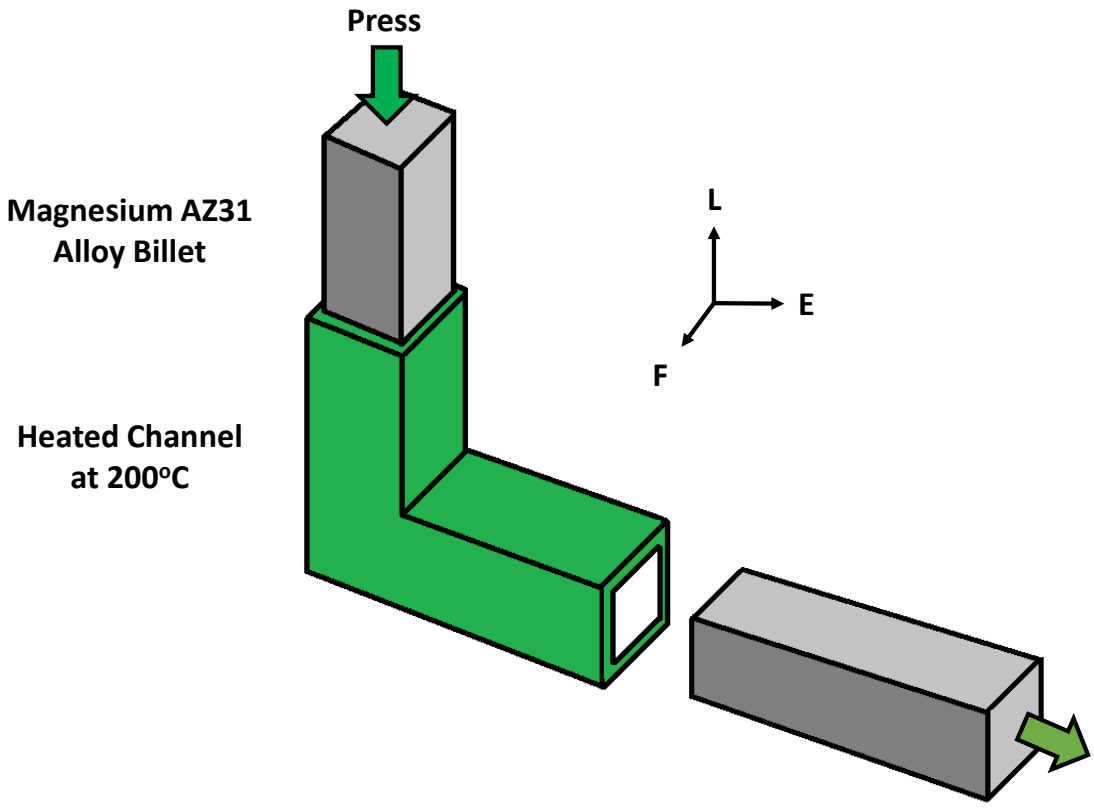


**Figure 1.3: Schematic of Equal Channel Angular Processing (ECAP) with inlet and outlet channels demonstrating the definition of coordinate axes names which are utilized in the present work. E: Extrusion direction, L: Longitudinal direction, F: Flow direction.**

Several ECAP processing routes have been used with variations in temperature and rotation sequence to ensure that strongly textured Mg alloys do not shear band and fracture during processing [16, 58, 63] . Most ECAP work on Mg AZ31 was conducted at temperatures 200°C and above at slow extrusion rates to assure non-basal slip activity and twin suppression [16, 28, 58]. Fast extrusion rates and lower temperatures could lead to extensive shear banding in the ECAP billet leading to failure [16]. ECAP of Mg AZ31 can be conducted at temperatures as low as 115°C if the strong basal texture could be altered through prior processing such as higher temperature rolling or ECAP processing with temperature step down approach [58, 63-65]. ECAP at lower

temperatures in subsequent passes can be achieved using the temperature stepdown method and help develop more equiaxed and finer grain sizes [64, 65].

Few studies have shown various degrees of dynamic recrystallization to occur during ECAP at temperatures above 150$^{o}$C [16, 58, 66]. Initially coarse grain structures after a couple of ECAP passes at 200$^{o}$C develop small necklace like chains of dynamically recrystallized grains along the boundaries of coarser grains leading to a bimodal grain size distribution. Upon further deformation, the grain structure becomes more refined and homogenous, and the coarse grain structure at 4 or more ECAP passes is completely fragmented and recrystallized into 1 to 5 µm range grain size [16, 66]. At temperatures below 200$^{o}$C, sub-grain formation occurs if basal slip activity is more dominant than pyramidal slip leading to more grain refinement [16, 58]. It should be noted in the VPSC crystal plasticity model recrystallization was not portrayed in the current model but will need to be considered for future renditions of the simulation process.

ECAP has been used to improve formability of Mg alloys through texture alterations using ECAP route control [23, 44, 55]. Prior studies have shown that ECAP routes, such as route 4C (180$^{o}$ rotation along the extrusion direction between passes), result in better formability of Mg AZ31 than conventional rolling, confirmed using round notch bar tensile tests [23]. It was shown that a processing approach that targets texture control using ECAP can be suitable for tailoring formability of highly textured Mg alloys.

### 1.3.2 Visco-Plastic Self Consistent (VPSC) Crystal Plasticity Model

The VPSC crystal plasticity formulation, together with the Predominant Twin Reorientation (PTR) scheme in order to keep track of the abrupt changes in crystallographic texture due to deformation twinning, was first developed by Lebensohn and Tomé [67]. The VPSC treats each

grain or twin lamellae as a visco-plastic inclusion embedded in a homogeneous medium representing the polycrystalline aggregate. More details on VPSC and PTR can be found in [67-69]. VPSC has been extensively used to predict mechanical behavior for tension, compression, ECAP, and rolling deformation of Mg alloys [16, 28, 67, 70-75]. VPSC can predict the relative activities of slip and twinning deformation modes in hcp alloys under different processing paths. Most studies on VPSC modeling of Mg alloys have utilized the Voce hardening formulation, presented in Eq. 1.1, along with the PTR scheme to predict the activation of extension, contraction, and double twinning. For each slip or twin system four Voce hardening parameters ($\tau_o$, $\tau_1$, $\theta_o$, and $\theta_1$) are related to the threshold stress ($\tau_s$) for plastic flow and accumulated shear strain ($\Gamma$) within each grain. $\tau_o$ is the Critical Resolved Shear Stress (CRSS) of the respective slip or twinning system, $\tau_1$ is the latent critical resolved shear stress, $\theta_o$ is the initial hardening rate and $\theta_1$ is the latent hardening rate of the slip or twinning system.

$$\tau_s = \tau_o + (\tau_1 + \theta_1\Gamma)\left(1 - \exp\left(-\Gamma\left|\frac{\theta_o}{\tau_1}\right|\right)\right) \qquad (1.1)$$

The VPSC model uses a phenomenological approach for calibrating the Voce hardening parameters, through curve fitting of experimental stress-strain responses. However, since Mg alloys feature multiple potential slip and twinning systems that can be activated upon deformation, depending on crystallographic texture, and loading direction, in order to calibrate the Voce hardening parameters for all possible deformation systems, many experimental results are needed. This complicates the calibration process through trial-and-error curve fitting procedures. A forward sequential quadratic optimization method has been used in our prior work to calibrate 20 hardening parameters for basal slip, prismatic slip, pyramidal slip, extension and contraction twinning systems for a rolled Mg AZ31 alloy [28]. Constraints on the CRSS values were put in place to ensure the Voce hardening conditions reflected experimental deformation modes at their

respective temperatures from 25$^{o}$C to 200$^{o}$C. Texture evolution of the rolled Mg AZ31 alloy during a single pass and multi pass ECAP deformation using simple routes such as Route A (no rotation between passes) and C (180$^{o}$ rotation between passes) has been accurately predicted at elevated temperatures [76]. Therefore, in the present work, VPSC crystal plasticity modeling is utilized to predict crystallographic texture evolution during ECAP, tensile mechanical responses along different loading directions after ECAP, and the formability parameter.

### 1.3.3 Grain Fragmentation in Visco-Plastic Self Consistent (VPSC) Crystal Plasticity Model

Visco-Plastic Self-Consistent (VPSC) crystal plasticity model has been extensively used to study and predict the behavior of magnesium alloys under both simple deformation conditions, such as tension and compression, and more complex deformation processes such as equal channel angular pressing (ECAP) and rolling [16, 28, 67, 70-75]. VPSC crystal plasticity code has been extended over the years with additional features that improved its mechanical and microstructural prediction capabilities [67, 77-83]. Some of these include: Predominant Twinning Reorientation (PTR) scheme for simulating twinning [67], modelling high strain and more complex velocity gradients to simulate severe plastic deformation processes [78, 79], dislocation density hardening accounting for temperature and strain rate effects on plasticity [80], phenomenological implementation of slip-twin interactions improving predictions for anisotropic materials [81], etc.

As more advanced severe plastic deformation processing methods are explored with the VPSC model, new additions to the model need to be made for proper prediction of texture and mechanical property evolution. Recently, the VPSC model with the prior mentioned features was used to predict texture and mechanical properties of Mg AZ31 alloys after Equal Channel Angular Pressing (ECAP). The complex velocity gradients applied to the simulated volume element, due

to complex processing routes, and high strain conditions resulted in inaccurate texture predictions compared to the experimental results. Most of the predicted textures displayed very sharp components with high intensities compared to the gradual intensity variation observed in the experimental pole figures. This further led to poor mechanical property predictions after ECAP.

This lack of accuracy in the predicted texture evolution originates from the approximations introduced in the self-consistent (SC) approach, which was originally developed for predicting effective behavior of linear elastic materials and not for predicting the microstructure evolution [84]. In the VPSC model, crystallographic rotation responsible for texture evolution is calculated based on the average value of stress within the grain and is thus assumed constant within each grain. Therefore, each grain is described by a single crystallographic orientation even at higher strain. EBSD scans of deformed polycrystals clearly indicated that this assumption is not justified, and is the main cause for poor texture predictions [82]. Furthermore, since this approach does not allow variation of misorientation within grains, grain refinement during high strain processing cannot be simulated. Grain refinement phenomena have been extensively observed in experimental microstructures of f.c.c. aluminum after ECAP; high dislocation densities caused by severe plastic deformation create sub-grain boundaries, which eventually develop into high angle grain boundaries [85]. In Mg alloys the grain refinement differs during severe plastic deformation at elevated temperatures, where grains nucleate along the original grain boundaries through dynamic recrystallization forming a necklace grain structure which then populates and consumes the rest of the original grain until a refined microstructure is achieved [28, 66].

In order to predict texture evolution of Mg alloys, recent VPSC additions accounting for the intragranular misorientation evolution were used in this study. Average fluctuation of stress within each grain, described by second moment, is calculated by extending the method developed for

linear elastic behavior [86] to the linearized visco-plastic regime [87, 88]. Average fluctuations of crystallographic orientation within each grain, also described by second moments, are then calculated using the second moments of intragranular stress [15]. The intragranular misorientation distributions are further used to fragment the grains once a user inputted critical intragranular misorientation is reached. Therefore, each grain in the simulations is represented by a statistical distribution of crystallographic orientations, resulting in smoother textures in comparison to the previous VPSC predictions. The extended VPSC model accounting for intragranular misorientation evolution and Grain Fragmentation (GF) is denoted by VPSC-GF.

### 1.3.4 Hall Petch effect in Visco-Plastic Self Consistent (VPSC) Crystal Plasticity Model

Hall Petch effect is the increase of yield strength, ultimate tensile strength of the alloy due to grain refinement processes such as ECAP, rolling, extrusion etc. Smaller grain sizes in Mg alloys are achieved through a combination of temperature step down processes. For example, using rolled Mg AZ31 and using ECAP at 200$^{o}$C for the initial passes then using a temperature step down approach as low as 115$^{o}$C has shown to refine grain size to 1-2 um in size [58, 63-65].

Grain size dependance in Mg alloys have shown a large dependance on the Critical Resolved Shear Stresses (CRSS) of the certain deformation systems. Basal slip has been observed to show very little change in CRSS as a function of grain size where non-basal slip systems, like prismatic slip have shown to activate more after grain refinement which could resulting in better formability at room temperature due to the decrease in CRSS difference [22, 65]. Twinning has also been observed to reduce considerably with grain size [89]. This increased CRSS values for extension and contraction twinning resulting in reduced tension-compression symmetry due to higher non-basal slip deformation modes. This could be the solution to find better formability in Mg alloys.

This dependance on grain size should be able to be recreated in simulation with equivalent CRSS trends in VPSC.

VPSC has been used to portray grain refinement and recrystallization in face centered cubic materials however the increase in CRSS with grain refinement has not been implemented in VPSC very accurately [82, 90]. The only hardening effect is the slip-slip and slip-twin interaction commonly known as self or latent hardening effects in VPSC [91]. However, the slip-grain interaction (with dislocation hardening) in VPSC is not currently modelled and requires secondary calibrations of the voce hardening parameters against experimental ECAP results to accurately portray the CRSS increases for each slip and twin system. This process becomes too cumbersome to repeat after every ECAP process and thus a better Hall-Petch VPSC relationship would be convenient and necessary for each slip and twin system. Experimental tensile and compression tests under various orientation on textured Mg AZ31 has been conducted in prior works to isolate activations of slip and twin systems in Mg alloys to find CRSS values [65] [58]. However, these same trends in Hall Petch relationship have not been shown yet in VPSC.

### 1.3.5 Quantifying Formability using the Anisotropy Effect on Ductility (AED) Parameter

Before an inverse optimization framework could be utilized together with the calibrated VPSC model, a way of quantifying formability needs to be determined. One method of quantifying formability would be through tensile ductility measurements along multiple orientations of a textured material to represent the overall formability. However, due to the anisotropy of Mg alloys the elongation at fracture can vary considerably with orientation, hence multiple experiments need to be conducted for an overall definition of formability. Similarly, R-values can be another source of formability measure, commonly used for rolled FCC materials. Measuring R-values again

would require multiple tests along various orientations and can change greatly with orientation for highly textured materials.

During extended plastic deformation, anisotropy of the material is known to dynamically alter the microstructure of the material either through texture evolution, grain elongation, or void growth and coalescence [92, 93]. Various models have been developed to relate these microstructural evolution processes to the anisotropic effects on plasticity. In previous works, the void growth model showed a good theoretical correlation with the anisotropy of ECAP processed Mg alloys to its plasticity or formability [44]. Assuming a material has a structure with inherent ellipsoidal voids, a model was developed to show how controlling void growth and coalescence could result in enhanced ductility. The major contribution to controlling void growth was controlling the plastic anisotropy around these voids [92]. This plastic anisotropy relationship on void growth was utilized in this study to improve the formability of Mg alloys through ECAP processing. In what follows, it will be summarized how microstructural void growth in materials can lead to a connection between plastic anisotropy and formability.

Here, in order to quantify formability with a single parameter, an invariant of the fourth order anisotropy tensor was considered. The anisotropy tensor is associated with Hill's simple criterion for yielding and plastic flow in anisotropic materials [94]. The invariant of the anisotropy tensor is labeled here as *H* and is presented in Eq. 1.2 which has been derived to describe void growth in a material obeying Hill's criterion. The void growth rate ($\dot{f}$) is then found to be inversely proportional to this scalar anisotropy invariant *H*. Here *T* is the stress triaxiality ratio. Simplifying the equation to power form reveals [44, 95]:

$$\frac{\dot{f}}{\dot{\varepsilon} f} \approx \frac{3}{H} \sinh\left(\frac{3}{H} T\right) \approx \frac{3}{2H} \left(e^{\frac{3T}{H}} - e^{-\frac{3T}{H}}\right) \qquad (1.2)$$

In order to reduce the void growth rate and enhance formability solely based on the void growth model in Eq. 1.2, the anisotropy invariant term needs to be maximized to enhance formability due to the inverse power relationship between $\dot{f}$ and *H*. By increasing *H*, voids tend to grow and coalesce at a slower rate allowing an overall improvement in formability for anisotropic materials.

*H* can be derived from the components of the fourth order anisotropy tensor as shown in Eq. 1.3 where $h_1$, $h_2$ and $h_3$ are associated with tensile principal states while $h_4$, $h_5$ and $h_6$ are the off-axis terms.

$$H = 2\left[\frac{2}{5}\ \frac{h_1+h_2+h_3}{h_1h_2+h_2h_3+h_3h_1} + \frac{1}{5}\left(\frac{1}{h_4}+\frac{1}{h_5}+\frac{1}{h_6}\right)\right]^{1/2} \quad (1.3)$$

The next step requires some form of physical experimental measurements that can be used to determine *H*. Previous studies have reported a relationship between *H* and specifically oriented R-value measurements of a single material [23, 44, 95]. From this section onwards the *H* invariant parameter will be referred to as the Anisotropy effect on Ductility (AED) parameter.

The R-value relationships for each $h_i$ can be substituted into Eq. 1.3 to yield Eq. 1.4. The R-value orientations were named according to a standard ECAP orientation system as displayed in Fig. 1, Extrusion (E), Flow (F) and Longitudinal (L) directions. Furthermore, off axis directions are defined as follows: 45° orientation between Extrusion and Flow directions as (EF), 45° between Extrusion and Longitudinal directions as (EL) and 45° between Flow and Longitudinal directions as (FL). It must be noted that Eq. 4 has been normalized with respect to $R_L$ hence only five R-value parameters are required to calculate the AED parameter.

$$AED = 2\left[\frac{3}{10R_{FL}+5} + \frac{3(R_E+1)}{5\,(2R_{EF}+1)(R_ER_F+1)} + \frac{3(R_E+1)}{5R_E(2R_{EL}+1)(R_F+1)} + \frac{(R_E+1)(R_E+R_ER_F+1)}{5R_E(R_F+R_ER_F+1)}\right]^{1/2} \quad (1.4)$$

In Eq. 1.4, it can be observed that the AED index is defined by a complex combination of lateral strain measurements or R-values along various orientations of the sample. The AED index

contains all lateral ductility measurements, which are in accordance with the changes in texture that might affect slip and twinning deformation modes for the hcp material in the present study.

In order to better understand the physical meaning of the increasing or decreasing trends in the AED index, a simple example is considered here. If an isotropic material is considered, $h_i = 1$ in Eq. 1.3. This would make the AED parameter in Eq. 1.4 equal to 2.0. This is important since, according to the model, any value above 2.0 reduces void growth rate and enhances formability. Vice versa any AED value lower than 2.0 is detrimental to formability. Hence, it is required to maximize the AED parameter above 2.0 for good formability. Furthermore, upon closer inspection of Eq. 1.4, it is observed that mostly an inverse relationship is observed between AED and R-values in all orientations. This is in accordance with the experimental studies that reported R-values lower than 1.0 displaying better formability for Mg alloys [3, 10, 26].

In summary, the AED parameter, calculated using R-values, provides a simple representation of the complex mechanical ductility properties of an hcp alloy with a single formability measure. This parameter will be utilized in the present inverse optimization framework to demonstrate how thermomechanical processing routes can be designed to enhance the formability of a Mg alloy.

### 1.3.6 Inverse Optimization

In order to achieve highly formable Mg alloys, many experimental and simulation methods have been used to find optimum processing paths [3, 6, 9, 10, 14, 27, 44, 54, 55, 72, 73, 96-98]. However, it is still unclear what complete formability ranges are achievable in commercial Mg alloys using the accessible processing techniques, i.e., rolling, conventional extrusion, ECAP or combinations thereof. Trial and error approaches to determining processing routes leading to a target formability level are time consuming and expensive. Optimization tools, on the other hand, can be used to find such formability boundaries if the modeling tools used as part of the

optimization framework can predict correct trends in formability when a selected material is subjected to given thermomechanical processing paths. This can be achieved by coupling modeling and simulation techniques for thermomechanical processing and resulting formability, with an inverse optimization methodology to predict possible thermomechanical processing routes to achieve the target formability.

The present study introduces a complete inverse optimization framework, utilizing the VPSC crystal plasticity modeling, covering entire space of all possible ECAP routes to reach the best one for achieving maximum formability in a specific Mg alloy. The designed new ECAP routes are experimentally implemented and the formability measure for these new routes are experimentally determined to validate the predictions. ECAP is just one possible thermomechanical processing method to present the implementation of the inverse optimization framework introduced in this work. However, many other processing techniques such as dynamic rolling and conventional extrusion, or their combination, can be similarly modeled using VPSC or other crystal plasticity models with the inverse optimization framework to design specific processing routes to achieve a desired formability.

For any inverse optimization framework to predict or design thermomechanical processing routes, a few subcomponents are needed: a calibrated crystal plasticity (or phenomenological) model that takes into account crystallographic texture and microstructure evolution during processing simulations, a way of quantifying formability, that also needs to be predicted by the selected plasticity model, and experimental implementation of the designed routes, and experimental measurements of the formability to confirm the predicted results.

# CHAPTER II

# EXPERIMENTAL AND MODELLING PROCEDURES

## 2.1 Modelling Procedures

### 2.1.1 Calibration of Mechanical Properties from 25ºC to 200ºC

All simulations consist of material point calculations following a prescribed path of macroscopically homogeneous straining. Although individual grains are not explicitly modeled, grains sharing the same orientation are represented by their volume fraction in the aggregate, given by their relative weight in the discretized initial texture. Three slip systems (basal, prismatic, and pyramidal) and two twinning systems (extension and contraction) were considered. For each deformation system, a Voce hardening law was employed from Eq. 5 such that the flow (or threshold) stress, $\tau_s^{\alpha}$, is given in terms of accumulated shear strain, $\Gamma$.

To account for twinning-induced lattice reorientation and subsequent texture evolution, the so-called predominant twin reorientation (PTR) scheme was implemented in the VPSC model. In this scheme, the actual twin volume fraction in the polycrystal aggregate ($V_{act}$) is calculated based on the accumulated twinning shear associated with each twin system. Whenever a whole grain (or more precisely, a group of grains of common orientation) is reoriented by twinning, the effective twin volume fraction ($V_{eff}$) is updated based on the volume fraction of that particular grain in the aggregate. At every deformation step, the fraction accumulated in the individual twinning systems of each grain is compared with a threshold value ($V_{Th}$) that follows the empirical relation,

$$V_{Th} = \mathrm{A}_1 + \mathrm{A}_2 \left(\frac{V_{eff}}{V_{act}}\right) \qquad \text{Equation (2.1)}$$

where $\mathrm{A}_1$ and $\mathrm{A}_2$ are constants [68] [99]. This scheme thereby favors the reorientation of grains using the most active twinning systems. In addition, the self-adjusting nature of the scheme guarantees the reoriented volume fraction, $V_{eff}$, to coincide with the actual volume fraction, $V_{act}$. Whenever $V_{eff}$ is larger than $V_{act}$, the threshold $V_{Th}$ increases and inhibits further reorientation by twinning until the actual volume fraction catches up with the effective one. For all temperatures for both extension and contraction twinning, the values of $A_1$ and $A_2$ were set to 0.1 and 0.4, respectively. Here, the $A_1$ term delays reorientation by twinning until at least 10% of the grain has twinned, while $A_2$ allows $V_{Th}$ to increase quickly at the onset of twinning, while simultaneously preventing excessive twinning effects from being simulated. For later work on ECAP Mg alloys the $A_1$ and $A_2$ parameters were optimized to ensure correct twinning properties were portrayed in the mechanical behavior since there is a significant decrease in twinning for finer grain materials. The VPSC model was modified in this study to allow extension twinning to occur within contraction twins (double twinning). For further details on VPSC crystal plasticity modeling, refer to [16] [75] [67].

In principle, temperature dependence of Voce hardening parameters can be represented in some functional form. This was not attempted here, however, since isothermal conditions were assumed at the relatively slow loading rates (quasi-static tests). Thus, a different set of hardening parameters is considered for each test temperature. By way of consequence, the full model involves many parameters: four Voce hardening parameters ($\tau_o$, $\tau_1$, $\theta_o$, and $\theta_1$) per deformation system (out of 5) and temperature (out of 4 considered in the experiments), leading to a total of 80 material

parameters. What renders model identification even more arduous is the fact that all parameters are subject to some constraints. For instance, one must satisfy:

$$\tau_0 \geq 0;\ \tau_1 \geq 0;\ \theta_0 \geq 0; \theta_1 \geq 0; \theta_0 \geq \theta_1, \qquad \text{(Constraint 2.1)}$$

which is the main constraint. In addition, following constraints were found to lead to faster and improved calibration:

$$20.0 \leq Basal\ \tau_o \leq 35.0\ MPa\ ;\quad 20.0 \leq Extension\ Twin\ \tau_o \leq 60.0\ MPa, \text{ (Constraint 2.2)}$$

$$10.0 \leq Basal\ \tau_o \leq 35.0\ MPa\ ;\ \ 80.0 \leq Extension\ Twin\ \tau_o \leq 150.0\ \ MPa, \text{(Constraint 2.3)}$$

where Constraint (2.2) is for $T$ = 25°C, 100°C, and 150°C whereas Constraint (2.3) is for $T$ = 200°C only.

Model parameter identification was carried out using the optimization component of the Z-Set software suite . The VPSC code and the Z-Set optimizer have been coupled using a code embedding capability within Z-Set [100]. In addition, a python script was used to automate input/output operations. As in Eq 2.2, a least-square cost function is based on the error:

$$E^{\mathrm{X}} = \frac{1}{\varepsilon^{\mathrm{X}}_{\max}} \int_0^{\varepsilon^{\mathrm{X}}_{\max}} \left(\sigma^{\mathrm{X}}_{\exp} - \sigma^{\mathrm{X}}_{\mathrm{sim}}\right)^2 d\varepsilon \qquad \text{Equation (2.2)}$$

where X stands for the loading orientation (TD, ND, or 45toND), $\varepsilon^{\mathrm{X}}_{\max}$ is the maximum uniform strain reached in the experiments, and $\sigma^{\mathrm{X}}_{\exp}$ and $\sigma^{\mathrm{X}}_{\mathrm{sim}}$ are, respectively, the measured and simulated flow stresses at a given strain. The cost function is obtained by summing the errors over all three loading orientations. Sequential Quadratic Programming (SQP) method was utilized enabling optimization under multiple constraints. The solution is obtained by solving a sequence of quadratic subproblems that converge to the best fit (see [101] for more details on the SQP method). Model calibration was carried out separately for each test temperature so that each optimization is

over 20 parameters. In a first step, only constraint (2.1) was considered to allow optimization over a wide parameter space. In a second step of iterations, constraints (2.2) and (2.3) were implemented for basal slip and extension twinning parameters.

### 2.1.2 Using Visco-Plastic Self Consistent Model to simulate Equal Channel Angular Pressing

ECAP simulations at 200°C were conducted using VPSC to verify simulated texture with known experimental results. Route 4A, four passes with no rotation along the extrusion axis, and 4C, four passes with 180° rotations along the extrusion axis after each pass, was simulated matching experimental work conducted on the same rolled Mg AZ31 material texture to ensure proper texture prediction [23].

Experimentally measured texture of rolled Mg AZ31 texture files was discretized into weighted Euler angle orientations of 1000 grains. The starting rolled texture is shown in Figure 2.4. ECAP was simulated under a velocity gradient tensor given by Equation 2.3 where $\dot{v}$ is the velocity gradient and $\dot{\varepsilon}$ is the applied strain rate [58]. The $\dot{\varepsilon}$ was fixed at $10^{-2}$ $s^{-1}$ for all simulated ECAP deformations. The total plastic strain of 0.954 was applied for every pass to match the effective strain of the 90° tool dies used in experimental work. This was derived under the assumption of finite element analysis methods conducted by H.S. Kim et al. [102] where the effect of dead zones at the intersection of the ECAP die determined the total effective strain per pass for high strain hardening materials. Since texture predictions for 4A and 4C routes at 200$^{o}$C did not match experimental texture, the voce hardening parameters were altered accordingly for more accurate texture predictions.

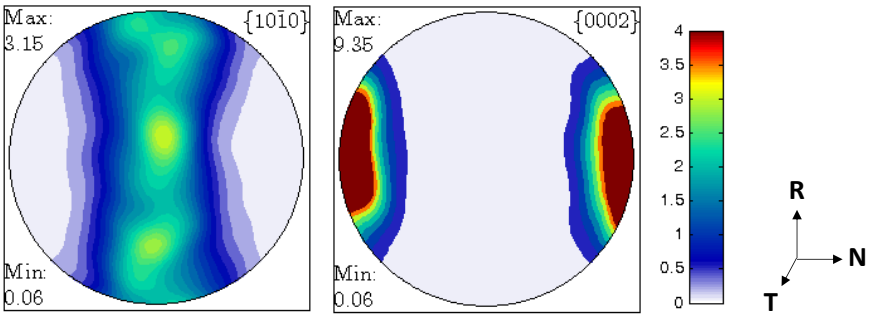


**Figure 2.4: Texture for rolled Mg AZ31 used for simulated ECAP deformation. This was rotated to get either basal Extrusion or basal Flow directions.**

$$\dot{v} = \frac{\dot{\varepsilon}}{2}\begin{Bmatrix} 1 & -1 & 0 \\ 1 & -1 & 0 \\ 0 & 0 & 0 \end{Bmatrix} \qquad \text{(Eq. 2.3)}$$

### 2.1.3 Implementation of the Inverse Optimization Framework

The VPSC crystal plasticity model has been utilized in conjunction with an optimization approach to develop an automated inverse optimization methodology that can predict new and unique ECAP routes that would result in superior formability of Mg alloys. This methodology is expected to yield unconventional ECAP routes that have not been experimentally attempted before. In order to perform VPSC model simulations in an automated fashion and design new ECAP routes, three major steps should be performed. Fig. 2 displays the simple breakdown of these steps and the following sections describe the steps in detail. Step 1 requires the calibration of the VPSC model parameters by fitting simulated results to available mechanical test data and textures from known ECAP routes. The calibrated VPSC model should then be able to predict the R-values and thus, the AED parameter, for any arbitrary ECAP route. The number of ECAP passes in this study is limited to four passes. Moving on to step 2, an optimization algorithm is used to

find newly designed ECAP routes (i.e., combinations of the rotation angles between passes) that would result in the maximum AED parameter (as a formability index) by performing VPSC runs in an automated fashion. The final step is to experimentally validate the new designed ECAP routes by performing ECAP following the designed routes on Mg alloy billets. Tensile tests, R-value measurements, and calculation of the AED parameters are performed on each new ECAP route to ensure that the experimental results match well with the predicted VPSC results.

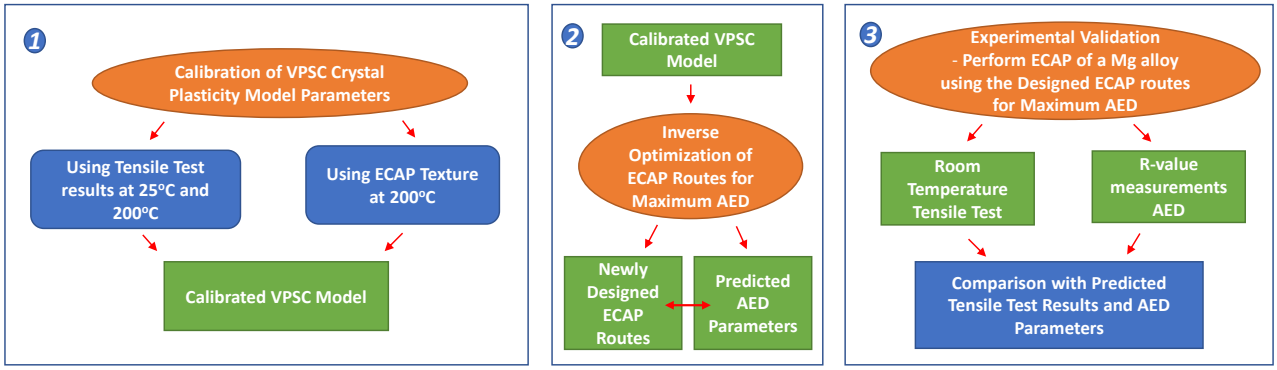


**Figure 2.5. Flowchart of the inverse optimization framework introduced in this study in order to design new ECAP routes that would result in superior formability in Mg alloys, demonstrating the three steps: 1) the calibration of VPSC crystal plasticity model, 2) inverse optimization of the ECAP routes to maximize the AED parameter, and 3) experimental validation.**

### 2.1.4 Calibration of Crystal Plasticity Model Parameters using Monotonic Tension Experiments

Following Step 1 in Fig. 2.5, tensile experiments were conducted on commercially rolled Mg AZ31 alloy with a strong basal texture, shown in Fig. 2.4, along three orthogonal directions [28]. The Normal Direction (N), Transverse direction (T) and the diagonal direction between the Normal

and Rolling directions (NR) were tested at a constant strain rate of $5x10^{-4}$ $s^{-1}$ at two different temperatures, 25ºC and 200ºC. Only the uniform deformation region of the tensile tests was considered for the calibration since VPSC does not consider strain localization effects.

Due to a strong basal texture, particular slip or twinning systems could be activated at a controlled manner by choosing the orientation for tensile testing. At room temperature, tensile loading along the N direction would mainly activate extension twinning, T direction would activate mostly prismatic slip while NR direction would mostly activate basal slip [28]. At higher temperatures of 200ºC pyramidal slip activity is known to drastically increase for all orientations [16, 58]. This becomes very important in VPSC calibration since the set of hardening parameters ($\tau_o$, $\tau_1$, $\theta_o$, $\theta_1$) for each deformation system could drastically change as a function of temperature. To ensure proper calibration of the hardening parameters of each slip and twinning system, an optimization method, the Sequential Quadratic Programming (SQP), was used for fitting the simulated VPSC tensile test results with their respective experimental results [28]. VPSC was coupled to the optimization software Z-set [100] via a python code during the optimization iterations in order to alter and update VPSC files such as the hardening parameters, virtual tensile test orientation (N, T, or NR), and predicted stress-strain response in the output files. The output files are used to calculate the optimization error of the iteration. The optimization code then utilizes the error to choose a new set of hardening parameters for the next iteration.

Eq. 2.4 was the objective function used for minimizing the difference between the experimental and simulated tensile curves for each direction.

$$Minimize \quad E^{X} = \frac{1}{\varepsilon^{X}_{max}} \int_0^{\varepsilon^{X}_{max}} \left(\sigma^{X}_{exp} - \sigma^{X}_{sim}\right)^2 d\varepsilon \qquad (2.4)$$

where X represents the directions (N, T, or NR), $\varepsilon^{X}_{max}$ is the maximum uniform strain reached in the experiments within the uniformly deformed region (this region included the yield point to just

before necking of the sample), and $\sigma_{\text{exp}}^{\text{X}}$ and $\sigma_{\text{sim}}^{\text{X}}$ are the stresses for the experiments and simulations at the given strain.

Using the SQP method, the hardening parameters ($\tau_o$, $\tau_1$, $\theta_o$, $\theta_1$) for each deformation system are optimized in order to minimize $E^{\text{X}}$ for all X directions. However, due to the lack of compression test data along the N direction, there is no sufficient contraction twinning activity in any of the directions tested. This could yield low fidelity hardening parameters for contraction twinning in the VPSC model and lead to somewhat inaccurate predictions during step 2 in Fig. 2.5. The contraction twinning system was still considered during the VPSC calibration process since minor contraction twins were still observed in experiments at room temperature along the T direction.

### 2.1.5 Calibration of Crystal Plasticity Model Parameters using Texture Measurements after ECAP

After the calibration using the tensile responses at two temperatures, we have further calibrated the hardening parameters using ECAP textures of the Mg AZ31 alloy, experimentally performed and measured only at 200$^o$C (since ECAP is not possible at room temperature), as shown in Fig. 2.5, step 1. This was needed because after calibrating the hardening parameters only with the tensile responses, the texture predictions for ECAP routes 4A (no rotation between passes) and 4C (180$^o$ rotation along extrusion direction between each pass) at 200$^o$C did not sufficiently match the experiments. Hence, the Voce hardening parameter $\tau_o$ at 200$^o$C was recalibrated to better match the experimental textures of ECAP 4A and 4C cases. All ECAP passes were simulated assuming simple shear deformation along the 45$^o$ angle at the intersection of the two ECAP channels, with a total accumulated strain of 0.954 per pass at $10^{-2}$ $s^{-1}$ strain rate to mimic the ECAP experiments.

The total accumulated strain was calculated assuming a medium strain hardening rate for Mg alloys following the work by Kim *et al.* [103].

In summary, the Voce hardening parameters at 25$^{o}$C were calibrated using tensile test results along three directions of the rolled Mg AZ31 alloy while the hardening parameters at 200$^{o}$C were calibrated using both tensile test results and texture measurements from two ECAP routes after four passes. Since the inverse optimization methodology will be utilized to design new ECAP routes for processing at 200$^{o}$C, the texture evolution at 25$^{o}$C was not needed in the calibration process.

### 2.1.6 Inverse Optimization to derive highly formable ECAP Routes using VPSC (No Grain Fragmentation)

This section introduces the details of step 2 in the flowchart of Fig 2.5. The Z-set optimization software suite [100] was coupled with the VPSC model to design ECAP routes tailored to maximize the AED index. The problem was constrained to ECAP rotations between passes from 0° to 360°, counterclockwise along the extrusion direction as written in Eq. 2.5 (i.e., all integer values between 0$^{o}$ to 360$^{o}$ are viable selections for the optimization, not just 90° rotations). Here $Rot_n$ is the rotation of the billet along the extrusion direction before the $n^{th}$ ECAP pass. Only sets of 4-pass ECAP routes were optimized hence $n$ was constrained to a maximum of 4. All ECAP routes were simulated using the Voce hardening parameters calibrated for the 200$^{o}$C experiments. The objective error function to be minimized is defined by Eq. 2.6 where $AED_{Target}$ was defined by the user and $AED_{Predict}$ was predicted using VPSC for the simulated ECAP route at a given optimization iteration. Due to the non-linear AED objective function with rotation constraints needed for this problem the SQP optimization method was utilized. The VPSC model was coupled to the Z-set software via a python code in order to alter or update the VPSC files such as input

textures, ECAP deformation paths, hardening parameters and output files, during the optimization iterations.

$$0.0 \leq Rot_n \leq 360.0\,;\ \ n = 1, 2, 3, 4 \qquad (2.5)$$

$$Error = \left(AED_{Target} - AED_{Predict}\right)^2 \qquad (2.6)$$

Four initial rotations along the extrusion direction were pre-defined as initial conditions before each optimization process, as shown in Table 2.1. The initial rotations were selected based on the three main ECAP routes commonly used in the past: Route A, Route C, and Route $B_c$ (+90° rotation between ECAP passes). Table 2.1 lists several combinations of 0°, 90° and 180° rotations along the extrusion direction as initial conditions in order to find a globally optimized ECAP route solution.

**Table 2.1: Initial conditions for the ECAP rotations between the passes to initialize the optimization iterations for the inverse optimization of ECAP routes to achieve maximum formability [76].**

| Route Name | Rotation* 1 (°) | Rotation* 2 (°) | Rotation *3 (°) | Rotation* 4 (°) |
|---|---|---|---|---|
| 4J | 0 | 0 | 0 | 0 |
| 4K | 180 | 0 | 0 | 0 |
| 4L | 180 | 180 | 0 | 0 |
| 4M[76] | 180 | 180 | 180 | 0 |
| 4N | 180 | 180 | 180 | 180 |
| 4O | 90 | 0 | 0 | 0 |
| 4P | 90 | 90 | 0 | 0 |
| 4Q | 90 | 90 | 90 | 0 |
| 4R | 90 | 90 | 90 | 90 |

*All rotations are counterclockwise along the extrusion axis.

At each optimization iteration, the simulated ECAP texture of the attempted route was used to simulate the tensile tests using the Voce hardening parameters, calibrated for 25°C experiments above, to a strain level of 0.1 along the five respective orientations (E, F, EF, EL and FL). The $AED_{Predict}$ values were then calculated using Eq. 1.3 with the simulated R-values from each simulated tensile test and then compared with the $AED_{Target}$.

The $AED_{Target}$ was set to 5.0, which was hypothesized to be not attainable by the ECAP process so this would drive the optimization to choose ECAP routes with the highest possible AED. At each iteration, a collection of four rotations would be selected by the optimization tool with slight perturbations to alter the value of the objective function. Then the optimization tool delivers the four-rotation sequence (i.e., the route) that would minimize the error of the objective function. The iterations continue until no further minimization of the objective function is possible.

### 2.1.5 Texture and Mechanical Optimization of Visco Plastic Self Consistent Model with Grain Fragmentation

In this study, both the original VPSC model, denoted simply by VPSC [67], and the VPSC-GF [83] model are used to simulate tension and ECAP of Mg AZ31 alloy at 200$^{o}$C, in order to test the difference in the simulated texture evolution between the two models. Mg alloys deform by activation of 3 main slip modes: basal <a>, prismatic <c>, and pyramidal <c+a>; and activation of two twinning modes: extension and contraction. Double twinning was also considered by allowing the nucleation of extension twins within a contraction twinned region. The Voce hardening parameters for each slip and twin mode need to be calibrated simultaneously, resulting in a total of 20 calibration parameters, to simulate tensile mechanical behavior and texture after ECAP. Considering the large number of parameters, and complexity of applied loading, manual

calibration is difficult. This study provides a novel optimization strategy that considers mechanical and texture experimental data in order to calibrate the VPSC and VPSC-GF models. It is noted that the dynamic recrystallization is not simulated in our model. It is assumed that the dynamic recrystallization, as described above, does not appreciably affect the texture evolution for magnesium alloys due to randomness of the process and limited grain growth. Effect of dynamic recrystallization on the mechanical behavior is taken into account through the hardening parameters. VPSC simulations will be calibrated on, and/or compared to two experimental data sets. First experimental data set includes measured tensile mechanical stress-strain curves of commercially rolled Mg AZ31 at 200$^{o}$C along three different directions, Normal (N), Transverse (T) and 45$^{o}$ between Normal and Rolling (NR). Second experimental data set includes measured textures after four different ECAP routes: 4K, 4P, 4C, and 4A, where the rotations along the extrusion direction between each pass are shown in Table 2.2. For all these routes strain rate, $\dot{\varepsilon}$, was $10^{-2}$ $s^{-1}$ and 90$^{o}$ angle ECAP die was used. The textures were measured using a 2D Vantec Bruker detector with a Cu Kα source. In VPSC, velocity gradient, $\partial \dot{v}/\partial x$, given, by Eq 2.3, was used to simulate a 90$^{o}$ angle ECAP die by using a 45$^{o}$ shearing angle. ECAP has also been shown to have a tensile strain along the extrusion axis and compression strain along the longitudinal axis of the billet [16].

**Table 2.2: Experimental ECAP routes showing rotation along the extrusion direction between each pass. All Rotations are counterclockwise along the extrusion direction.**

| ECAP Route | Rotation 1 | Rotation 2 | Rotation 3 | Rotation 4 |
|---|---|---|---|---|
| **4K** | 0 | 0 | 90 | 0 |
| **4P** | 0 | 180 | 90 | 90 |
| **4C** | 0 | 180 | 180 | 180 |
| **4A** | 0 | 0 | 0 | 0 |

Due to the complexities of having 20 Voce hardening parameters that affect simulated mechanical properties and texture evolution, it becomes very difficult and time consuming to calibrate all these parameters manually to an optimal set of values. To address this issue, optimization methods were used to calibrate all 20 Voce hardening parameters in VPSC and VPSC-GF using the experimental mechanical tensile stress-strain curves and experimental ECAP textures as the reference. Optimization requires reducing the error of an objective function that compares a quantifiable difference between experimental and simulation data. Due to a constrained problem with boundary conditions and a non-linear objective function the Sequential Quadratic Programming (SQP) optimization model was used in this study. Fig. 1 shows three different optimization strategies adopted in this study, which are next described in detail.

Fig. 2.6 (a) shows an optimization path utilizing only the mechanical testing data for commercially rolled Mg AZ31 and for three different loading directions (N, T, NR) to calibrate the Voce hardening parameters in the VPSC model, termed VPSC mechanical optimization. The objective error function for optimization of tensile stress-strain curves is shown in Eq 2.4 where X represents the tensile direction (N, T, or NR). $\varepsilon_{\max}^{X}$ is the maximum uniform strain reached in the experiment within the uniformly deformed region of the stress-strain curve (this region included an interval between the yield point to just before necking of the sample), and $\sigma_{\exp}^{X}$ and $\sigma_{\mathrm{sim}}^{X}$ are the stress for the experiment and simulation at the given strain. Reducing this tensile error will cause the simulated tensile plots to eventually overlap with experimental results. Calibrated Voce hardening parameters are then used to simulate the ECAP routes from Table 1 and predict the final deformed textures. This was done to provide a control simulation data set for the study, and this is also the most common method of calibrating Voce hardening parameters using VPSC.

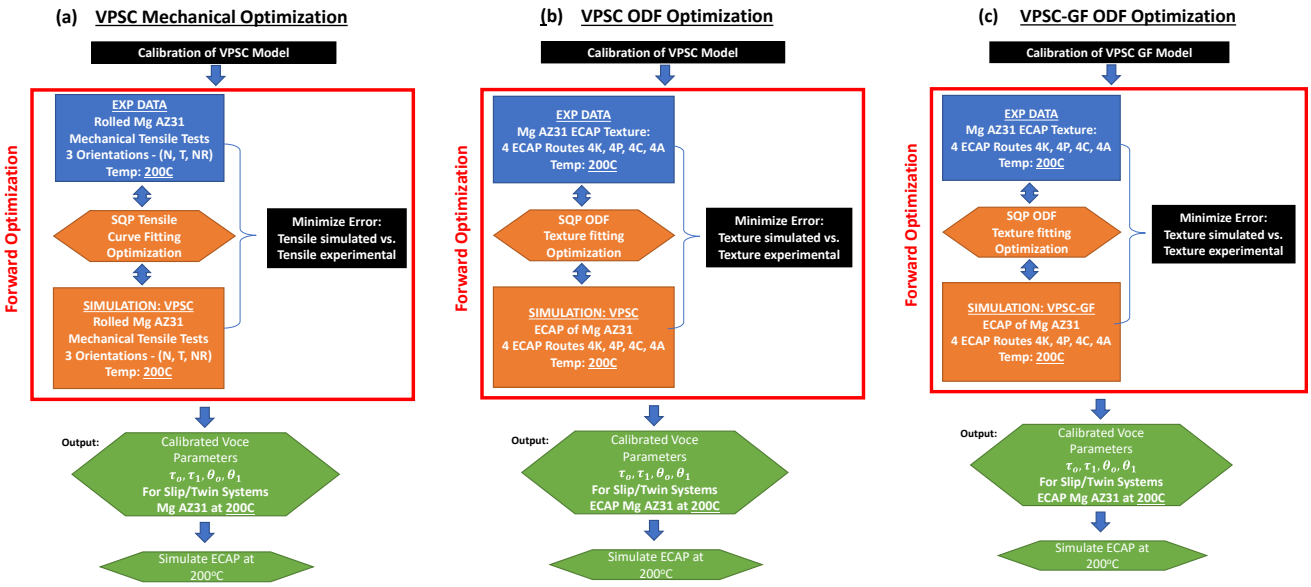


**Figure 2.6: Describes the optimization paths used to calibrate voce hardening parameters: (a) VPSC optimization strategy using experimental mechanical tensile tests (b) VPSC optimization strategy using experimental ECAP route textures and Orientation distribution function (ODF) and (c) VPSC Grain Fragmentation (GF) optimization strategy using experimental ECAP route textures and ODF optimization.**

The second optimization strategy (Fig. 2.6 (b, c)) was a novel idea of incorporating experimental ECAP texture data during calibration of the Voce hardening parameters in VPSC and VPSC-GF. The initial guess for the optimization procedure is the Voce parameters calibrated on the tensile stress-strain curves only. Texture is equally important as mechanical data and needs to be considered for more robust VPSC and VPSC-GF calibration. Fig 2.6 (b) shows optimization strategy of Voce hardening parameters for the VPSC model based on experimental ECAP textures from Table 1, termed VPSC ODF optimization. Defining the objective error function directly based on the discrete orientations creates a problem in the optimization procedure since the number of discrete orientations can be over 10,000, thus making the minimization problem very difficult to converge. In order to simplify the objective error function, textures are represented by

Orientation Distribution Functions (ODFs), which replace thousands of discrete orientations by a functional form. Next, objective error function for the texture of a selected route Y is given by

$$Minimize(\ ODF^{Y}_{Error}\ ) = \left|\int ODF^{Y}_{Exp}\ (g)\ dg - \int ODF^{Y}_{Sim}\ (g)\ dg\right| \qquad (2.7)$$

where $g$ is crystal orientation. The results from texture optimization will show if texture from severe plastic deformation processing is needed to calibrate voce hardening parameters more accurately. Fig 2.6 (c) shows a same optimization path as Fig 2.6 (b), but this time the VPSC-GF model was used in the optimization process to calibrate the Voce hardening parameters, termed VPSC-GF ODF optimization. The same objective function as in Eq. 2.7 was used for this optimization path. This approach should provide the most accurate texture results to date with the novel texture optimization working in conjunction with the VPSC-GF model.

### 2.1.6 Addition of Hall Petch Hardening Effect into Visco-Plastic Self Consistent Grain Fragmentation Model

VPSC voce hardening model uses self and latent hardening between slip-slip and slip-twin interactions to determine the change in CRSS ($\tau_o$) under an applied strain rate [91]. The voce parameters ($\tau_1$, $\theta_o$, and $\theta_1$) do not change during the simulated deformation process such as ECAP. Instead, the voce hardening parameters are used to update the CRSS of each slip and twinning system of each grain which are then averaged to find the final CRSS value. This means, $\tau_o$ is the only voce hardening parameter that evolves during deformation. In VPSC-GF, second order misorientation calculations are used to calculate stress, misorientation and lattice rotation distributions to calculate grain fragmentation and misorientation distributions [90]. However, for both cases, the interaction of dislocation to grain boundary interaction is not considered as a hardening factor. These issues result in a lack of critical resolved shear stress evolution for slip and twinning systems after ECAP. It is known CRSS of extension and contraction twinning

increases with decreasing grain size which allows non-basal slip systems such as prismatic slip to be more prevalent during deformation which could result in more formable Mg alloys [22, 65, 89].

In order to properly reflect the grain refinement hardening and dislocation hardening after ECAP, the same mechanical optimization method from section 2.1.4 was used to reduce the error between simulated VPSC tensile tests and experimental ECAP tensile tests to calibrate the ($\tau_o$, $\tau_1$, $\theta_o$, and $\theta_1$) voce hardening parameters and PTR Twinning scheme variables (A1, A2) using 5 ECAP orientations (E, F, EF, FL, EL).

In order to find the Hall Petch relationship in VPSC the grain size of the ECAP material is also required in simulation but VPSC GF is not able to portray a grain size. An experimental relationship was used to relate grain fragments in VPSC to grain size in experiments. Three different Mg AZ31 processed materials were chosen as an experimental measurement for grain size, Mg AZ31 Rolled, ECAP 4K and ECAP 4P. The grain size for each of these materials were measured and plotted again the VPSC grain fragments to derive a power law relationship. This creates a grain fragment to grain size relationship that can be used for the Hall-Petch properties in the VPSC model.

### 2.1.7 Inverse Optimization Methodology with Visco-Plastic Self Consistent Grain Fragmentation

With the updated and improved VPSC Grain fragmentation and Hall Petch model the inverse optimization could now be repeated to derive better AED results. The objective error function for AED was kept the same as before, as defined by Eq. 2.5 where $AED_{Target}$ was defined by the user at 10.0 and $AED_{Predict}$ was predicted using VPSC for the simulated ECAP route at a given optimization iteration. Due to the non-linear AED objective function with rotation constraints needed for this problem the SQP optimization method was utilized. The VPSC model was coupled

to the Z-set software via a python code in order to alter or update the VPSC files such as input textures, ECAP deformation paths, hardening parameters and output files, during the optimization iterations.

$$0.0 \leq Rot_n \leq 360.0\,;\ \ n = 1, 2, 3, 4 \qquad (2.5)$$

$$Error = \left(AED_{Target} - AED_{Predict}\right)^2 \qquad (2.6)$$

Four initial rotations along the extrusion direction were pre-defined as initial conditions before each optimization process, as shown in Table 2.3. The initial rotations were selected based on the three main ECAP routes commonly used in the past: Route A, Route C, and Route $B_C$ (+90$^o$ rotation between ECAP passes). Table 2.3 lists several combinations of 0$^o$, 90$^o$ and 180$^o$ rotations along the extrusion direction as initial conditions in order to find a globally optimized ECAP route solution. 90$^o$ fixed orientation was used for rotation 1 where the normal direction of the billet was along the extrusion direction. This was done to show how initial orientation has a large effect on the final optimized AED parameter.

**Table 2.3: Initial conditions for the ECAP rotations between the passes to initialize the optimization iterations for the inverse optimization of ECAP routes to achieve maximum formability.**

| Route Name | Rotation* 1 (°) | Rotation* 2 (°) | Rotation *3 (°) | Rotation* 4 (°) |
|---|---|---|---|---|
| 4G | 0 | 0 | 0 | 0 |
| 4H | 0 | 90 | 90 | 90 |
| 4I | 0 | 180 | 180 | 180 |
| 4J | 0 | 270 | 270 | 270 |
| 4K | 90 fixed | 0 | 0 | 0 |
| 4L | 90 fixed | 180 | 180 | 180 |
| 4M | 90 fixed | 270 | 270 | 270 |
| 4N | 90 fixed | 180 | 90 | 180 |
| 4O | 90 fixed | 90 | 180 | 90 |

*All rotations are counterclockwise along the extrusion axis.

## 2.2 Experimental Procedures

### 2.2.1 Experimental Validation of the Designed ECAP Routes and Mechanical Testing

In order to confirm the success of the designed ECAP routes and $AED_{Predict}$ parameters for these routes, the Mg alloy billets should be processed using the designed ECAP routes and the AED parameters of the billets should be experimentally measured as shown in step 3 of the flowchart in Fig. 2.5. The continuous rotations derived from the model were discretized to $90^o$ increments and the $AED_{Predict}$ parameters was recalculated in VPSC. Two discretized routes, the highest $AED_{Predict}$ parameter route and a lowest $AED_{Predict}$ parameter route, were then selected for the experiments.

Two 1"x1"x7" Mg AZ31 billets were annealed at $350^oC$ for 12 hours inside an Argon gas furnace before ECAP. The billets were water quenched right after the heat treatment. Prior to ECAP, the billets were placed in a preheated ECAP die at $200^oC$ for 30 mins. Extrusion was conducted at an effective strain rate of $10^{-2}$ $s^{-1}$. A back pressure of 30 MPa was applied during the first two ECAP passes and then was lowered to 20 MPa for the $3^{rd}$ and $4^{th}$ ECAP passes.

Tensile and texture samples were cut from the ECAP billets using wire Electro-Discharge Machining. Texture samples were cut from the flow plane surface of each billet. A Bruker-AXS D8 XRD device with a Cu K-alpha source was used to attain experimental texture measurements [44]. All five tensile directions (E, F, EF, EL and FL) were cut according to the five R-value orientations required for the AED calculations in Eq. 4. Tensile specimens had a nominal gauge length of 8 mm with a 3 mm x 1.5 mm cross section. The EDM layer from the tensile samples were removed using 400 grit SiC paper and edges were cleaned using the Dremel tool. The samples were tested at room temperature using an MTS tensile frame at the strain rate of $5 \times 10^{-4}$ $s^{-1}$ and strained to a ~0.10 plastic strain and then unloaded to measure the lateral (width and thickness)

dimension changes. The same samples were then reloaded to failure. The axial strain was measured using an extensometer directly attached to the gauge section of the tensile samples. The sample width and thicknesses were measured before and after straining to calculate the R values for each direction using Eq. 4.

R-values were calculated using the ratios of the lateral strains measured after the tensile tests to ~0.10 plastic strain. For the flat dog-bone specimens, the true lateral strains were calculated from the ratio of the natural log of the either the width or thickness of the specimen as in Eq. 2.8 where $d_l$ is final width or thickness and $d_o$ is the respective initial width or thickness of the sample. The R-value expressions were derived in Eq. 2.9 with respect to the ECAP orientation convention system of Extrusion (E), Flow (F) and Longitudinal (L) directions as shown in Fig. 1.3. Similarly, the R value equations for the 45$^o$ off-axes orientations are comprised of taking the strain of the perpendicular plane of the tensile direction being tested as in Eq. 2.10 [44].

$$\varepsilon_x = \frac{\ln(d_l)}{\ln(d_o)} \qquad (2.8)$$

$$R_E = \frac{\varepsilon_F}{\varepsilon_L}\ ; \qquad R_F = \frac{\varepsilon_L}{\varepsilon_E}; \qquad R_L = \frac{\varepsilon_E}{\varepsilon_F} \qquad (2.9)$$

$$R_{EF} = \frac{\varepsilon_{EF}}{\varepsilon_L}\ ; \qquad R_{EL} = \frac{\varepsilon_{EL}}{\varepsilon_F}; \qquad R_{FL} = \frac{\varepsilon_{FL}}{\varepsilon_E} \qquad (2.10)$$

Within the VPSC model, R-values are determined by applying tension along a given direction while keeping a zero stress along the in-plane and through thickness directions. The strain rates are calculated at each time increment before updating the hardening parameters or texture, which allows R-value calculation at any stage of deformation [78].

CHAPTER III

# MECHANICAL AND TEXTURE CALIBRATION OF VPSC CRYSTAL PLASTICITY MODEL (NO GRAIN FRAGMENTATION)

## 3.1 Simulated Results of Optimized VPSC Model

Fig. 3 shows the experimental (solid lines) tensile curves with the fitted VPSC curves (dotted lines) up to the uniform deformation region. The simulated fits for all four temperatures and three directions show very good agreement with experimental tensile tests after fitting VPSC simulated curves with optimization fitting. The voce hardening parameters after optimization are shown in Table 3.4. The constraints imposed for each temperature range allowed a better representation of the experimental slip and twinning mechanisms for their respective temperatures.

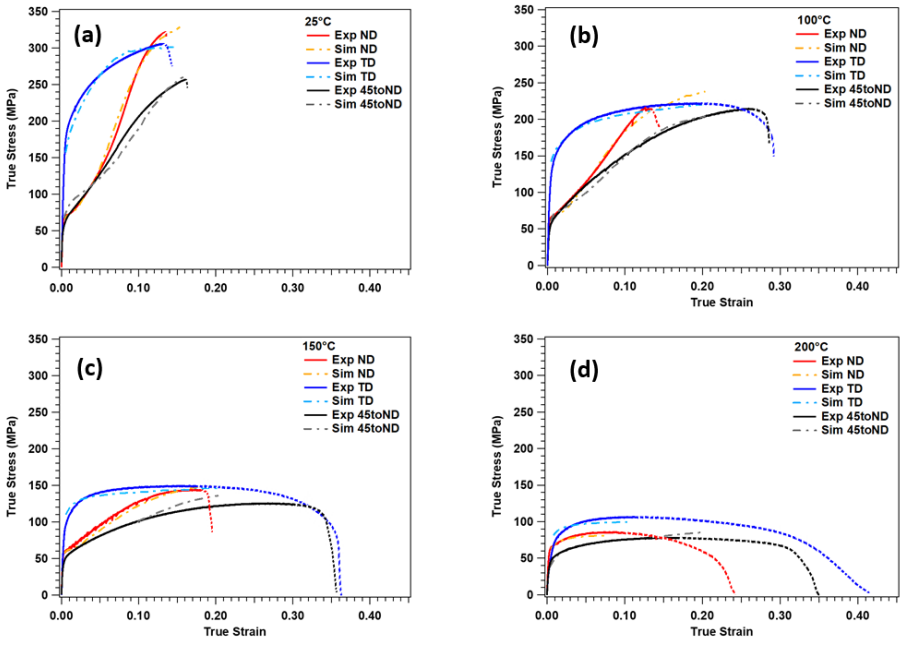


**Figure 3.6: True stress vs. true strain responses of Mg-AZ31 alloy tested in tension along three different ND TD and 45toND (RN direction). The results at (a) 25°C, (b) 100°C, (c) 150°C, and (d) 200°C. Simulated, optimized fits from VPSC model for each respective direction and temperature are also included up to a maximum of 0.2 true strain. Exp: Experiments; Sim: Simulations [28]**

**Table 3.4. Voce hardening parameters for the simulated, optimized fits from the VPSC model of the true stress – true strain curves in Figure 3.7 at each of the four test temperatures [28].**

| | $\tau_o$ (MPa) | | | | $\tau_1$ (MPa) | | | |
|---|---|---|---|---|---|---|---|---|
| | ***25°C*** | ***100°C*** | ***150°C*** | ***200°C*** | ***25°C*** | ***100°C*** | ***150°C*** | ***200°C*** |
| **Basal** | 28.1 | 24.6 | 21.0 | 14.0 | 13.0 | 4.84 | 6.53 | 14.5 |
| **Prismatic** | 135.9 | 120.4 | 95.5 | 82.4 | 114.1 | 29.7 | 8.64 | 40.0 |
| **Pyramidal <c+a>** | *<255.0* | <223.5 | 91.1 | 62.5 | <294.0 | <48.9 | 161.3 | 9.4 |
| **Extension Twinning** | 53.47 | 55.1 | <49.4 | <99.3 | ~0 | ~0 | <~0 | <~0 |
| **Contraction Twinning** | 130.5 | 200.4 | <150.4 | <112.0 | 107.4 | 74.0 | <45.1 | <83.2 |

| | $\theta_o$ (MPa) | | | | $\theta_1$ (MPa) | | | |
|---|---|---|---|---|---|---|---|---|
| | ***25°C*** | ***100°C*** | ***150°C*** | ***200°C*** | ***25°C*** | ***100°C*** | ***150°C*** | ***200°C*** |
| **Basal** | 927.7 | 5555.2 | 962.3 | 348.6 | 28.02 | 54.0 | 3.3 | ~0 |
| **Prismatic** | 1017.3 | 653.2 | 351.0 | ~0 | ~0 | ~0 | ~0 | ~0 |
| **Pyramidal <c+a>** | <9659.0 | <963.1 | 828.5 | 121.9 | <~0 | <~0 | ~0 | ~0 |
| **Extension Twinning** | ~0 | ~0 | <~0 | <~0 | ~0 | ~0 | <~0 | <~0 |
| **Contraction Twinning** | 18042.3 | 4319.8 | <1382.0 | <1261.0 | ~0 | ~0 | <~0 | <~0 |

In order to show this mechanical dependence on temperature more clearly the slip and twinning activities from VPSC simulations are shown in Fig. 3.8. Fig. 3.8 (a-c) represents the VPSC slip and twinning activities for 25$^o$C. The TD case presents significant prismatic slip activity, accounting for around 20% to 50% of the deformation, basal slip activity ranging from 40% to 70%, and extension twinning activity generally below 10%. In contrast to the TD sample, the activities for the ND and 45toND samples show extensive basal slip and extension twinning, respectively (Figs. 3.8 b, c). Overall, these results are consistent with expectations based on

Schmid's Law. The initial stage of the strain hardening in the ND case can be attributed to extension twinning which reorients the c-axes 86° away from the tensile axis. After reorientation, strain hardening occurs, as twins become favorably oriented for prismatic slip systems where we see a transition from extension twinning to prismatic slip in Fig. 3.8 b. Comparatively minimal contraction twinning activity was predicted for the 45toND and ND samples and no pyramidal $< c + a >$ slip was evident in the predictions for any loading condition as is expected for room temperature. VPSC results support double twinning activity in the TD sample. Using the PTR scheme, double twinning was implemented into the model by allowing extension twins to form within contraction twins, and Fig. 3.8 (a) shows a rapid increase in extension twinning activity after contraction twinning activity at 0.08 strain indicative of double twinning.

Fig. 3.8 (d-f) shows slip and twinning activities for the 100°C case. Slip system activities were similar to room temperature activities however the extension and contraction twinning was predicted to have decreased considerably along TD. The temperature increases from 25°C to 100°C may allow pyramidal $< c + a >$ slip to compete more easily with contraction twinning for c-axis compression along TD but VPSC predictions did not predict any form of pyramidal slip but rather just higher amounts of prismatic slip activity. In experimental tests, along ND it was found contraction and double twinning had occurred near the fracture surface but VPSC is unable to predict this behavior due to the lack of strain localization effects in the VPSC model.

Fig. 3.8 (g-i) shows the activities for 150°C case. In experimental results there is a transition from basal slip dominated deformation to non-basal slip with high amount of dynamic recrystallization. This transition at 150°C is only observed in VPSC predictions for the TD direction with the initial spike in pyramidal slip and the slight increase in prismatic slip. Due to the lack of recrystallization model in VPSC the recrystallized grains that tended to favor pyramidal

slip are not modelled in VPSC, so the initial grain structure does not promote any pyramidal slip for the ND and 45toND orientations.

Fig 3.8 (j-l) shows the VPSC activities for 200C case. There is a complete transition from twinning-based deformation activity to mainly a pyramidal slip dominant deformation even surpassing prismatic activity in all orientations. This promotes the presence of continuous dynamic recrystallization which requires the pyramidal slip to occur. This SQP optimization tool shows a good calibration method and its versatility in dealing with non-linear functional fitting and dealing with large number of fitting parameters. With the correct constraints the mechanical properties in VPSC could be predicted with just fitting the mechanical stress-strain properties of the material.

| Temp (°C) | TD | ND | 45toND (RN) |
|---|---|---|---|
| 25 | 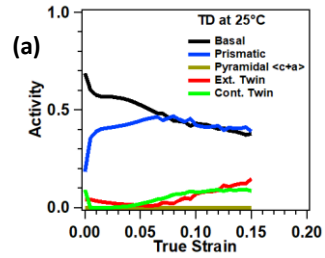 | 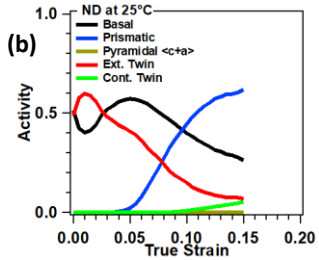 | 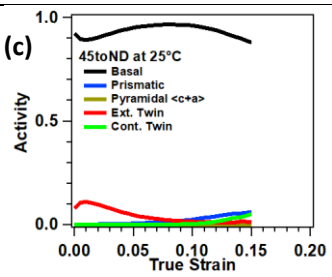 |
| 100 | 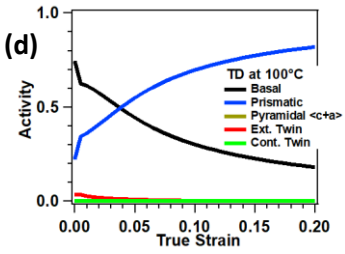 | 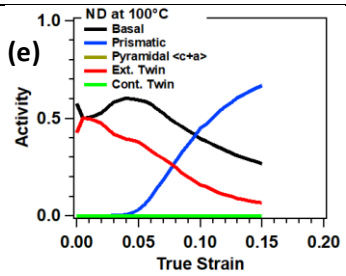 | 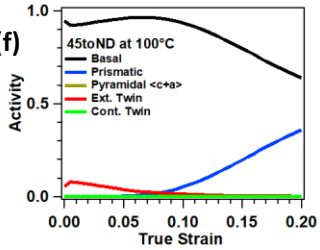 |
| 150 | 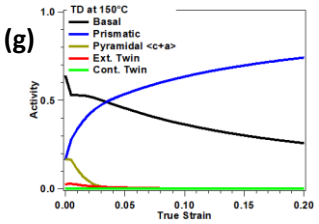 | 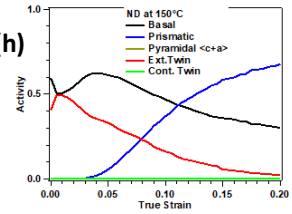 | 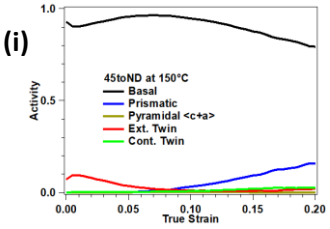 |
| 200 | 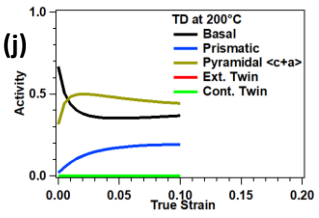 | 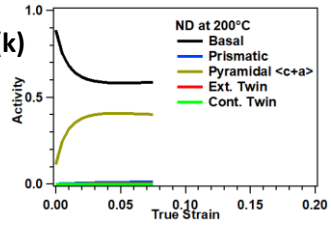 | 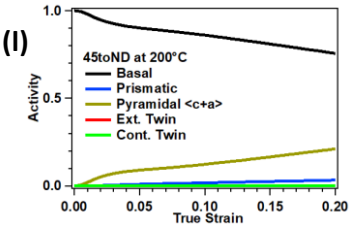 |

**Figure 3.7: Slip and twinning activity for TD, ND and 45toND directions at temperatures of (a-c) 25C, (d-f) 100C, (g-i) 150C and (j-l) 200C [28].**

### 3.2 ECAP Texture correction using VPSC

Experimental texture measurements of Mg AZ31 alloys after ECAP routes of 4A and 4C at 200°C conducted by Basu et al. [23] shows a 4A texture similar to the rolled condition with a strong basal texture while the 4C texture shows basal pole splitting at an approximately 45° interval as shown in Figure 3.9. These textures were taken as a template for calibration of the VPSC Texture calibration process.

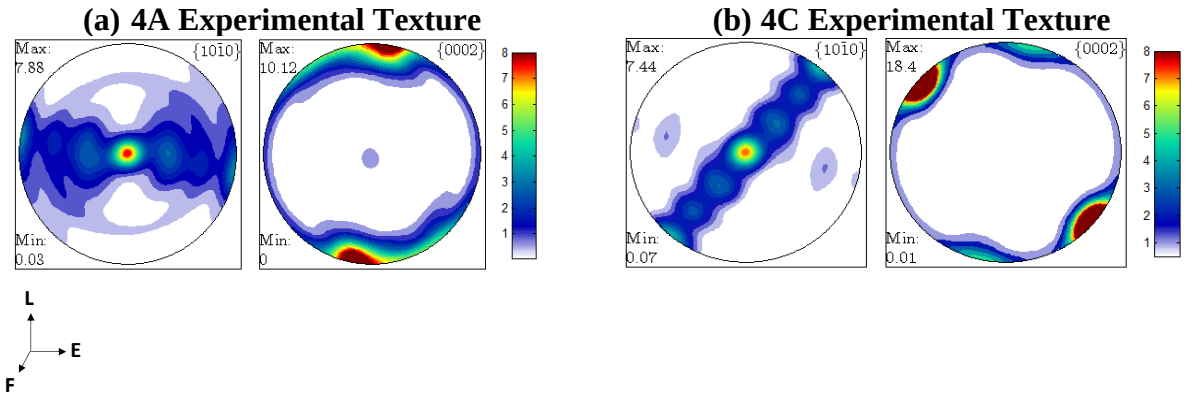


**Figure 3.8: Experimental ECAP (a) 4A and (b) 4C Texture for Mg AZ31 processed at a temperature of 200ºC [23]**

The same ECAP deformation process was simulated under VPSC using the voce hardening parameters at 200°C from Table 3.4 and the velocity gradient matrix shown in Eq. 2.3. Figure 3.10 shows the simulated (0002) plane ECAP 4A texture. Here the pole figure shows an unusual basal pole splitting for the 4A route and new density peaks, circled with a red dashed line, also form at 90° to the basal pole orientation which were not observed in experimental texture results of ECAP 4A. Deformation activities showed a high propensity of the pyramidal and basal slip with minimal extension twinning. In order to prevent basal pole splitting for route 4A, two approaches were

studied where extension twinning was completely suppressed allowing more pyramidal slip and the next approach was to allow high amounts of extension twinning with less pyramidal slip to fix the texture error. This was done by mainly changing the extension twinning $\tau_o$ CRSS term of the 200ºC case in Table 3.4 from 99.3 MPa to 130 MPa to suppress twinning or decreased 99.3 MPa to 49 MPa to promote twinning as shown in Table 3.5. The other voce hardening terms were kept the same as Table 3.4.

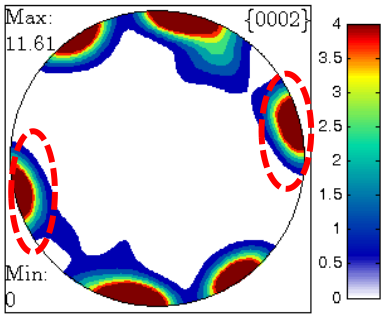


**Figure 3.9: (0002) basal pole figure of ECAP simulated 4A texture at 200°C using Voce hardening parameters from Table 1. Circled locations show unusual development of basal texture density not observed in experimental 4A condition [76].**

**Table 3.5: $\tau_o$ CRSS values used for ECAP at 200°C under twin suppression and twin promotion conditions [76].**

| | $\tau_o$ (MPa) at 200ºC | |
|---|---|---|
| | ***Twin Suppression*** | ***Twin Promotion*** |
| **Basal** | 14.0 | 13.5 |
| **Prismatic** | 82.4 | 97.2 |
| **Pyramidal <c+a>** | 62.5 | 57.4 |
| **Extension Twinning** | **130.0** | **49.1** |
| **Contraction Twinning** | 110.0 | 112.0 |

In the twin suppression case basal poles still showed splitting with extra density peaks at 90° interval from the basal poles with an additional rotation of the overall texture. Extension twin promotion showed a weaker basal pole split as one basal pole was significantly weaker than the other which is much closer to the experimental 4A results. From these observations it was determined extension twinning needs to be promoted for accurate texture prediction in addition to a slight pyramidal slip suppression. Hence Table 3.6 was designed as the final $\tau_o$ parameter for ECAP texture prediction at 200°C with a slight increase in pyramidal slip CRSS and some promotion of extension twinning. Figure 3.11 a shows the ECAP 4A texture with no basal splitting nor any density peak outliers with these new parameters hence matching experimental results quite well. Plotting ECAP 4C texture in Fig. 3.11 b also showed good agreement with experimental results where the basal poles have shown to split after deformation.

**Table 3.6: Final calibrated $\tau_o$ parameters for 200°C ECAP for VPSC (No Grain Fragmentation) [76].**

| | **$T_o$ (MPa) at 200°C** |
|---|---|
| | ***Twin Promotion with Pyramidal Slip Suppression*** |
| **Basal** | 14.0 |
| **Prismatic** | 82.4 |
| **Pyramidal <c+a>** | **72.5** |
| **Extension Twinning** | **99.3** |
| **Contraction Twinning** | 110.0 |

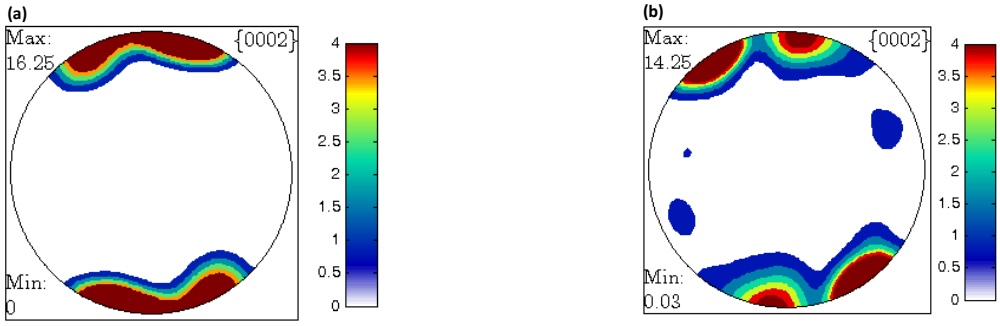


**Figure 3.10: (0002) basal pole figure of simulated ECAP texture at 200°C under route (a) 4A and (b) 4C using $\tau_o$ parameters from Table 3.6. [76]**

## 3.3 Summary and Conclusion

In addition, a Visco-Plastic Self-Consistent crystal plasticity model was employed to simulate the experimental stress-strain responses at various temperatures. Model identification was based on an optimization method of sequential quadratic programming, delivering a simultaneous fit to stress-strain curves from twelve (12) independent data sets (3 orientations at 4 temperatures). The model was also able to predict the activities of deformation mechanisms and resulting textures up to failure initiation over the full range of temperatures, and thus, to provide guidance in interpreting the experimental results. The ECAP simulation in VPSC did not produce accurate results and required an alteration to the optimized voce hardening parameters. This was done by promoting twinning and suppressing pyramidal slip for better accuracy for simulated ECAP texture. This version of the VPSC model does not account for grain fragmentation nor recrystallization at high temperatures.

# CHAPTER IV

# OPTIMIZATION OF PROCESSING PATHS TO TAILOR FORMABILITY OF MG-AL-ZN ALLOYS

## 4.1 Calibration of VPSC Crystal Plasticity Model and Predicted AED Parameters

Please note all the textures and mechanical tests from last chapter was recalibrated and updated for Chapter 4. Fig. 4.12 presents the experimental tensile tests (solid lines) performed along N, T and NR (labelled 45toND in the Chapter 3) directions for the rolled Mg AZ31 alloy at 25$^{o}$C and 200$^{o}$C with their respective VPSC simulated fits (dotted lines) using the optimization method introduced above. The VPSC simulations after the optimization of the hardening parameters exhibit good agreement with the experimental results. Comparing the predicted deformation activities for each orientation at 25$^{o}$C, it was observed that basal slip and prismatic slip were dominant along T direction, only basal activity was dominant along NR direction, while extension twinning, and basal slip was most dominant along N direction. These deformation modes agree well with the microstructural findings reported in [28]. Pyramidal slip activity was found to drastically increase at 200$^{o}$C in all directions while twinning was significantly reduced, as expected. Pyramidal slip activity resulted in a decrease in prismatic slip activity while basal slip activity at 200$^{o}$C remained comparable to room temperature. These results again agree well with experimental microstructural observations [28].

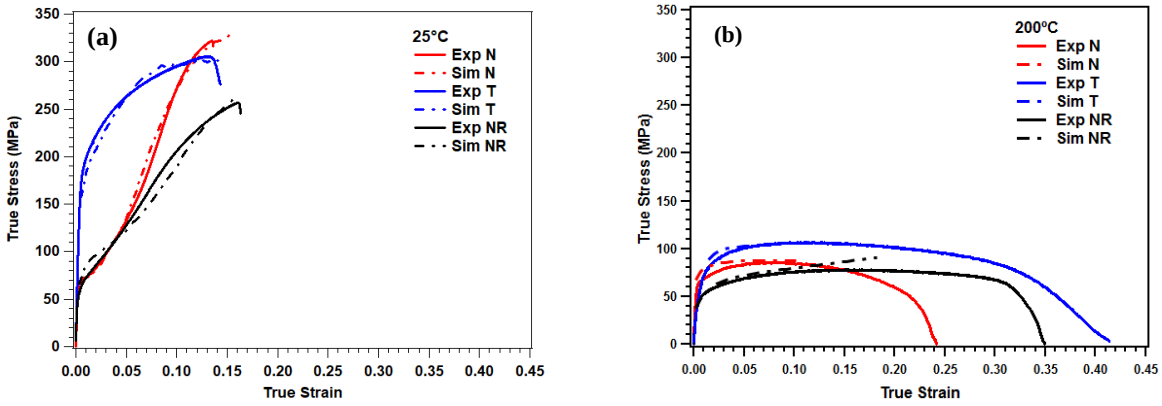


**Figure 4.11: Experimental tensile test results of Mg AZ31 alloy together with the VPSC crystal plasticity model simulation fits for the orientations N, T, NR, conducted at (a) 25oC and (b) 200oC [31]. Simulation fits were achieved by determining the model hardening parameters using the optimization algorithm introduced in the text in order to minimize the error. NR: diagonal direction between the Normal (N) and Rolling (R) directions.**

Fig. 4.13 presents the experimental textures together with the VPSC simulated textures for routes 4A and 4C which are in good agreement. The simulated 4A texture exhibits some splitting in the basal pole figure along the longitudinal direction, but the prismatic pole figures agree well. This difference could be related to the limitation of the current VPSC model which does not consider grain fragmentation or recrystallization effect which is known to occur during high temperature ECAP deformation [16, 58]. Table 4.7 shows the final calibrated VPSC hardening parameters after the optimization using the tensile test results along 3 directions at 25$^{o}$C, and Table 4.8 presents the calibrated hardening parameters after the optimization using both tensile test results along 3 directions and ECAP texture for 2 different routes (4A and 4C) at 200$^{o}$C.

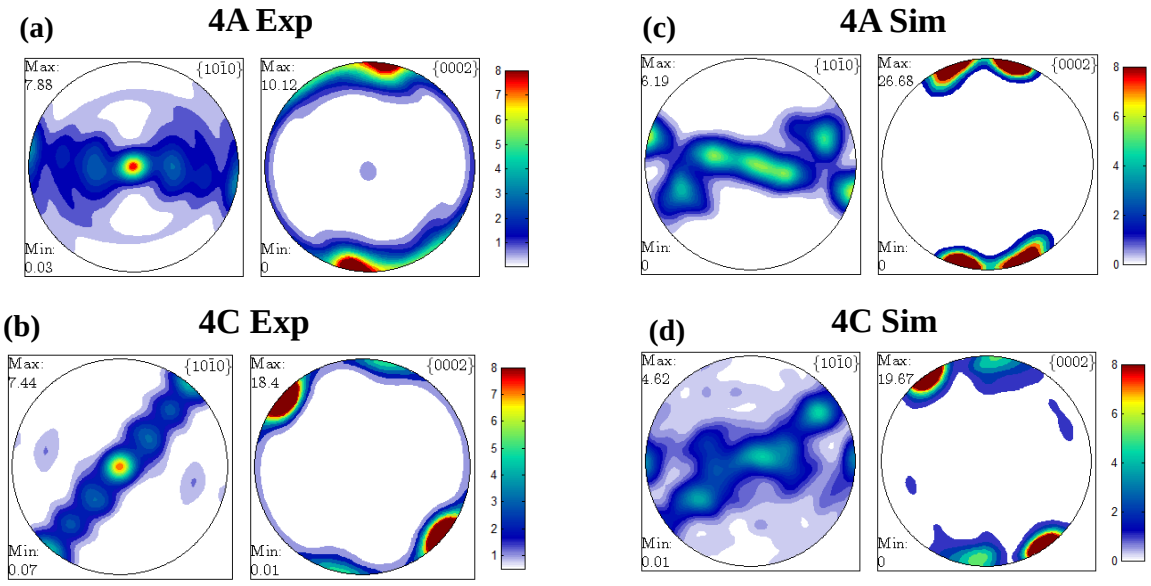


**Figure 4.12: (0002) Basal and (10$\bar{1}$0) Prismatic pole figures of Mg AZ31 alloy after ECAP at 200°C following Routes 4A ((a) and (c)) and 4C ((b) and (d)). Experiments ((a) and (b)) and VPSC simulations ((c) and (d)) [65].**

**Table 4.7. Calibrated Voce hardening parameters for Mg AZ31 alloy slip and twinning systems at 25ºC using experimental tensile tests along Normal (N), Transverse (T) and the diagonal direction (NR) between N and Rolling (R) directions [28].**

| Deformation Systems | $\tau_o$ (MPa) | $\tau_1$ (MPa) | $\theta_o$ (MPa) | $\theta_1$ (MPa) |
|---|---|---|---|---|
| **Basal** | 28.1 | 13.0 | 927.7 | 28.02 |
| **Prismatic** | 135.9 | 114.1 | 1017.3 | ~0 |
| **Pyramidal <c+a>** | 255.0 | 294.0 | 9659.0 | 0 |
| **Extension Twinning** | 53.47 | ~0 | ~0 | ~0 |
| **Contraction Twinning** | 130.5 | 107.4 | 18042.3 | ~0 |

**Table 4.8: Calibrated Voce hardening parameters of Mg AZ31 alloy slip and twinning systems at 200ºC using experimental tensile tests along N, T and NR orientations and experimental ECAP textures for routes 4A and 4C textures.**

| Deformation Systems | $\tau_o$ (MPa) | $\tau_1$ (MPa) | $\theta_o$ (MPa) | $\theta_1$ (MPa) |
|---|---|---|---|---|
| **Basal** | 14.0 | 14.5 | 348.6 | ~0 |
| **Prismatic** | 82.4 | 40.0 | ~0 | ~0 |
| **Pyramidal <c+a>** | 72.5 | 9.4 | 121.9 | ~0 |
| **Extension Twinning** | 99.3 | ~ 0 | ~0 | ~0 |
| **Contraction Twinning** | 112.0 | 83.2 | 1261.0 | ~0 |

Fig. 4.14 (a) shows the experimentally measured AED parameters of Mg AZ31 alloy at room temperature as a function of the compressive plastic strain for the as-received rolled plate and the samples ECAP processed at 200°C following routes 4A and 4C [23]. The ECAP samples were annealed at 350$^{o}$C for 24 hours prior to the AED measurements at room temperature. The VPSC model was used to perform virtual tensile tests and predict the same AED parameters at room temperature as a function of the tensile plastic strain (Fig. 4.14 (b)) using the simulated textures for ECAP 4A and 4C conditions and the experimental texture for the as-received rolled plate, as initial textures, and the calibrated hardening parameters listed in Table 4.7. Even though the experimental AED measurements under compressive plastic strain were compared with the predicted AED under tensile plastic strain, the same trends hold true for the measured AED indices for both tensile and compression as stated by Basu *et al*. [23]. Fig. 4.14 shows a very good agreement between experimental and predicted AED indices as a function of the plastic strain, which confirms that VPSC can predict trends in AED index for ECAP processed materials with acceptable accuracy with the current calibrated parameters, even without recrystallization or grain fragmentation considerations. This calibrated VPSC model can now be used to design new ECAP routes with higher AED values using the inverse optimization method introduced above.

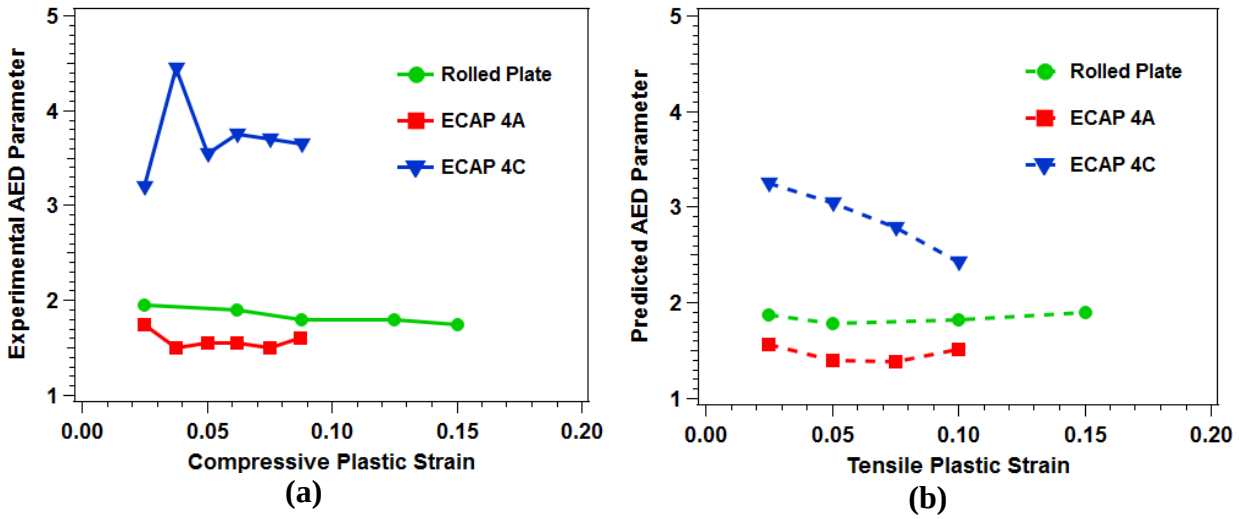


**Figure 4.13: (a) Experimentally measured AED parameters of Mg AZ31 alloy as a function of compressive plastic strain at room temperature for as-received rolled plate and after ECAP processing at 200°C following Routes 4A and 4C [65]. (b) AED parameters predicted using the calibrated VPSC model for the same conditions under tensile plastic strain showing matching trends in AED parameters.**

## 4.2 New ECAP Route Design using the Inverse Optimization Method

Table 4.9 shows the final optimized routes derived by the inverse optimization method for the nine initial conditions shown in Table 2.1. All simulated rotations were counterclockwise along the Extrusion Direction (ED). $AED_{Predict}$ at 0.10 plastic strain and number of iterations has also been provided for each optimized route. It should be noted that the final optimized route was dependent on the initial rotations from Table 2.1. This is due to a common optimization issue with multiple local minima present in the objective function leading to convergence at a singular minimum other than the global objective minimum. To avoid this issue a range of initial guesses had to be considered for a thorough optimization of the objective function. The initial conditions studied here provided several new unexplored routes not considered in the past. The inverse

optimization tool was able to sample over 1089 different 4 pass ECAP routes using just these nine initial rotations in Table 2.1.

**Table 4.9: Final ECAP route solutions for the inverse optimization method using the initial rotations given in Table 2.1 [76].**

| Route Name | Rotation* 1 (°) | Rotation* 2 (°) | Rotation* 3 (°) | Rotation* 4 (°) | $AED_{Predict}$ at 0.1 Plastic Strain | No of Iterations |
|---|---|---|---|---|---|---|
| **4J** | 0 | 246 | 0 | 42 | 2.86 | 83 |
| **4K** | 165 | 25 | 23 | 0 | 2.19 | 130 |
| **4L** | 97 | 0 | 0 | 253 | 2.92 | 102 |
| **4M** | 0 | 151 | 25 | 104 | 2.57 | 94 |
| **4N** | 175 | 236 | 84 | 245 | 3.26 | 143 |
| **4O** | 157 | 40 | 91 | 43 | 2.73 | 234 |
| **4P** | 134 | 125 | 50 | 61 | 2.49 | 63 |
| **4Q** | 138 | 157 | 161 | 72 | 4.09 | 90 |
| **4R** | 141 | 279 | 87 | 251 | 4.06 | 150 |

*All rotations are counterclockwise along the extrusion axis.

Prior experimental work has shown that the highest experimentally measured AED parameter was for route 4C with an AED of 2.69 [44]. The same route 4C was simulated using the calibrated VPSC model and the $AED_{Predict}$ was derived to be a slightly lower value of 2.39. With this consideration, the VPSC inverse optimization predicted 8 out of the 9 routes (underlined) with a higher $AED_{Predict}$ than the $AED_{Predict}$ of route 4C. The highest $AED_{Predict}$ was for route 4Q at 4.09.

Figure 4.15 shows the AED index as a function of plastic tensile strain for the rolled optimized selected routes of Mg AZ31 at room temperature. Since AED parameter or formability changes as function of strain at room temperature this needs to be checked for final route considerations. Route N showed the highest AED of 5.1 at 0.05 strain however the AED decreases rapidly at strains higher than 0.15. All routes except J shows this downward trend in formability to ~2.0 at higher plastic strains of 0.2. Only route J showed an AED index of 2.43 at 0.2 strain

which still shows good formability at higher strains showing promising ductility properties for deep drawing tests where applied strains can be much higher than 0.1.

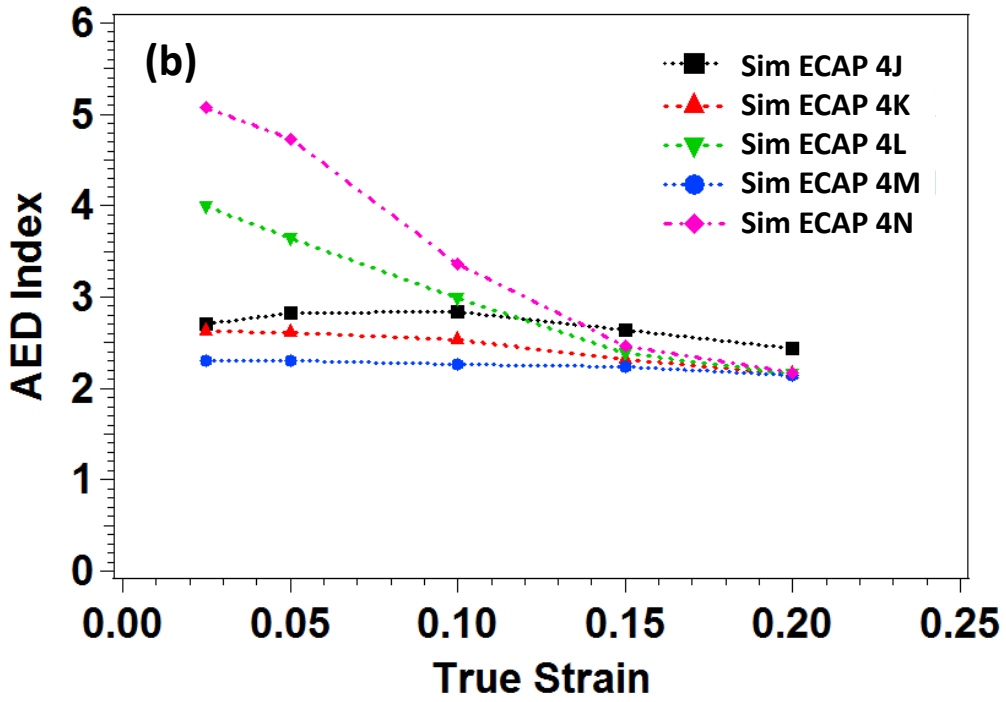


**Figure 4.14: Simulated AED Index as a function of tensile plastic strain for selected optimized routes derived by the inverse method [76].**

In order to confirm the inverse optimization predictions, equivalent experimental ECAP routes need to be tested to validate the $AED_{Predict}$ results. Due to a constrained square cross section of the experimental ECAP setup, the nearest discretized 90° increments were taken for each optimized route from Table 4.9 and the $AED_{Predict}$ parameter was re-calculated using the VPSC model as shown in Table 4.10. For the first rotation in column two, 0°/180° rotations were labeled accordingly due to the two-fold symmetry of the rolled Mg texture along the E direction.

Furthermore, 4N and 4R after discretization resulted in the same route. Route 4K had the lowest $AED_{Predict}$ of 2.16 and 4P had the highest $AED_{Predict}$ of 3.10. Routes 4K and 4P were, thus, selected for experimental validation which would cover two extremes of ECAP formability predicted by the model. These ECAP experiments were subsequently performed at 200°C.

**Table 4.10: Discretized ECAP routes at 90º increments for the optimized rotations in Table 4.9.**

| Route Name | Rotation* 1 (°) | Rotation* 2 (°) | Rotation* 3 (°) | Rotation* 4 (°) | $AED_{Predict}$ at 0.1 Plastic Strain |
|---|---|---|---|---|---|
| **4J** | 0/180 | 270 | 0 | 90 | 2.79 |
| **4K** | 0/180 | 0 | 90 | 0 | **2.16** |
| **4L** | 90 | 0 | 0 | 270 | 2.95 |
| **4M** | 0/180 | 180 | 0 | 90 | 2.18 |
| **4N** | 0/180 | 270 | 90 | 270 | 2.39 |
| **4O** | 0/180 | 90 | 90 | 90 | 2.31 |
| **4P** | 0/180 | 180 | 90 | 90 | **3.10** |
| **4Q** | 0/180 | 180 | 180 | 90 | 2.37 |
| **4R (same as 4N)** | 0/180 | 270 | 90 | 270 | 2.39 |

*All rotations are counterclockwise along the extrusion direction.

## 4.3 Comparison of Experimental and Predicted R-values, AED parameters, and Crystallographic Textures for the Designed ECAP Routes

Tensile tests were conducted along all five orientations (E, F, EF, EL and FL) for the designed routes 4K and 4P where the R-values were measured at ~10-11% plastic strain. The five R-values from each direction were then used to calculate the $AED_{Exp}$ parameters for Routes 4P and 4K using Eq. 1.3. Fig. 4.16 presents the R-values and AED parameters for Routes 4K (Fig. 4.16 (a)) and 4P (Fig. 4.16 (b)).

As it can be seen in the figure, the predicted R-values and AED index values for the optimized ECAP routes exhibit notable discrepancy with the experimental results. Therefore, the experimental textures for these routes were also compared with the VPSC predicted textures as shown in Fig 4.17. Figs. 4.17 (a) and (b) show the VPSC predicted $(10\bar{1}0)$ prismatic and (0002) basal pole figures for the Routes 4K and 4P while Figs. 4.17 (c)-(d) represent their respective experimental ECAP textures. It is clear that VPSC texture predictions (Figs. 4.17 (a)-(b)) show a similar orientation to the experimental textures but the texture densities are more separated or discretized compared to the experimental results.

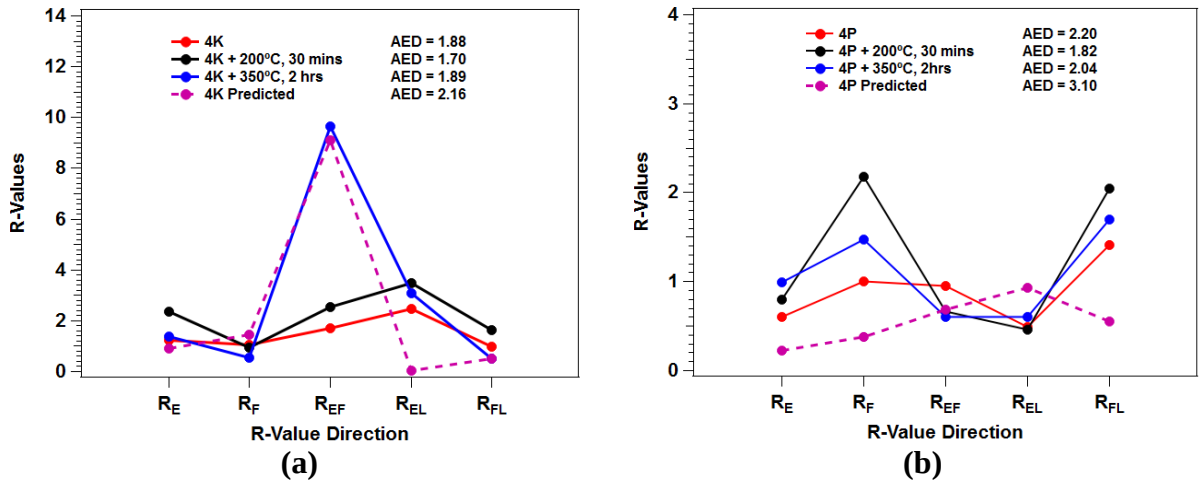


**Figure 4.15: Experimental R values for the tensile directions of E, F, EF, EL and FL at ~10%-11% plastic strain for the designed Routes 4K (a) and 4P (b), in as-processed conditions and after two post-annealing heat treatments (at 200°C for 30 min. and 350°C for 2 hours). The plots also include the predicted R-values for the same routes. Corresponding experimentally determined and predicted AED parameters are also included in the legends.**

This discrepancy between the experiments and predictions is attributed to the limitation of the current VPSC model which does not consider dynamic grain fragmentation or recrystallization

effects known to occur at 200°C during the ECAP deformation [16, 45, 54, 58]. Hence, an annealing step was included here to address the lack of dynamic grain fragmentation and recrystallization in the model.

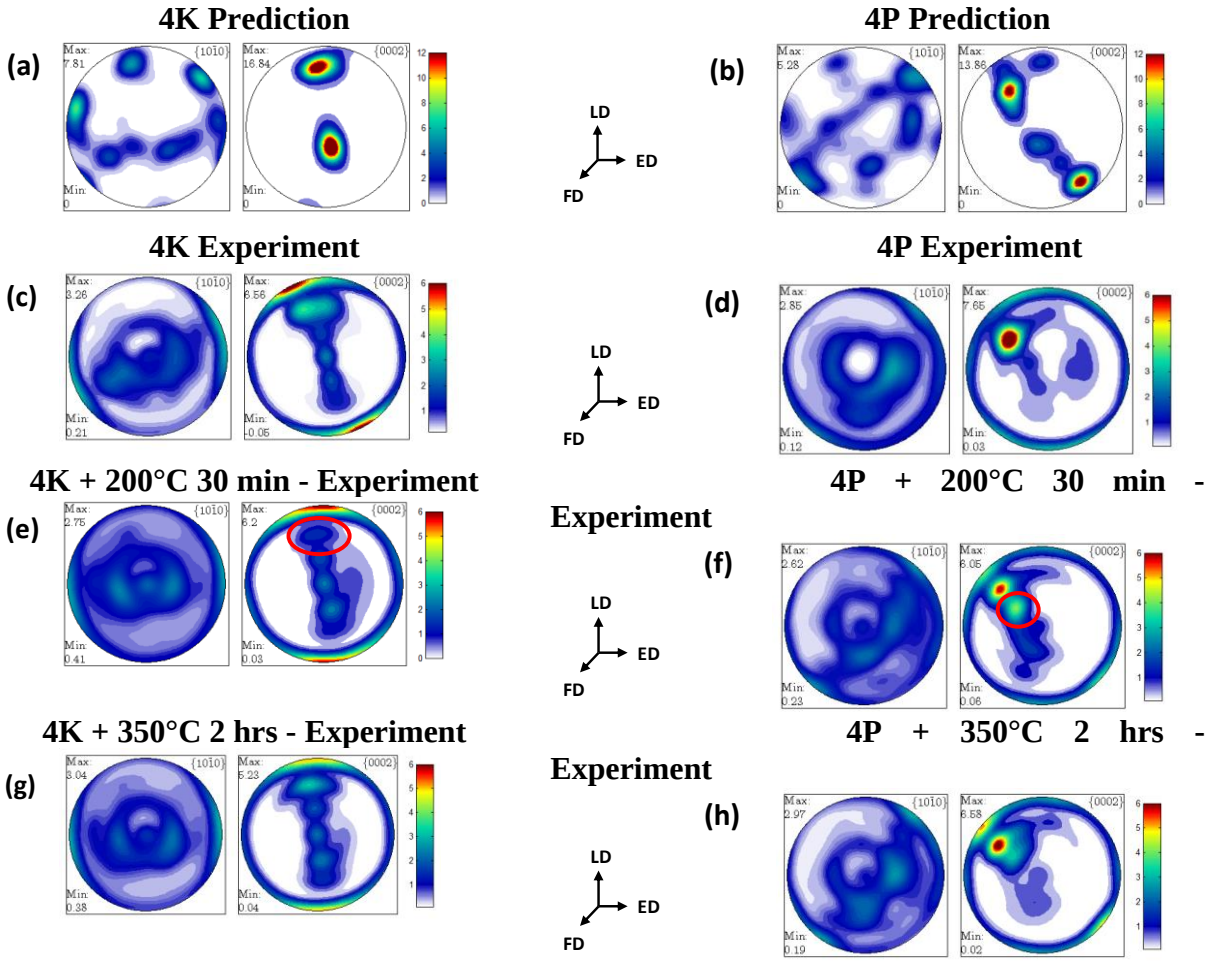


**Figure 4.16: Predicted VPSC pole figures for the designed ECAP Routes 4K (a) and 4P (b), and the corresponding experimental pole figures for the as processed ((c) and (d)) and after the annealing treatments of 200ºC 30 min (€ and (f)) and 350ºC 2 hours ((g) and (h)).**

Annealing treatments after ECAP should allow a closer representation of the VPSC predicted textures without grain refinement or recrystallization. Annealing at low temperatures for short time

durations should allow the grains to grow while maintaining the texture for that particular ECAP route removing microstructural size effects in the experimental AED measurements [23]. Three annealing conditions were tested for a single tensile orientation along the extrusion direction to confirm the changes in mechanical properties and overall microstructure. First chosen annealing treatment was 200$^{o}$C for 30 min. to remove stored dislocations present within the grains without significantly coarsening grains. Second and third annealing treatments were chosen as 350$^{o}$C for 2 hours and 24 hours respectively to ensure that grain growth occurs while removing the recrystallized grains within the microstructure. Two different durations were tested to see if grain growth continued after the first 2-hours.

Fig. 4.18 shows the experimental tensile tests of Route 4P along the extrusion direction (E) with the subsequent annealing treatments. The tensile samples were tested at a 5 x $10^{-4}$ $s^{-1}$ strain rate and deformed to ~10%-11% plastic strain. Comparison of the results of the Route 4P right after ECAP with those after the 200$^{o}$C, 30 min annealing showed a considerable decrease in yield strength from 133 MPa to 113 MPa which was expected due to the removal of stored dislocations [104]. $R_E$ also increased from 0.6 to 0.8 as can be seen in Fig. 4.16 (b). Increasing the annealing temperature to 350$^{o}$C also showed a further decrease in yield strength from 113 to 75 MPa, which was similar for both the 2 hour and 24-hour annealing times. This indicates that grain coarsening had reached a plateau by the 2-hour treatment and longer annealing times could result in a significant change in texture as compared to the original ECAP texture. The $R_E$ value did increase further from 0.99 to 1.06 with the longer heat treatment time which could have resulted from a texture change rather than just a grain size difference. It was concluded that the 200$^{o}$C, 30 min annealing heat treatment would only remove the remnant stored dislocations within the ECAP microstructure while the 350$^{o}$C, 2 hour annealing treatment would successfully remove most of

the refined and recrystallized grains in the microstructure and were both selected for the experimental AED measurements.

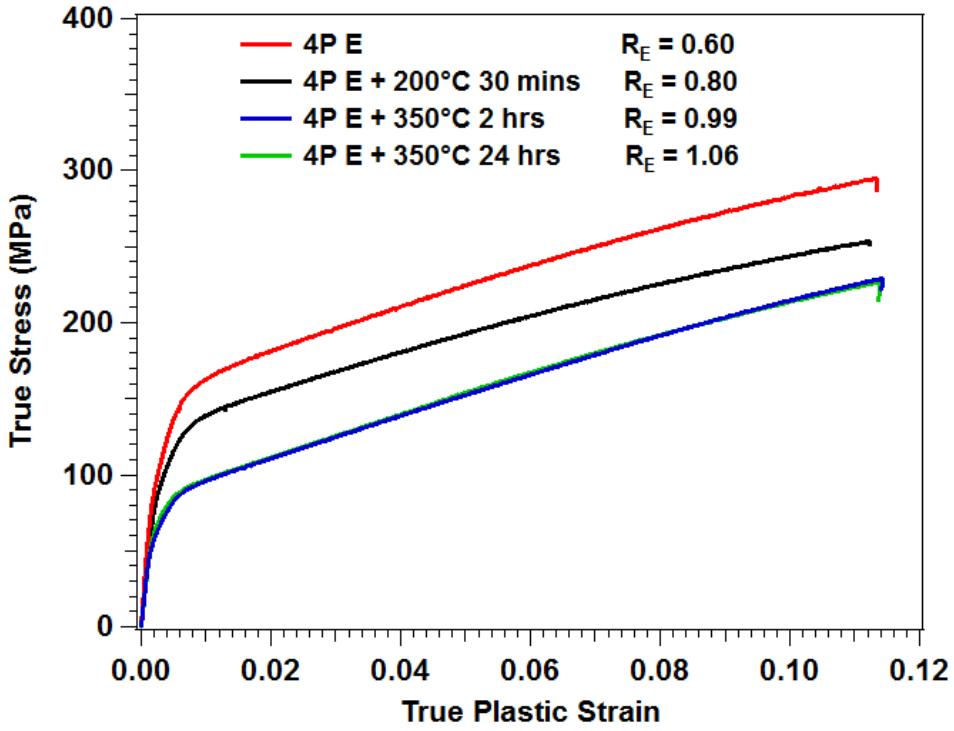


**Figure 4.17: Experimental tensile responses of the designed Route 4P along the extrusion direction (E direction) in four different conditions: as-processed ECAP (4P), after annealing at 200°C for 30 min, 350°C for 2 hours, and 350°C for 24 hours. All tensile tests were conducted at a strain rate of 5 x10$^{-4}$ s$^{-1}$. The $R_E$ values are also included in the legend.**

Considering only the experimental ECAP textures in Fig. 4.17, the annealing treatment 200°C 30 min shows a notable difference with the texture of the as-ECAP texture for both Routes 4P and 4K (marked in red). Route 4K exhibits a significant decrease in basal peak intensity while Route 4P displays a new peak intensity after annealing at 200°C (marked in red). Upon annealing at a

higher temperature, 350$^{o}$C for 2 hours, the annealing texture shows a closer match to the original as-ECAP texture for both Routes 4P and 4K. This difference in texture was reflected in experimental R-values and AED measurements as discussed below.

Comparing the experimental R-values and AED parameters in Fig 4.16 (a), the annealing condition 200°C, 30 min showed a decrease in $AED_{Exp}$ from 1.80 of the as-ECAP condition to 1.70. This is associated with the change in texture marked in Fig. 4.17 (e). Similarly, for Route 4P, Fig. 4.17 (b) showed a similar decrease in $AED_{Exp}$ from 2.20 to 1.82 due to the texture difference marked in Fig. 4.17 (f). The 350°C, 2-hour heat treatment increased the $AED_{Exp}$ from 1.80 of the as-ECAP condition to 1.89 and the texture shown in Fig. 4.17 (g) matches closely to the original ECAP texture in Fig. 4.17 (c). In contrast, for the Route 4P 350°C, 2-hour case exhibited a notable decrease in $AED_{Exp}$ from 2.20 to 2.04 even though the texture in Fig. 4.17 (h) matches the as-ECAP texture in Fig. 4.17 (d).

It can be concluded from this that the choice of annealing temperature can have a negative effect on formability even if performed for short times due to changes in texture. Furthermore, grain coarsening of ECAP processed AZ31 Mg alloy does not necessarily benefit formability but is more reliant on the texture alterations during annealing. To summarize, annealing treatments on ECAP processed AZ31 Mg alloy do not lead to a general direct improvement in $AED_{Exp}$ but rather a more complex relationship exists which requires assessing texture and microstructure of the material including the effects of dynamically recrystallized grains, dislocation densities and grain size.

Although VPSC simulations do not take dynamic recrystallization and grain refinement into account, some predicted R-values are still comparable to the experimental results. Fig 4.16 (a) shows the predicted R-values for Route 4K where the predicted R-values for 4 orientations match

well with the 350°C 2-hour heat treatment condition. The $R_{EL}$ value was predicted to be far lower than the actual experimental result which drove the $AED_{Predict}$ to a much higher value of 2.15. In Fig. 4.16 (b), predicted R-values for route 4P does not match well with the experimental $R_E$, $R_F$ and $R_{FL}$ values, with much lower predicted values than those for the 350°C, 2-hour condition which again drives the $AED_{Predict}$ to 3.10 which is much higher than the $AED_{Exp}$ of 2.04. This demonstrates that although the VPSC model can predict the trends in AED parameter, it lacks accuracy and new models that take dynamic grain fragmentation and recrystallization into account are needed to better predict the AED parameters in many cases.

Recent updates to the VPSC model have incorporated calculation of stress fluctuations within grains which accounts for the dispersion in misorientation within a single grain [82, 83, 90]. This allows the new VPSC model to predict if a grain will split based on a critical misorientation angle difference, or in other words, will the grain fragment or refine [83, 90]. The difference in predicted and experimental textures in Fig. 8 shows the importance of using grain fragmentation to model ECAP or any other type of severe plastic deformation processing. Moreover, during ECAP at 200$^{o}$C, dynamically recrystallized grains tend to nucleate along grain boundaries [16, 28, 58]. New grains develop in locations of high strain energy differences between two sides of a moving grain boundary such as the locations within shear or transition bands [82]. This effect was also not considered in the current VPSC model which could lead to additional texture differences observed between experimental and simulated results.

### 4.4 Anisotropy Effect on Ductility

Fig. 4.19 shows the tensile stress-strain plots for the ECAP Route 4K and 4P samples annealed at 350°C for 2 hours along all five directions (E, F, EF, EL and FL). The same samples used for

the R-value measurements in Fig. 4.16 were strained to failure. This was done to demonstrate if $AED_{Exp}$ index values could be correlated with the ductility trends in tension tests. It was expected that since the difference in $AED_{Exp}$ between the Route 4K and 4P after 350°C, 2-hour treatment (1.89 vs. 2.04, respectively) is not significant, the overall ductility of the samples from these routes should be very similar. The average elongation to failure for Route 4K for all orientations was 0.206 +/- 0.014 while for Route 4P it was slightly higher at 0.208 +/- 0.019. In comparison the average elongation to failure of rolled AZ31 alloy at room temperature for N, T and NR orientations was ~ 0.15 with an AED parameter of ~1.70 to 1.95 [28, 44]. This indicates a significant improvement in ductility after designing ECAP routes using the inverse optimization method.

Any deviations from AED index-based projections mean that the ductility of hcp alloys is more complex than can be inferred based on net plastic anisotropy alone. In other words, crystallographic aspects may come into play. For example, Selvarajou et al. [105] have discussed the role of twinning leading to symmetry breaking and void sharpening from twin boundary-void surface intersections. Depending on the twin boundary misorientation, the twin boundaries could lead to localized deformations that affect void growth and coalescence, particularly at low to intermediate stress triaxialities.

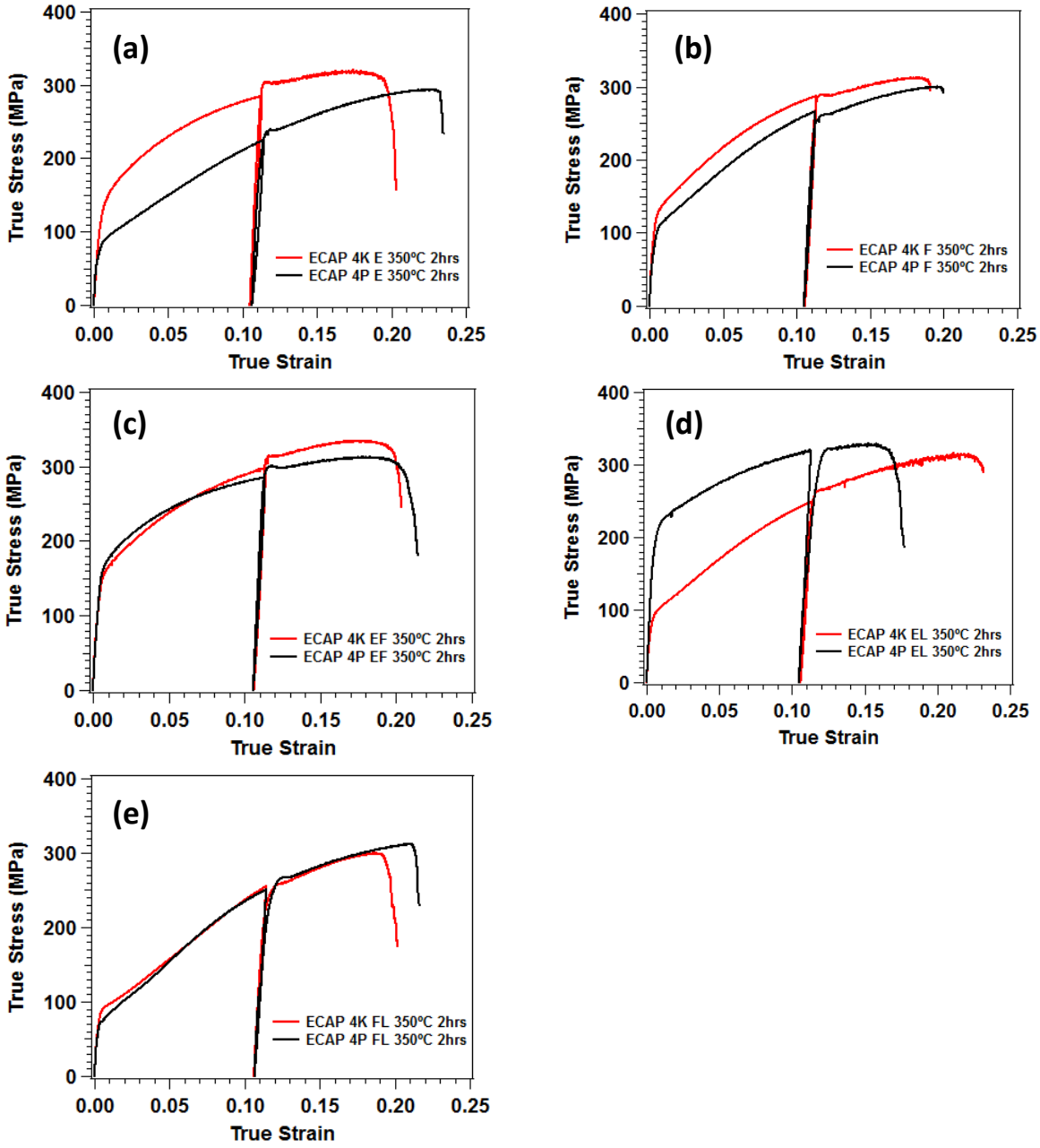


**Figure 4.18: Room temperature tensile true stress vs. strain plots to failure for the designed ECAP Routes 4K and 4P after 350°C, 2 hour annealing treatment along five sample directions (refer to Fig. 1) (a) E, (b) F, (c) EF, (d) EL and (e) FL. Strain drop at 0.10 was associated with the R-value measurements at this strain increment for each sample.**

## 4.5 Summary and Conclusions

In this work, an inverse optimization framework based on Sequential Quadratic Programming (SQP) was used to design severe plastic deformation (SPD) processing paths to improve the room temperature formability of the Mg-3Al-1Zn (AZ31) alloy. Equal Channel Angular Processing (ECAP) was chosen as the SPD technique to test the success of the optimization and alter crystallographic texture and mechanical properties. The Visco-Plastic Self Consistent (VPSC) crystal plasticity model was used to simulate and predict routes from the inverse optimization process. In order to quantify formability using the anisotropy of textured magnesium, a single invariant coefficient called the anisotropy effect on ductility (AED) index was used to account for the overall ductility of the processed Mg alloy using orientation specific R-value measurements in experiments and simulations. The SQP method was also used to calibrate the VPSC crystal plasticity model using multiple known experimental tensile tests and ECAP textures to create a much more robust Mg calibration for the 25$^{o}$C and 200$^{o}$C temperature cases compared to prior work. The AED formability index was accurately predicted with VPSC crystal plasticity model for known routes 4A and 4C and the original rolled Mg AZ31 alloy. This is the first time VPSC plasticity model was used to show a correlation between AED formability parameter and experimental AED results. This robustly calibrated VPSC crystal plasticity model was used with the inverse optimization approach, which explored over 1089 possible ECAP route combinations to maximize the formability of Mg alloys. This extent of exploration would be prohibitive using conventional simulations and experimental methods. Two routes with highest and lowest predicted AED values were taken, 4P ($AED_{Predicted}$ = 3.10) and 4K ($AED_{Predicted}$ = 2.16) and compared with experimental results to show some inaccuracies in AED formability trends and texture predictions. This was due to the lack of recrystallization and grain fragmentation considerations in the VPSC

crystal plasticity model, which is known to be present during ECAP. Both ECAP routes with similar experimental AED parameters resulted in extended elongation to failure where route 4K showed a strain to failure of 0.206 +/- 0.014 with an AED of 1.89 and route 4P with a strain to failure of 0.208 +/- 0.019 with an AED of 2.04. Both ECAP routes with post-annealing showed an improvement in ductility as compared to the original rolled condition of Mg AZ31 alloy with an average elongation to failure of ~0.15 strain with an AED of ~1.70 to 1.95.

This study presented one example of the inverse optimization method with ECAP using VPSC model but can also be used with higher fidelity versions of VPSC model or other crystal plasticity models, that can take grain fragmentation and dynamic recrystallization into account, to provide better optimized hybrid processing routes combining rolling, extrusion and ECAP. It is also possible to employ more flexible ECAP route designs with circular die implementation in experiments. This should cover a higher range of formability control on Mg alloys.

# CHAPTER V

# ODF TEXTURE OPTIMIZATION AND VPSC HALL PETCH EFFECT WITH VPSC GRAIN FRAGMENTATION MODEL

## 5.1 Voce Hardening Calibration of VPSC Grain Fragmentation Model using ODF optimization

Due to the texture prediction issues that arose in Chapter 4 a new optimization method needs to be introduced that is more accurate at predicting ECAP texture. Using the VPSC grain fragmentation model along with Orientation Distribution Function (ODF) optimization were tried as possible solution to reduce the error for predicted textures in VPSC crystal plasticity model. This will also provide a conclusion if using processed texture results is necessary to calibrate voce hardening parameters for future VPSC simulations. Figure 5.20 (a-d) shows the experimental XRD measurements of prismatic $(10\bar{1}0)$ and basal (0002) plane systems for 4K, 4P, 4C and 4A. To compare each possible optimization technique three different paths were chosen for voce parameter recalibration of the model, VPSC mechanical optimization from Chapter 4 would be the control group and starting point for our texture optimization, VPSC ODF Optimization with the new optimization objective function will be the second method and the ODF optimization with the new VPSC crystal plasticity Grain Fragmentation model will be the final method.

The original VPSC mechanical optimization method was used to calibrate the voce hardening parameters for 200$^{o}$C rolled tensile tests for three orientations, Normal, Transverse, and 45$^{o}$ between Normal and Rolled direction. All orientations showed good agreement of simulated tensile tests and experimental tensile tests as shown before. The calibrated voce hardening parameters for the mechanical test optimization are shown in Table 4.8. The mechanical objective

function shows good promise in reducing error between experimental and simulation tensile tests for multiple orientations. Figure 5.20 (e-h) shows the mechanical calibrated Voce hardening parameters used to simulate 4 ECAP pass route systems with the specified rotations for each route. The textures for all route cases show a significant disagreement with experimental results, where very discrete peaks are observed for all predicted VPSC textures. Predicted VPSC 4K and 4P results also shows the emergence of new peaks which were not present in the experimental textures.

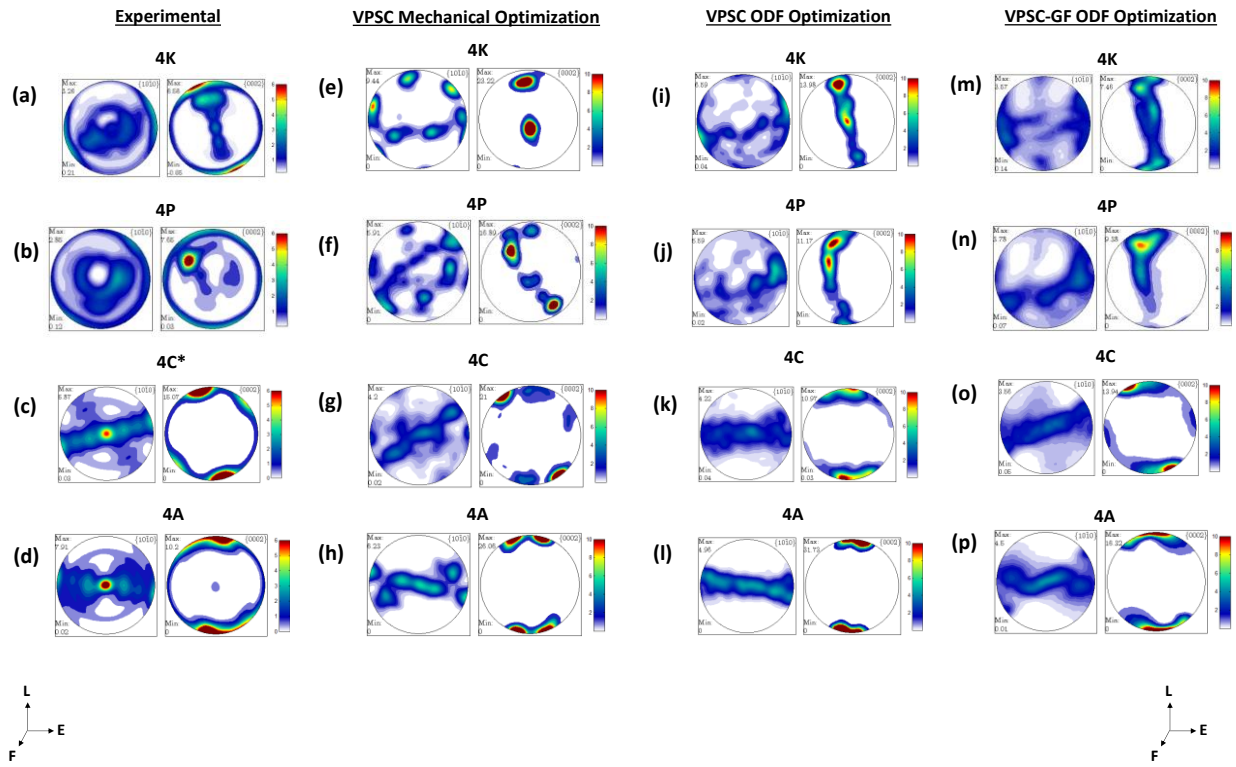


**Figure 5.19: (a-d) Experimental column of textures for routes 4A, 4P , 4C and 4K. (e-h) VPSC predicted textures from mechanical test calibration (i-l) VPSC simulated texture from ODF optimization. (m-p) VPSC Grain fragmentation simulated texture from ODF optimization.**

***Route 4C texture was slightly reoriented by 30º to ensure Extrusion direction is lined up with axes used in this figure.**

Moving on to VPSC (No Grain Fragmentation) ODF Optimization using Equation 2.7, Figure 5.20 (i-l) shows the ODF optimized texture of the same routes. Here the simulated VPSC results show much better agreement with experimental results with 4K and 4P, However, 4C and 4A still show a great discrepancy in the distribution of peaks simulated by the VPSC along the longitudinal direction. This may be due to the misorientation averaging conducted by the original VPSC model discussed before.

Table 5.12 shows the calibrated voce hardening parameters for the VPSC optimization method which has changed considerably with the mechanical optimization parameters in Table 5.11. However, the ODF optimized voce hardening parameters were used to plot the Mg AZ31 rolled condition and was observed to still agree with the experimental mechanical tests very well as shown in Figure 5.21 and can be disregarded being an issue. This shows ODF optimization may be a better optimization method than just doing mechanical optimization in terms of texture processing and mechanical test simulations. This also shows how VPSC can have multiple solutions to voce hardening parameters and sometimes an optimization function can do a better job than a human counterpart in calibrating these parameters. There may be solutions unexplored by the user in these circumstances with so many possible outcomes.

**Table 5.11: Voce hardening parameters derived using tensile curve fitting optimization of Rolled Mg AZ31 200°C mechanical tests along three orientations (N, T, RN) with the VPSC model.**

| Deformation Systems | $\tau_o$ (MPa) | $\tau_1$ (MPa) | $\theta_o$ (MPa) | $\theta_1$ (MPa) |
|---|---|---|---|---|
| Basal | 14.0 | 14.5 | 348.6 | ~0 |
| Prismatic | 82.4 | 40.0 | ~0 | ~0 |
| Pyramidal <c+a> | 72.5 | 9.4 | 121.9 | ~0 |
| Extension Twinning | 99.3 | ~ 0 | ~0 | ~0 |
| Contraction Twinning | 112.0 | 83.2 | 1261.0 | ~0 |

**Table 5.12: Voce hardening parameters derived using ODF texture fitting optimization using experimental ECAP Mg AZ31 at 200°C for routes 4K ,4P, 4A and 4C with the VPSC Model**.

| Deformation Systems | $\tau_o$ (MPa) | $\tau_1$ (MPa) | $\theta_o$ (MPa) | $\theta_1$ (MPa) |
|---|---|---|---|---|
| Basal | 3.0 | 6.0 | 311 | ~ 0 |
| Prismatic | 153 | 26.9 | ~ 0 | ~ 0 |
| Pyramidal <c+a> | 70.8 | 2.87 | 161.0 | ~ 0 |
| Extension Twinning | 170.0 | ~ 0 | ~ 0 | ~ 0 |
| Contraction Twinning | 170.0 | ~ 0 | 1372.5 | ~ 0 |

(a) VPSC Mechanical Optimization (b) VPSC ODF optimization

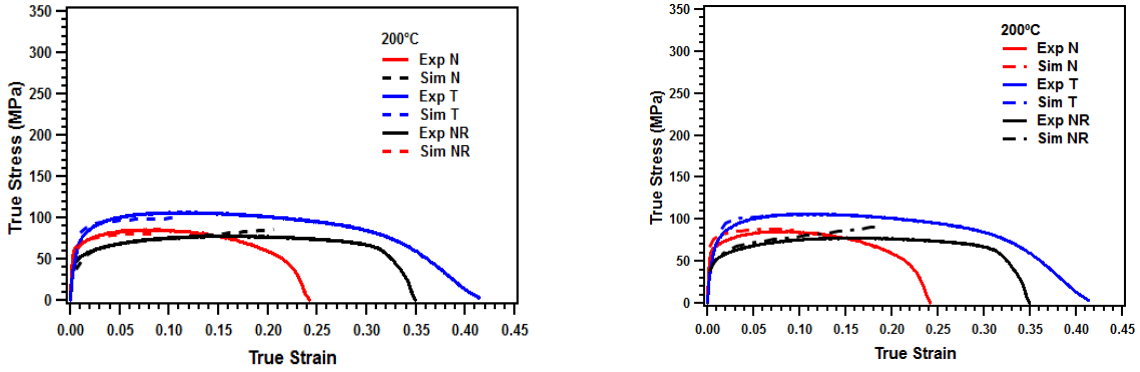


**Figure 5.20: Experimental Rolled Mg AZ31 tensile tests at 200°C with (a) mechanical test calibration using optimization and (b) the simulated mechanical response at 200C of the Voce hardening parameters using ODF optimized Voce hardening parameters still showing good agreement with experimental tensile results.**

Finally, Fig. 3 (m-p) shows the VPSC-GF ODF optimization which resulted in the best agreement between experimental and simulation texture results. 4P, 4K , 4C and 4A show very good agreement with the correct density peaks at the correct locations in the pole figure. Some issues still arise with prismatic pole figures for 4P and 4K where some central densities are missing from the simulated textures but did not show that much disagreement with the basal pole figures. Overall, the improvement was significant. Table 5.13 shows the voce hardening parameters did not change between the VPSC and VPSC-GF ODF optimizations. This also makes sure the mechanical rolled tensile test fits remained the same since grain fragmentation does not occur extensively in mechanical tests and does not change the mechanical simulation for 200$^{o}$C.

**Table 5.13: Voce hardening parameters derived using ODF texture fitting optimization using experimental ECAP Mg AZ31 at 200$^{o}$C for routes 4K ,4P, 4A and 4C with the new VPSC Grain fragmentation model**.

| Deformation Systems | $\tau_o$ (MPa) | $\tau_1$ (MPa) | $\theta_o$ (MPa) | $\theta_1$ (MPa) |
|---|---|---|---|---|
| Basal | 3.0 | 6.0 | 311 | ~ 0 |
| Prismatic | 153 | 26.9 | ~ 0 | ~ 0 |
| Pyramidal <c+a> | 70.8 | 2.87 | 161.0 | ~ 0 |
| Extension Twinning | 170.0 | ~ 0 | ~ 0 | ~ 0 |
| Contraction Twinning | 170.0 | ~ 0 | 1372.5 | ~ 0 |

To ensure the ODF error is not just qualitatively represented by only pole figures, The ODF errors were normalized over the integral of the experimental ODF to get a percentage error of route Y, as shown in Equation 5.11, to produce a quantifiable error plot between all the optimization methods, shown in Figure 5. This shows a considerable reduction in percentage error with the change from mechanical optimization to ODF optimization. The last step with the VPSC grain

fragmentation model to show an even bigger improvement where second misorientation calculations represented texture with a higher accuracy level than what was ever done before with ECAP Mg Alloys. This shows how powerful the new grain fragmentation VPSC addition is to high strain processing simulations. This study only showed one case but can also be extended for other high deformation processing methods such as simple rolling, dynamic rolling, extrusions, wire drawing etc.

$$\left( ODF^{Y}_{Percentage\ Error} \right) = \frac{\left| \int ODF_{Exp} - \int ODF_{Sim} \right|}{\int ODF_{Exp}} \times 100 \qquad \text{Equation (5.11)}$$

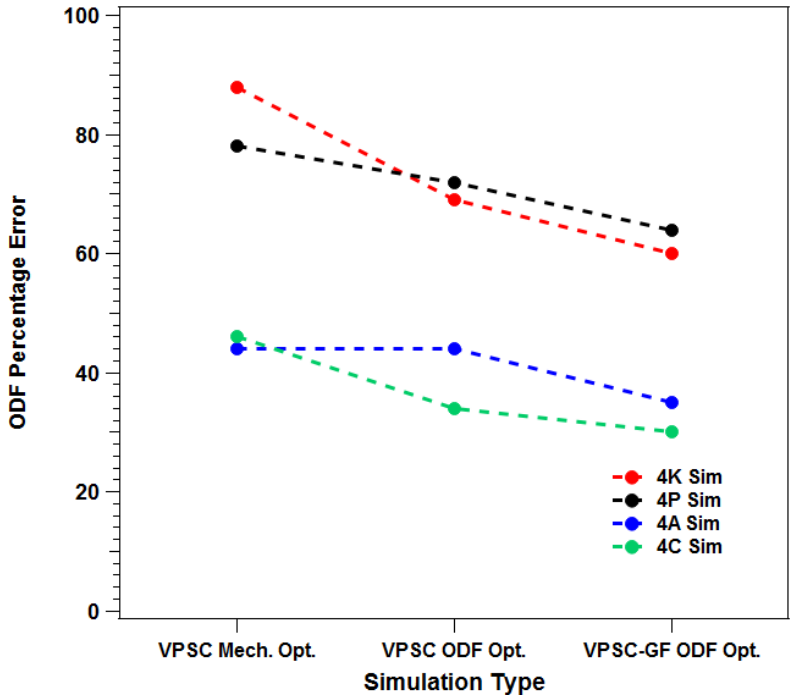


**Figure 5.21: ODF percentage error as a function of each optimization method for routes, 4K, 4P , 4C and 4A.**

## 5.2 Hall Petch effect Implementation with VPSC Grain Fragmentation Model

In order to show the self and latent hardening effect present in VPSC is not appropriate for ECAP processing, the VPSC 4K Route was used to show the evolution of voce hardening parameters and mechanical tests in VPSC-Grain Fragmentation model. Figure 5.23 (a) shows the tensile test of the 4K ECAP texture along the Flow direction using the initial 25$^{o}$C rolled voce hardening parameters. This provides an initial starting point reference of no hardening present in the material. The Experimental 4K ECAP route is also shown for comparison. The rolled 200$^{o}$C CRSS values were then tracked in VPSC to get the dislocation hardening (DH) effect after ECAP, this is already built into VPSC that measures the self and latent hardening of the material mentioned before. The difference between the evolved hardening parameters were then taken and added to the original 25$^{o}$C rolled hardening parameters as shown in Table 5.14. The hardening effect barely increases the yield point of the tensile curve as shown in Figure 5.23 (b), where the hardening effects in VPSC does not reflect the actual experimental hardening observed for ECAP Mg AZ31.

(a) (b)

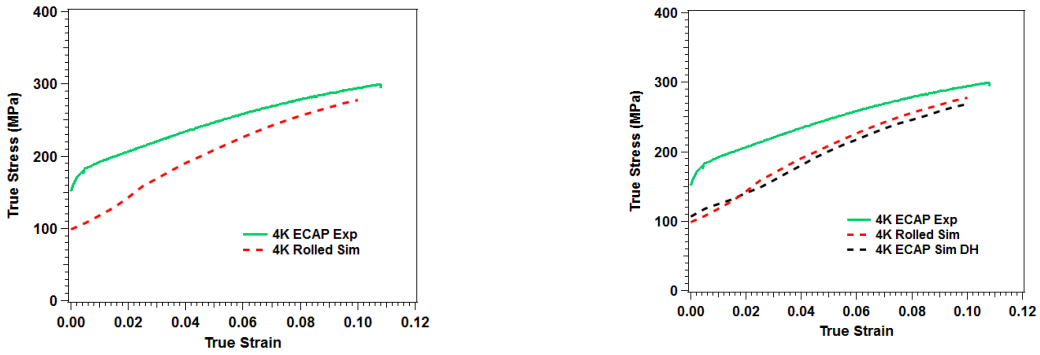


**Figure 5.22 (a): Experimental and VPSC simulated tensile test along F direction of ECAP 4K material at room temperature and (b) VPSC simulated tensile test after with dislocation hardening after ECAP**

**Table 5.14: CRSS $\tau_0$ Voce hardening parameter evolution from rolled Mg to after ECAP for the 4K condition**.

| Deformation Systems | $\tau_0$ (MPa) 200°C Rolled [Column 2] | $\tau_0$ (MPa) after ECAP 200°C 4K [Column 3] | $\tau_0$ (MPa) 25°C Rolled [Column 4] | $\tau_0$ (MPa) ECAP 25°C 4K CRSS hardening [Column (3-2)+4] |
|---|---|---|---|---|
| Basal | 3.0 | 10.1 | 10.0 | 17.10 |
| Prismatic | 153 | 156.2 | 110.0 | 113.2 |
| Pyramidal <c+a> | 70.8 | 73.8 | 255.0 | 258 |
| Extension | 170.0 | 171.3 | 55.0 | 56.3 |
| Contraction | 170.0 | 171.8 | 130.0 | 131.8 |

In order to introduce the Hall Petch effect first, the voce hardening parameters need to be calibrated for known ECAP mechanical tests which includes 4K and 4P. Then the CRSS increase could be related to grain fragments (grain size) within the VPSC grain fragmentation model.

Figure 5.24 and 5.25 shows the 4K and 4P VPSC tensile fit after the voce hardening calibration using the SQP mechanical optimization method shown previously. The only difference

in the optimization objective function is the additional orientation of the ECAP material (E,F,EF,FL,EL) and the inclusion of the PTR twinning control parameters A1 and A2 for extension and contraction twinning in the calibration process. The experimental tests are also shown for comparison. The 4K shows decent agreement after optimization of the voce hardening parameters in all orientations. However, the 4P, E orientation did not show good agreement with the model. Changing the voce hardening parameters by hand revealed changing the E orientation to fit better resulted in a larger error along other orientations so the best fit for all orientations was achieved by the optimization model. The final $\tau_o$ voce hardening parameters for all 4P and 4K slip and twin systems are shown in Table 5.15 for 4P and 4K separately. Table 5.17 shows the $\tau_1$, $\theta_o$, and $\theta_1$ voce hardening parameters that has been averaged for both 4P and 4K route since they were very similar and did not show a significant Hall-Petch correlation on $\tau_1$, $\theta_o$, and $\theta_1$.

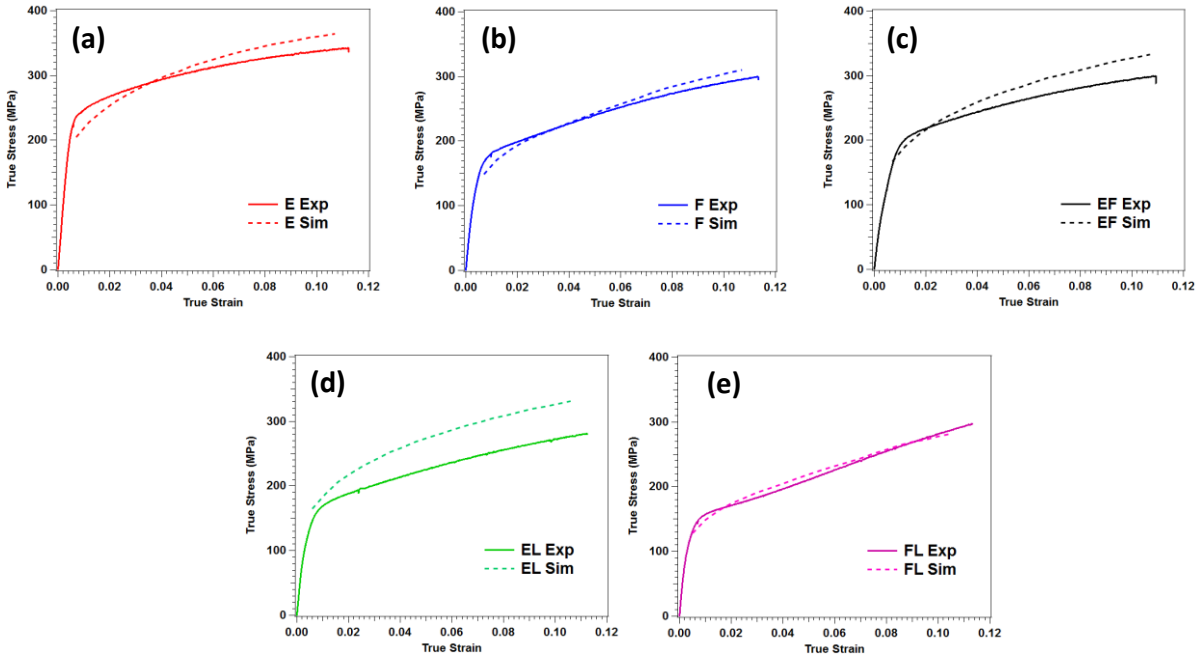

**Figure 5.23: ECAP mechanical optimization of 4K ECAP route at room temperature with VPSC optimization fits for (a) E, (b) F, (c) EF, (d) EL, and (e) FL orientations.**

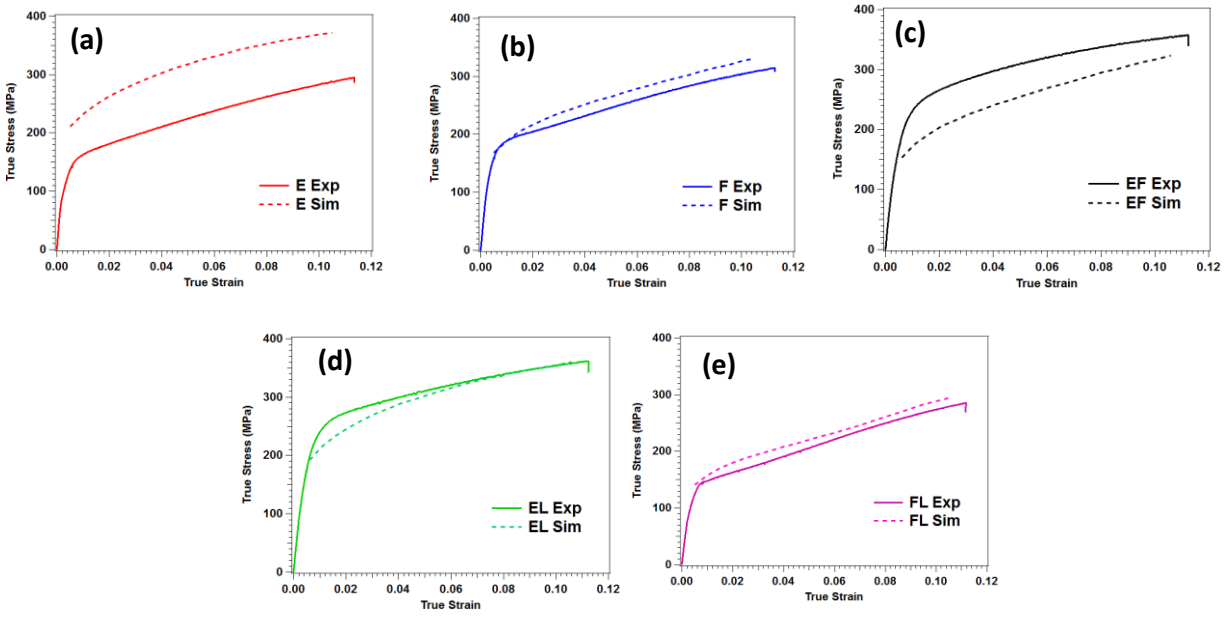


**Figure 5.24: ECAP mechanical optimization of 4P ECAP route at room temperature with VPSC optimization fits for (a) E, (b) F, (c) EF, (d) EL, and (e) FL orientations.**

**Table 5.15: $\tau_0$ voce hardening parameter of routes 4K and 4P after mechanical optimization.**

| Deformation Systems | $\tau_0$ (MPa) 4K | $\tau_0$ (MPa) 4P |
|---|---|---|
| Basal | 17.10 | 17.10 |
| Prismatic | 137.1 | 161.2 |
| Pyramidal <c+a> | 258 | 258 |
| Extension | 122.5 | 131.0 |
| Contraction | 151.3 | 155.0 |

**Table 5.16: $\tau_1$, $\theta_o$, and $\theta_1$ average voce hardening parameters of both routes 4K and 4P after mechanical optimization.**

| Deformation Systems | $\tau_1$ (MPa) | $\theta_o$ (MPa) | $\theta_1$ (MPa) |
|---|---|---|---|
| **Basal** | **60.48** | **1574.0** | **27.4** |
| **Prismatic** | **133.9** | **6552.0** | **~ 0** |
| **Pyramidal <c+a>** | **294.0** | **9659.0** | **~ 0** |
| **Extension** | **~ 0** | **4.60** | **~ 0** |
| **Contraction** | **125.0** | **1000.0** | **~ 0** |

Fig. 5.26 shows the final 4K texture result with the additional Hall Petch effect for the introduced through calibration. This shows the difference the Hall-Petch effects the VPSC grain fragmentation model will be able to demonstrate during ECAP processing. After establishing $\tau_o$ values for 4P and 4K after ECAP for mechanical tests the number of grain fragments in VPSC was related to the CRSS increase. 4P, 4K and Rolled condition grain sizes (marked with *) were experimentally measured and plotted in Fig. 5.27 with the number of VPSC grain fragments. 4A, 4C and 4Bc were later added to the plot for comparison.

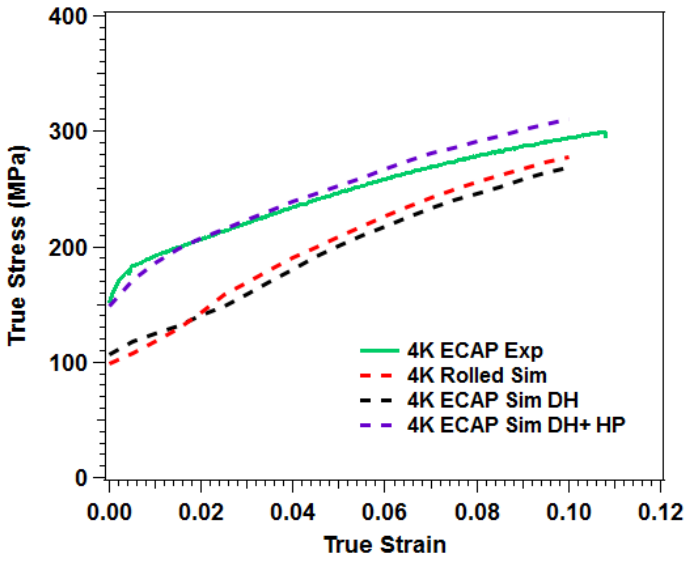


**Figure 5.25: 4K ECAP tensile test at room temperature along F direction with VPSC mechanical optimization calibration to portray the full Hall Petch hardening effect.**

The Hall-Petch equation for the CRSS of each slip and twin system (i) can be written as Equation 5.12, where $\tau_d^i$ is the CRSS of the ECAP material with grain size (d), the $\tau_{rolled}^i$ is CRSS of the rolled material, $\tau_{Dislocation-Hardening}^i$, is the CRSS increase from the dislocation hardening (self and latent hardening) after ECAP and k is the Hall-Petch slope. $\tau_{rolled}^i + \tau_{Dislocation-Hardening}^i$ term represents the y-intercept of the Hall-Petch equation. Figure 5 (a) shows the Hall-Petch plot of basal, prismatic, extension twinning and contraction twinning deformation systems. Pyramidal slip does not occur at room temperature, so it was excluded in this plot.

$$\tau_d^i = \left[\tau_{rolled}^i + \tau_{Dislocation-Hardening}^i\right] + (k^i)(d^{-0.5}) \quad \text{(Equation 5.12)}$$

Figure 5.28 (a) shows the Hall-Petch plots for basal, prismatic, extension twinning and contraction twinning for mg alloys as function of grain size ($d^{-0.5}$) for the VPSC simulated mechanical tests. The 25-um grain size was taken for the rolled Mg AZ31 material. Figure 5.28 (b) shows the experimental results measured by Dogan and Razavi [16, 58, 65] to compare with experimental

results. In terms of CRSS values the simulated values are much lower than the experimental counterpart for all slip and twin systems. However, the trends for the Hall Petch effect still holds for each deformation system. Extension twinning being the most dependent on grain size, prismatic coming second and basal slip was the least dependent on grain size.

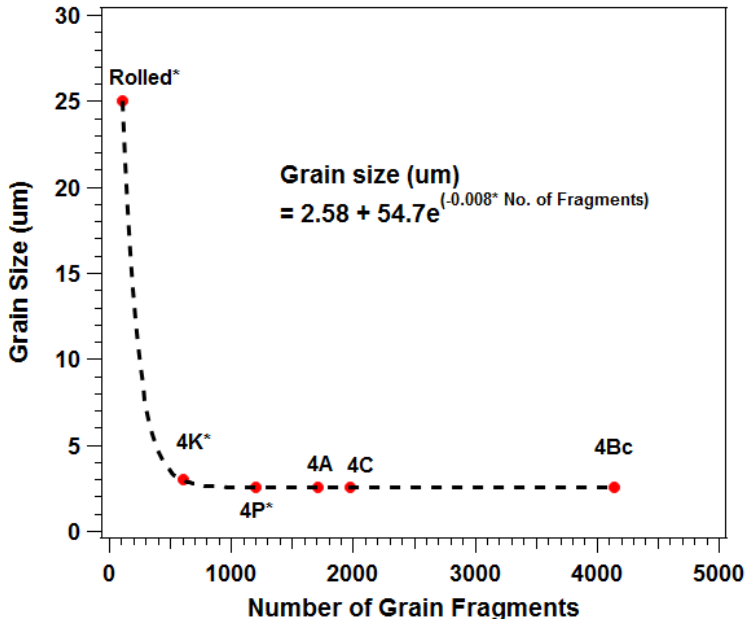


**Figure 5.26 : Power law relationship of Grain size to Number of grain fragments in VPSC.**

***Routes used for fitting the power law equation**

(a) (b)

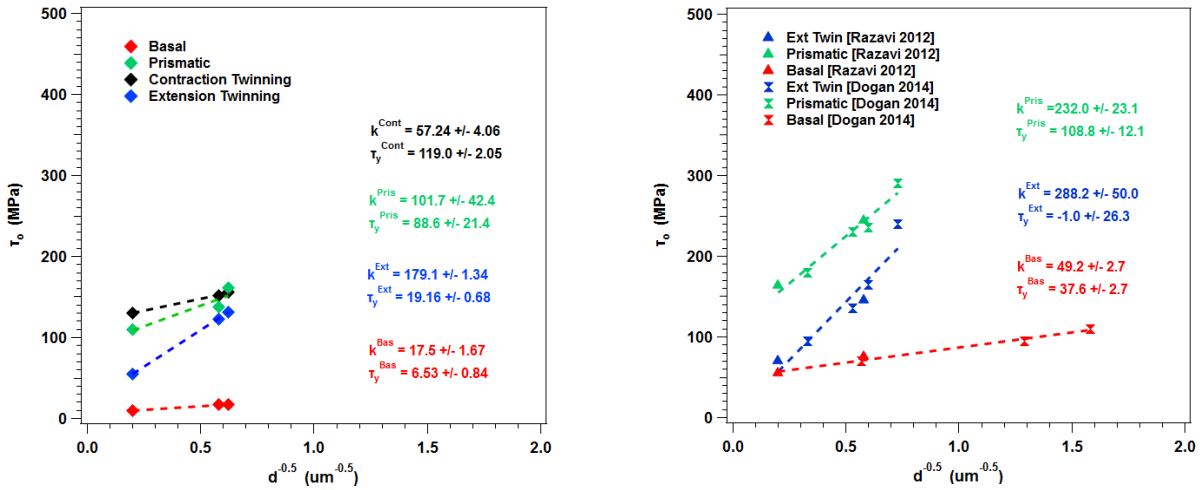


**Figure 5.27 Hall-Petch plots for basal, prismatic, extension and contraction twinning for (a) simulated VPSC grain fragmentation model and (b) experimental results. Contraction twin CRSS data was not found in experimental data.**

## 5.3 AED predictions with VPSC Grain fragmentation with new Dislocation hardening and Hall Petch model

The VPSC Grain Fragmentation Model with the latest Dislocation hardening and Hall Petch (DH+HP) relationship was used to predict the AED parameters of 4P and 4K to see if any improvement in accuracy of R-values and AED parameter had occurred. Figure 5.29 shows the experimental R-values along each orientation with its AED value for ECAP routes 4K and 4P. The dotted green line shows the R-value of the predicted results from the new VPSC model which shows much better agreement in terms of R-values most orientations including a much better conservative prediction of AED compared to before. The trend however is slightly different where 4P AED is predicted to be lower than 4K which is unfortunately the opposite correlation observed in experiments. This calculation of R-values in VPSC need to be explored further in the future

work to ensure there is no issue with the VPSC Lankford calculations for anisotropic materials. Another case could be the lack of recrystallization in the VPSC model for further improvement in the accuracy of the model could deem it more viable in predicting the complexities of the ECAP microstructure more accurately. However, these AED and R-value predictions are much more accurate than what was proposed earlier and was used to do the final attempt on the inverse optimization to design new route systems.

(a) (b)

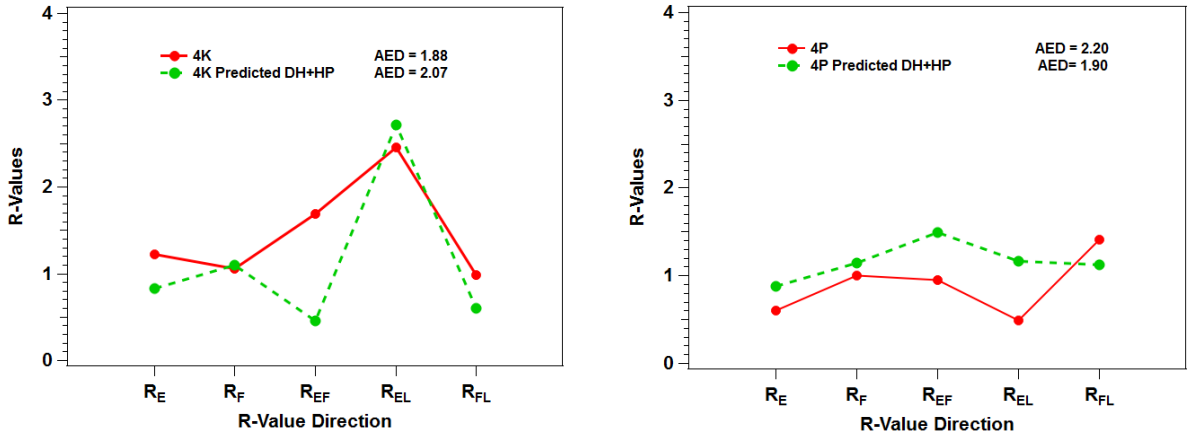


**Figure 5.28: Experimental R values for the tensile directions of E, F, EF, EL and FL at ~10%-11% plastic strain for the designed Routes 4K (a) and 4P (b), The plots also include the predicted R-values for the same routes. Corresponding experimentally determined and predicted AED parameters are also included in the legends.**

## 5.4 Inverse Optimization ECAP Route prediction using VPSC Grain Fragmentation with new Dislocation hardening and Hall Petch model

Four initial rotations along the extrusion direction were pre-defined as initial conditions before each optimization process, as shown in Table 2.3. The initial rotations were selected based on the three main ECAP routes commonly used in the past: Route A, Route C, and Route $B_c$ (+90$^o$ rotation between ECAP passes). Table 5.17 lists several combinations of 0$^o$, 90$^o$ and 180$^o$ rotations along

the extrusion direction as initial conditions in order to find a globally optimized ECAP route solution.

The results after inverse optimization are shown in Table 5.18. Most initial conditions after optimization went towards a 4A route (with a rotation of **0º, 0 º,0 º, 0 º** along Extrusion direction) with an $AED_{Predicted}$ of 2.47. This suggests 4A has a large local minima spot in the AED Error objective function and does not represent the global optimal. This can be confirmed when 90º fixed condition was used for Rotation 1 the optimized routes with higher $AED_{predicted}$ were derived by the model. In particular, route 4L with an $AED_{Predicted}$ of 3.44 has a much higher AED than what has been noted before. The predicted VPSC textures for all these predicted routes are shown in Figure 5.30. It can be concluded the SQP optimization process still suffers from local minima optimization and a more robust Bayesian method may have to be considered to find the actual global minima of this complex 4-dimensional objection function.

**Table 5.17: Inverse optimized routes with latest calibrated VPSC Grain Fragmentation Model with Hall Petch and Dislocation Hardening.**

| Route Name (GF+DH+HP) | Rot * 1 (°) | Rot * 2 (°) | Rot *3 (°) | Rot * 4 (°) | $AED_{Predicted}$ | Number of Iterations |
|---|---|---|---|---|---|---|
| 4G | 0 | 0 | 0 | 0 | 2.47 | 73 |
| 4H | 0 | 0 | 0 | 0 | 2.47 | 167 |
| 4I | 0 | 0 | 0 | 0 | 2.47 | 105 |
| 4J | 0 | 0 | 0 | 0 | 2.47 | 79 |
| 4K | 90 fixed | 0 | 0 | 0 | 2.79 | 14 |
| 4L | 90 fixed | 177 | 22 | 0 | **3.44** | 157 |
| 4M | 90 fixed | 168 | 0 | 0 | 2.93 | 137 |
| 4N | 90 fixed | 0 | 0 | 0 | 2.79 | 191 |
| 4O | 90 fixed | 0 | 0 | 0 | 2.79 | 111 |

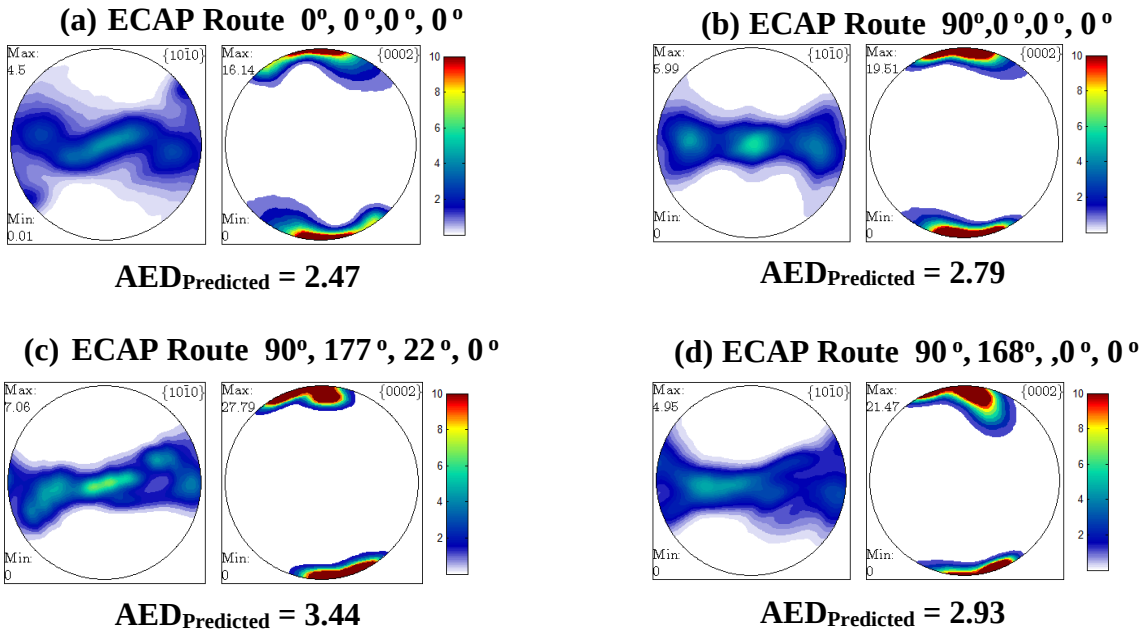


**Figure 5.29: Predicted Basal and Prismatic textures with superior AED predicted after inverse optimization. Route 90º, 177 º, 22º, 0 º shows the highest formability with an AED of 3.44**

## 5.5 Summary and Conclusion

ODF optimization method was shown to be very powerful tool in determining the voce hardening parameters to predict ECAP texture. Not only do mechanical tests need to be used for calibrating the VPSC crystal plasticity model but also texture when dealing with high strain processing simulations. Introduction of the Hall Petch effect for VPSC Grain fragmentation model was the first-time number of grain fragments were related to actual grain size of a simulated ECAP sample. This was then correlated to CRSS values of each slip and twinning system. The Hall-Petch plot matched very with experimental results in terms of mechanical properties after ECAP and AED prediction. This showed the VPSC model requires such models to predict ECAP processing in materials for future work.

# CHAPTER VI

# MAIN CONCLUSION AND FUTURE DIRECTIONS

## 6.1 Main Conclusions

1. The Sequential Quadratic Programming optimization method was used to calibrate the voce hardening parameters in Visco Plastic Self Consistent (VPSC) crystal plasticity model with great success. Using multiple orientation tensile data 20 voce hardening parameters were optimized for four different temperatures 25$^{o}$C, 100$^{o}$C, 150$^{o}$C, 200$^{o}$C. However specific initial conditions and constraints were needed to avoid local minima that would fail the optimization from converging to the correct solution. This does require further exploration into other optimization techniques for more efficient convergence.
2. This is the first time VPSC plasticity model was used to show a correlation between AED formability parameter and experimental AED results. This robustly calibrated VPSC crystal plasticity model was used with the inverse optimization approach, which explored over 1089 possible ECAP route combinations to maximize the formability of Mg alloys. This extent of exploration would be prohibitive using conventional simulations and experimental methods.
3. The Orientation Distribution Function (ODF) optimization process to calibrate Voce hardening parameters with experimental data was far more successful than the mechanical optimization process. This new optimization method further reduced the error of texture predictions of VPSC Equal Channel Angular Pressing.

4. The new VPSC Grain fragmentation with second order stress, misorientation and rotation calculations showed a much better agreement with experimental texture results, showing the least percentage ODF error compared to experiments for all ECAP route cases studied.
5. Introduction of the Hall Petch effect for VPSC Grain fragmentation model was the first-time number of grain fragments were related to actual grain size of a simulated ECAP sample. This was then correlated to CRSS value hardening of each slip and twinning system. The Hall Petch plot correlated very well with experimental results where prismatic slip and extension twinning were heavily dependent by grain size confirming experimental results.

**(e)** The Inverse optimization of AED with the final VPSC crystal plasticity model which combines Grain Fragmentation, Hall Petch and Dislocation hardening showed good success where two possible route solutions were discovered as possible routes with high formability. ECAP Route with a starting basal pole oriented along the extrusion direction were optimized to ECAP route 4L with rotations ( $90^{o}$, $177^{o}$, $22^{o}$, $0^{o}$ ) and 4N ECAP route with rotations ( $90^{o}$, $168^{o}$,$0^{o}$, $0^{o}$) with an $AED_{Predicted}$ = 3.44 and 2.93, respectively.

6. Conventional with a rotation of (90, 180, 0, 0) with an AED prediction of …. By the end of this study combining all the AED inverse optimization processes a total of over 1500 routes combinations were studied which would not be possible with conventional ECAP processes. This also provided a better idea of the possible range of AED formability possible in the 4 pass ECAP system.

### 6.2 Future Directions

The cup drawing experimental confirmation was not completed within this study and needs to be made priority for the next 2 years of the project. More Finite Element simulation data on Mg

AZ31 under the cup drawing process has been completed by Behrooz Bidabadi and Dr. Jywhen Wang which will aid the in confirming AED dependance on physical formability tests. The AED relation to earing effects limit flow diagrams, microstructure and texture orientation will also be conducted on the material. Currently 4 ECAP Plates with varying predicted AED parameters have been processed and cut and are ready for cup drawing at room temperature. The next sections are the preliminary results for the Finite element work on cup drawing and Inverse optimization prediction of ECAP Plate routes.

### 6.2.1 Preliminary Results for Finite Element of Cup Drawing

Controlling formability of ECAP plates are important to ensure sheet metal plates could be cut directly and be deep drawn to test its formability. A direct correlation between AED parameter and actual deep drawing parameters have never been experimentally conducted before, rather tensile test R-values have always been considered to test the AED theory indirectly.

One proof of concept was derived using Finite Element Analysis of Mg sheet by matching the simulated material properties with the exact R-value parameters predicted by the simulation tool. Finite element analysis (FEA) was conducted on ABAQUS CAE software to model the equivalent strain responses of cup drawing metal alloys sheets at ambient temperature. Strain localization in Mg AZ31 can lead to shear banding which leads to failure for these materials.

Fig. 9.31 shows the cup drawing model used for the simulation. This consists of a quarter section of the cup drawing setup. A larger section could not be used due to node constraints. The cup drawing setup is comprised of 4 parts, the metal sheet that is being drawn, the clamp that holds

down the top part of the sheet metal, the die that shapes the sheet metal into a cup and finally the punch that applies a constant displacement rate on the sheet metal.

The extrusion was conducted on a metal sheet with a diameter of 80 mm and a thickness of 1 mm and was drawn at a drawing ratio of 1.81. A fillet transition was placed on the die of 6.5 mm. Six boundary conditions (BCs) was applied on the model as shown in Table 9.18 where U represent translational displacements and UR represents rotational displacements. The punch was constrained to a constant downward displacement rate of 50 mm/s to deform the sheet. The time was set to 0.4 seconds resulting in a total drawing depth of 20 mm. This drawing depth was set to ensure if earing effects from the anisotropic Mg alloys could be observed during drawing. Furthermore, translational frictional coefficients were added to each contact point on the metal sheet. The punch and sheet metal surface were assigned a frictional coefficient of 0.1, the clamp and sheet metal were assigned 0.08 and the die and the sheet metal were assigned 0.05.

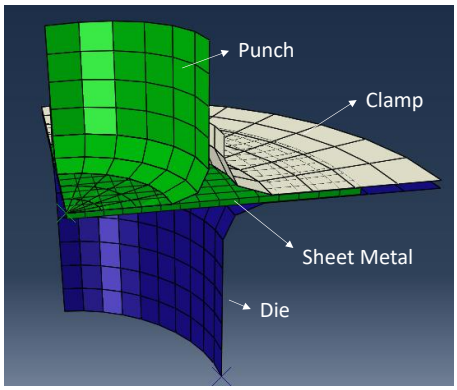


**Figure 6.30: Cup drawing model used for the FEA simulation comprised of four parts. The metal sheet was deformed at a constant displacement rate applied by the punch.**

**Table 6.18. Boundary conditions for the cup drawing model**

| Part | Boundary Conditions | | | |
|---|---|---|---|---|
| **Metal Sheet BC1** | Ux = 0 | URy = 0 | URz = 0 | |
| **Metal Sheet BC2** | Uz = 0 | URy = 0 | URx = 0 | |
| **Die** | Ux,URx = 0 | Uy,URy = 0 | Uz,URz = 0 | |
| **Clamp** | Ux,URx = 0 | Uy,URy = 0 | Uz,URz = 0 | |
| **Punch** | Ux,URx = 0 | URy = 0 | Uz,URz = 0 | Uy = -50 mm/s |

The Mg AZ31 sheets was subjected to an anisotropic plastic deformation using Hill's criterion. Each material was designed according to a different set of Lankford coefficients or R-values. This was derived from the original (No Fragmentation) VPSC model for the Rolled, 4P and 4K routes and experimental tensile R-value measurements for the 4A Route as shown in Table 6.19. The metal plates were drawn along the Longitudinal direction (L) while the Extrusion (E) and Flow (F) directions is perpendicular to the two straight edges of the metal plate in Figure 1. The off-axis directions are labelled with two different letters, EF would mean 45$^{o}$ in between E and F directions.

**Table 6.19: Lankford coefficients for all Mg AZ31 alloys studied with FEA.**

| Route | $R_E$ | $R_L$ | $R_F$ | $R_{EL}$ | $R_{EF}$ | $R_{LF}$ |
|---|---|---|---|---|---|---|
| **Rolled** | 1.37 | 0.95 | 1.56 | 0.05 | 1.37 | 33.3 |
| **4A** | 0.59 | 6.25 | 0.59 | 0.99 | 1.57 | 3.25 |
| **4P** | 0.16 | 0.14 | 0.35 | 1.06 | 0.35 | 0.38 |
| **4K** | 1.01 | 0.76 | 1.28 | 0.07 | 25.0 | 0.45 |

Fig. 6.32 shows the Equivalent plastic strain contour plots for each processed condition after cup drawing. The ECAP route 4A Mg AZ31 alloys with the lowest AED of 1.59 in Fig. 6.32 (b) shows the large warping with high strain concentrations along the edges causing the earing effect. The rolled AZ31 also shows some earing with a single region of heavy warping. Both the rolled and 4A processed material will most likely fail during cup drawing. For the higher AED conditions 4K with an AED of 2.13 has minor warping along the transition from the rim to the base which could cause some of this region to fail. The last route 4P with an AED of 3.10 shows the best results since the plastic strain transition from the rim to the bottom of the cup is gradual with no strain concentrated regions giving high promise of good drawability. FEA here proves the R-values that lead to high AED parameters do show better formability and this relationship is a feasible direct correlation.

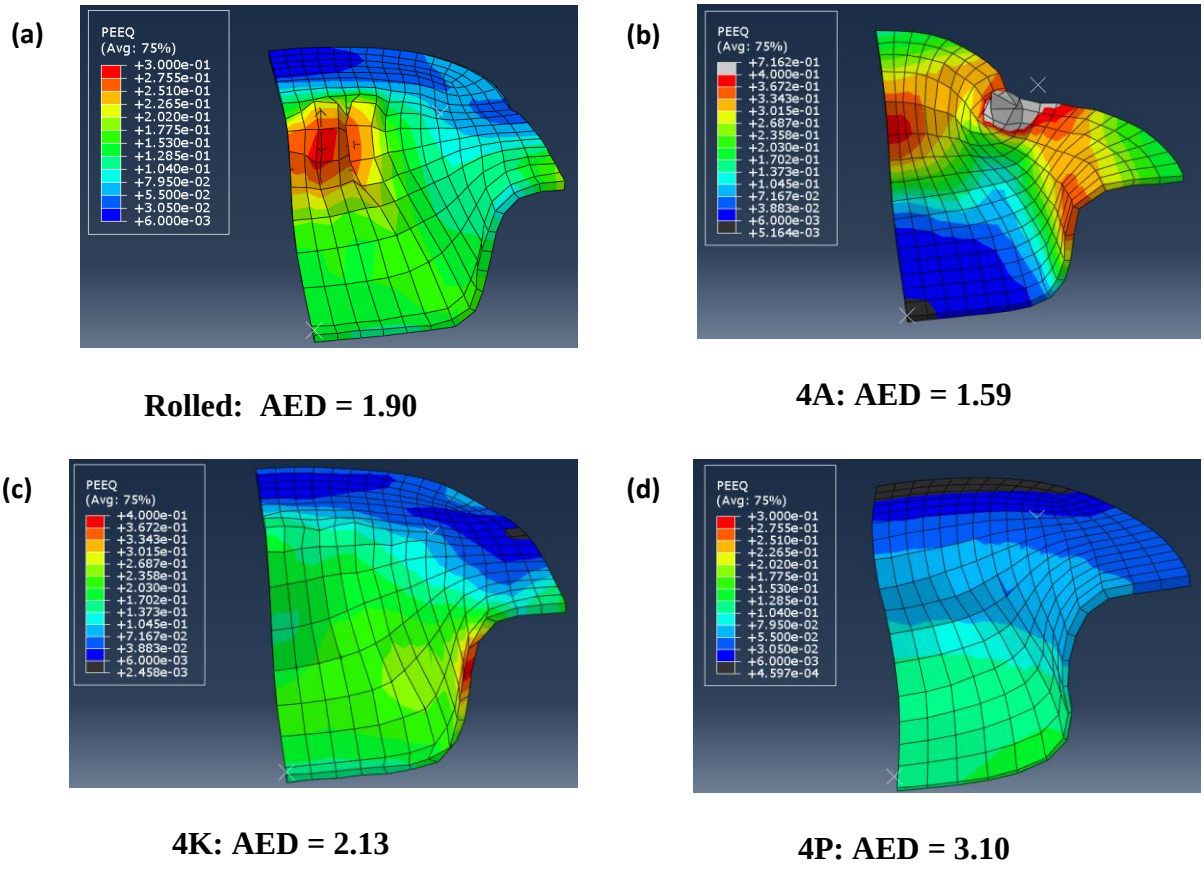


**Rolled: AED = 1.90**

**4A: AED = 1.59**

**4K: AED = 2.13**

**4P: AED = 3.10**

**Figure 6.31: Equivalent Plastic Strain contour plots for (a) Rolled, (b) 4A, (c) 4K and (d) 4P processed Mg AZ31 alloys. This shows a direct correlation of AED and forming sheet metal for Mg alloys.**

### 6.2.2 Preliminary Results for Inverse Optimization Design of Plate ECAP

A similar approach to the billet inverse optimization was taken for the ECAP plate inverse optimization problem. The only difference was the rotation direction for the plate tool was controlled along the longitudinal direction as shown in Figure . Since a basal texture is symmetric along the LD, the first rotation was omitted during the route optimization. Equation 6.12 shows the constraints for the inverse optimization model where rotation control is along only longitudinal direction. In prior chapters ECAP rotations were along the extrusion direction. Equation 6.13

shows the same objective function was used using SQP method as before. The version of VPSC crystal model used here was the original 200°C calibrated VPSC model from Chapter 3 with No Grain Fragmentation. Table 6.20 shows the initial guesses used for the optimization. The routes predicted from inverse optimization were discretized as before and 4 routes were chosen to get a distribution of AED parameters for cup drawing in experimental ECAP as shown in Table 6.21. The materials were processed but Cup drawing have not been attempted yet on those materials.

$$0.0 \leq Rot_{n\,LD} \leq 360.0\,;\;\; n = 2, 3, 4 \qquad (6.12)$$

$$Error = \left(AED_{Target} - AED_{Predicted}\right)^2 \qquad (6.13)$$

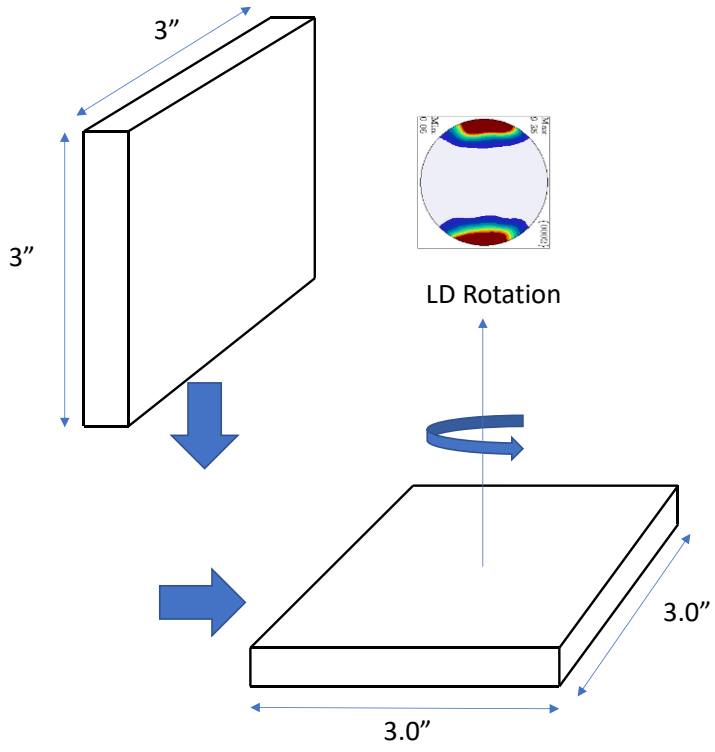


**Figure 6.32: Plate ECAP schematic of Mg AZ31 plates where Longitudinal rotation was used to design ECAP routes in the inverse optimization process**

**Table 6.20**: **Initial Guesses for LD rotation for the plate inverse optimization problem**

| Route | Rotation along LD |
|---|---|
| 4Q | **90-90-90 (Q)** |
| 4R | **90-90-90 (R)** |
| 4S | **270-270-270 (S)** |
| 4T | **180-180-180 (T)** |

**Table 6.21: Discretized routes after inverse optimization with the AED parameter for annealed and as-ECAPed conditions.**

| **Initial Conditions** | **Rot 1 (°)** | **Rot 2 (°)** | **Rot 3 (°)** | **$AED_{Sim}$ at 0.1 Plastic Strain** |
|---|---|---|---|---|
| **90-0-0** | 90 | 0 | 0 | 2.33 |
| **90-90-0** | 270 | 0 | 0 | 2.31 |
| **90-90-90 (Q)** | 90 | 90 | 90 | 2.28 |
| **90-90-90 (R)** | 90 | 180 | 180 | 2.52 |
| **270-270-270 (S)** | 270 | 180 | 270 | 2.81 |
| **180-180-180 (T)** | 270 | 270 | 90 | 3.13 |

## 6.3 Future Workflow Chart

The goal of the next 3-4 years will be the development of a more robust VPSC crystal plasticity model with built in grain size and dislocation hardening effects and recrystallization effects which will then be used to inverse optimize the AED parameter using hybrid multi step processing paths. This includes, extrusion, ECAP, rolling or even wire drawing. Each optimized

path will then be able to combine different orientations of the material at different intervals of strain under various combinations of varying processing paths, for example ECAP 2 passes at 200% strain, rolling to 90% strain and then finish with extrusion ratio of 2.5. The problem could be made more complex if a processing temperature range of 100$^{o}$C to 200$^{o}$C is considered. This will require more advanced optimization techniques to find hybrid temperature and path combinations to improve the formability of Mg alloys in an automated fashion.

Figure 6.34 shows the complete flow chart plan of the Mg formability project for the next 3-4 years which was completed with the help of Imroj Syed who will be taking over the project. Each colored region reflects a different sub project that may need to be completed before attempting the inverse optimization using hybrid processing paths. The green section on the extreme left discusses the characterization of the as received material of Mg AZ31 alloys. One generation of alloys have already been completely used and needs to be reordered for the next few years. To avoid batch to batch issues the as received material needs to be characterized again using mechanical tests at varying temperatures (25$^{o}$C to 200$^{o}$C), grain size and texture measurements. Three different geometries will be considered of the material will be considered for different uses. The Octa bar and round bar for more discretized orientation-controlled rotations and plates for sheet metal drawing with the possibility of machine cup drawing blanks from them.

The red box shows the VPSC hardening model sub project which deals with the lack of hardening in the VPSC crystal plasticity model. Out of all the voce hardening parameters, ($\tau_o$, $\tau_1$, $\theta_o$, and $\theta_1$), $\tau_o$ is the only parameter tracked and evolved in the VPSC model during processing. This prevents the VPSC model from predicting mechanical behavior accurately after high strain processing such as ECAP. In the prior sections a calibration of the voce hardening parameters were used to completely represent the Hall-Petch effect of the grain size in ECAP materials. In this case

we want to take it further by evolving $\tau_1$, $\theta_o$, and $\theta_1$ as well as $\tau_o$ within the model as a function of grain size and dislocation densities. If this could be done various processing paths can be used without the need of calibrating the voce hardening parameters after every high deformation process.

The blue box shows the recalibration of the VPSC crystal plasticity model using voce hardening parameters and multi objective optimization function. In this current study mechanical tensile test and ODF texture minimization was conducted separately to minimize the error with experimental and simulation results. Using a multi objective response the mechanical minimization and ODF minimization error functions could be combined into a single problem where only a single set of Voce hardening parameters could be derived for the rolled or extruded Mg AZ31 material. This along with the combination of the VPSC hardening model in the red subsection will mitigate a lot of recalibrations of the VPSC model in the future.

The purple box on the extreme right shows the dynamic recrystallization addition to the VPSC model. The model has already been developed by Dr. Ricardo Lebensohn and Dr. Miroslav Zecevic which uses a new set of calibration parameters (unknown at this time) to simulate microstructural dynamic recrystallization in simple materials. This has not been implemented for multi slip and twin system material such as Mg alloys as of yet. The idea of using optimization to calibrate such a model will deem necessary due to the complications of recrystallization. We understand discontinuous and continuous occurs in Mg alloys during high temperature processing and reflecting such behavior will bring us closer in predicting formability at a much higher level.

Using all the prior steps a new optimized VPSC model with recrystallization, hardening and grain fragmentation simulation tool will be developed hopefully developing into a better AED and formability predictions. In the Orange section on the bottom left, shows the AED inverse

optimization process with the added complexity of using hybrid processing paths, with combinations of ECAP, Rolling or Extrusion with material orientation control, temperature of processing and amount of strain for each processing path. This complex problem needs to solve with more advanced optimization techniques.

Finally, the last cyan box on the bottom right, shows the final experimental validation from the AED inverse optimization. This could use a set of different billet or plate types to ensure the most accurate orientation control during ECAP, rolling or extrusion predicted by the inverse optimization step. The materials will be characterized using mechanical tests, microstructural tests such SEM and EBSD, Texture characterization with XRD and finally cup drawing tests for AED dependance on formability.

# Project Flow Chart

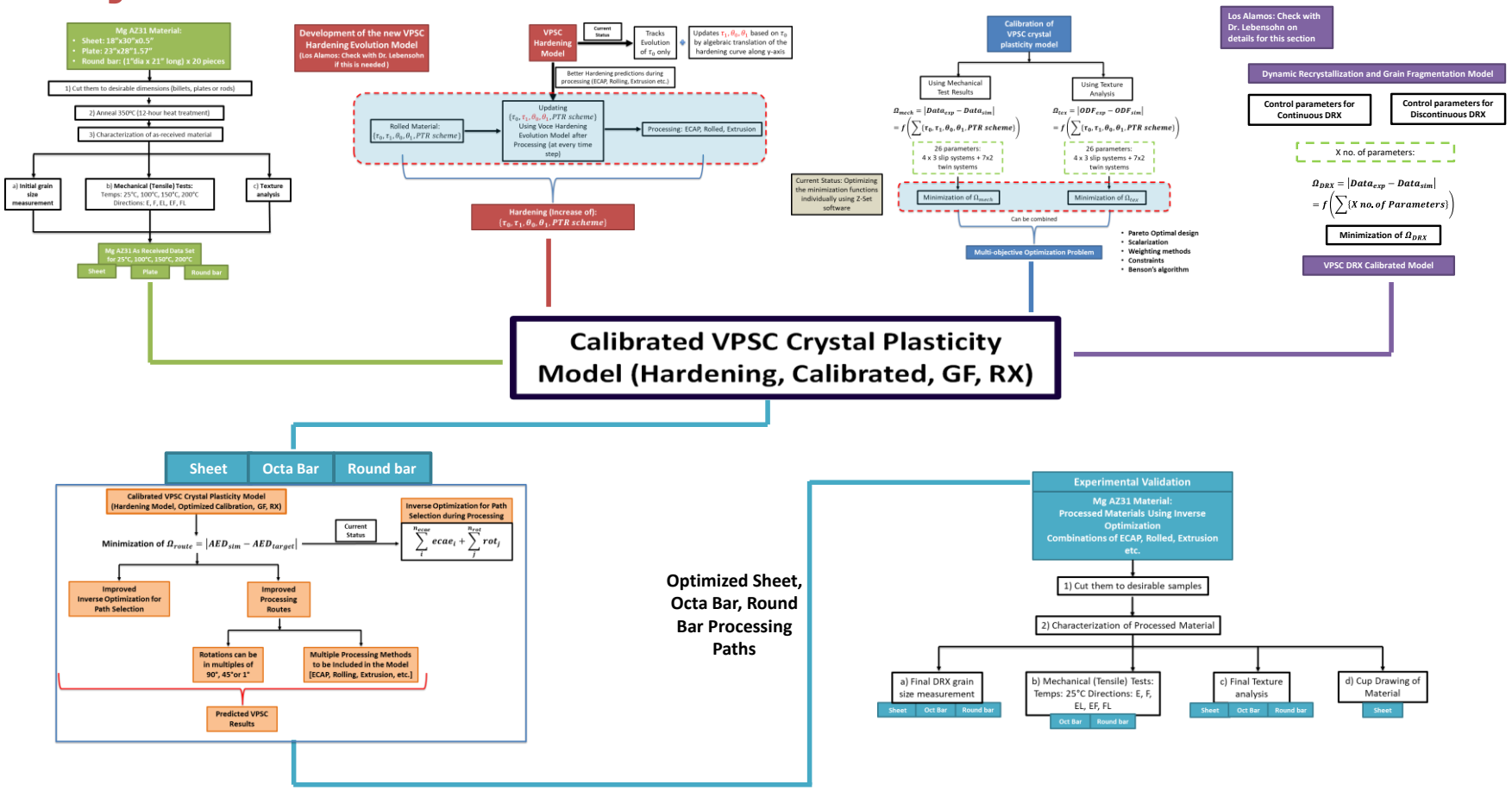


**Figure 6.33: Future workflow chart for Mg hybrid Processing paths using Inverse optimization Desi**

# VII: REFERENCES

[1] H.K. Lim, D.H. Kim, J.Y. Lee, W.T. Kim, D.H. Kim, Effects of alloying elements on microstructures and mechanical properties of wrought Mg–MM–Sn alloy, Journal of Alloys and Compounds 468(1) (2009) 308-314.

[2] H. Yan, R.S. Chen, E.H. Han, Room-temperature ductility and anisotropy of two rolled Mg–Zn–Gd alloys, Materials Science and Engineering: A 527(15) (2010) 3317-3322.

[3] X. Huang, K. Suzuki, A. Watazu, I. Shigematsu, N. Saito, Improvement of formability of Mg–Al–Zn alloy sheet at low temperatures using differential speed rolling, Journal of Alloys and Compounds 470(1) (2009) 263-268.

[4] N.J. Kim, Critical Assessment 6: Magnesium sheet alloys: viable alternatives to steels?, Materials Science and Technology 30(15) (2014) 1925-1928.

[5] Y.S. Sato, S.H.C. Park, A. Matsunaga, A. Honda, H. Kokawa, Novel production for highly formable Mg alloy plate, Journal of Materials Science 40(3) (2005) 637-642.

[6] B.-C. Suh, J.H. Kim, J.H. Hwang, M.-S. Shim, N.J. Kim, Twinning-mediated formability in Mg alloys, Scientific Reports 6(1) (2016) 22364.

[7] T.T.T. Trang, J.H. Zhang, J.H. Kim, A. Zargaran, J.H. Hwang, B.C. Suh, N.J. Kim, Designing a magnesium alloy with high strength and high formability, Nature Communications 9(1) (2018) 2522.

[8] E. Doege, K. Dröder, Sheet metal forming of magnesium wrought alloys — formability and process technology, Journal of Materials Processing Technology 115(1) (2001) 14-19.

[9] S. Yi, J. Bohlen, F. Heinemann, D. Letzig, Mechanical anisotropy and deep drawing behaviour of AZ31 and ZE10 magnesium alloy sheets, Acta Materialia 58(2) (2010) 592-605.

[10] S.R. Agnew, J.W. Senn, J.A. Horton, Mg sheet metal forming: Lessons learned from deep drawing Li and Y solid-solution alloys, JOM 58(5) (2006) 62-69.

[11] F. Klocke, Sheet Metal Forming, in: F. Klocke (Ed.), Manufacturing Processes 4: Forming, Springer Berlin Heidelberg, Berlin, Heidelberg, 2013, pp. 293-405.

[12] Y. Chino, H. Iwasaki, M. Mabuchi, Stretch formability of AZ31 Mg alloy sheets at different testing temperatures, Materials Science and Engineering: A 466(1) (2007) 90-95.

[13] W. He, Q. Zeng, H. Yu, Y. Xin, B. Luan, Q. Liu, Improving the room temperature stretch formability of a Mg alloy thin sheet by pre-twinning, Materials Science and Engineering: A 655 (2016) 1-8.

[14] N. Ogawa, M. Shiomi, K. Osakada, Forming limit of magnesium alloy at elevated temperatures for precision forging, International Journal of Machine Tools and Manufacture 42(5) (2002) 607-614.

[15] X. Huang, K. Suzuki, Y. Chino, M. Mabuchi, Influence of initial texture on cold deep drawability of Mg–3Al–1Zn alloy sheets, Materials Science and Engineering: A 565 (2013) 359-372.

[16] E. Dogan, M.W. Vaughan, S.J. Wang, I. Karaman, G. Proust, Role of starting texture and deformation modes on low-temperature shear formability and shear localization of Mg–3Al–1Zn alloy, Acta Materialia 89 (2015) 408-422.

[17] L. Jiang, J.J. Jonas, A.A. Luo, A.K. Sachdev, S. Godet, Influence of {10-12} extension twinning on the flow behavior of AZ31 Mg alloy, Materials Science and Engineering: A 445-446 (2007) 302-309.

[18] M. Knezevic, A. Levinson, R. Harris, R.K. Mishra, R.D. Doherty, S.R. Kalidindi, Deformation twinning in AZ31: Influence on strain hardening and texture evolution, Acta Materialia 58(19) (2010) 6230-6242.

[19] M.-G. Lee, R.H. Wagoner, J.K. Lee, K. Chung, H.Y. Kim, Constitutive modeling for anisotropic/asymmetric hardening behavior of magnesium alloy sheets, International Journal of Plasticity 24(4) (2008) 545-582.

[20] W. Muhammad, M. Mohammadi, J. Kang, R.K. Mishra, K. Inal, An elasto-plastic constitutive model for evolving asymmetric/anisotropic hardening behavior of AZ31B and ZEK100 magnesium alloy sheets considering monotonic and reverse loading paths, International Journal of Plasticity 70 (2015) 30-59.

[21] M.H. Yoo, Slip, twinning, and fracture in hexagonal close-packed metals, Metallurgical Transactions A 12(3) (1981) 409-418.

[22] N. Stanford, M.R. Barnett, Solute strengthening of prismatic slip, basal slip and {101¯2} twinning in Mg and Mg–Zn binary alloys, International Journal of Plasticity 47 (2013) 165-181.

[23] S. Basu, E. Dogan, B. Kondori, I. Karaman, A.A. Benzerga, Towards designing anisotropy for ductility enhancement: A theory-driven investigation in Mg-alloys, Acta Materialia 131 (2017) 349-362.

[24] K. Iwanaga, H. Tashiro, H. Okamoto, K. Shimizu, Improvement of formability from room temperature to warm temperature in AZ-31 magnesium alloy, Journal of Materials Processing Technology 155-156 (2004) 1313-1316.

[25] Z. Zeng, J.-F. Nie, S.-W. Xu, C. H. J. Davies, N. Birbilis, Super-formable pure magnesium at room temperature, Nature Communications 8(1) (2017) 972.

[26] Y. Chino, M. Mabuchi, Enhanced stretch formability of Mg–Al–Zn alloy sheets rolled at high temperature (723K), Scripta Materialia 60(6) (2009) 447-450.

[27] S.R. Agnew, Ö. Duygulu, Plastic anisotropy and the role of non-basal slip in magnesium alloy AZ31B, International Journal of Plasticity 21(6) (2005) 1161-1193.

[28] M.W. Vaughan, W. Nasim, E. Dogan, J.S. Herrington, G. Proust, A.A. Benzerga, I. Karaman, Interplay between the effects of deformation mechanisms and dynamic recrystallization on the failure of Mg-3Al-1Zn, Acta Materialia 168 (2019) 448-472.

[29] N. Li, G. Huang, X. Zhong, Q. Liu, Deformation mechanisms and dynamic recrystallization of AZ31 Mg alloy with different initial textures during hot tension, Materials & Design 50 (2013) 382-391.

[30] B. Srinivasarao, N.V. Dudamell, M.T. Pérez-Prado, Texture analysis of the effect of non-basal slip systems on the dynamic recrystallization of the Mg alloy AZ31, Materials Characterization 75 (2013) 101-107.

[31] B. Song, N. Guo, T. Liu, Q. Yang, Improvement of formability and mechanical properties of magnesium alloys via pre-twinning: A review, Materials & Design (1980-2015) 62 (2014) 352-360.

[32] D.H. Kang, D.W. Kim, S. Kim, G.T. Bae, K.H. Kim, N.J. Kim, Relationship between stretch formability and work-hardening capacity of twin-roll cast Mg alloys at room temperature, Scripta Materialia 61(7) (2009) 768-771.

[33] M. Al-Maharbi, I. Karaman, I.J. Beyerlein, D. Foley, K.T. Hartwig, L.J. Kecskes, S.N. Mathaudhu, Microstructure, crystallographic texture, and plastic anisotropy evolution in an Mg alloy during equal channel angular extrusion processing, Materials Science and Engineering: A 528(25) (2011) 7616-7627.

[34] K.C. Atli, I. Karaman, R.D. Noebe, A. Garg, Y.I. Chumlyakov, I.V. Kireeva, Shape memory characteristics of Ti49.5Ni25Pd25Sc0.5 high-temperature shape memory alloy after severe plastic deformation, Acta Materialia 59(12) (2011) 4747-4760.

[35] B. Kockar, I. Karaman, A. Kulkarni, Y. Chumlyakov, I.V. Kireeva, Effect of severe ausforming via equal channel angular extrusion on the shape memory response of a NiTi alloy, Journal of Nuclear Materials 361(2) (2007) 298-305.

[36] I. Karamn, The effect of temperature and extrusion speed on the consolidation of Zirconium-based metallic glass powder using Equal-Channel Angular Extrusion, Metall. Mater. Trans. A 35(1) (2004) 247-256.

[37] S.R. Agnew, J.A. Horton, T.M. Lillo, D.W. Brown, Enhanced ductility in strongly textured magnesium produced by equal channel angular processing, Scripta Materialia 50(3) (2004) 377-381.

[38] V.M. Segal, Equal channel angular extrusion: from macromechanics to structure formation, Materials Science and Engineering: A 271(1) (1999) 322-333.

[39] R.Z. Valiev, T.G. Langdon, Principles of equal-channel angular pressing as a processing tool for grain refinement, Progress in Materials Science 51(7) (2006) 881-981.

[40] Y. Iwahashi, Z. Horita, M. Nemoto, J. Wang, T.G. Langdon, Principle of equal-channel angular pressing for the processing of ultra-fine grained materials, (1996).

[41] H.S. Kim, Finite element analysis of equal channel angular pressing using a round corner die, Materials Science and Engineering: A 315(1) (2001) 122-128.

[42] I.J. Beyerlein, L.S. Tóth, Texture evolution in equal-channel angular extrusion, Progress in Materials Science 54(4) (2009) 427-510.

[43] W.J. Kim, C.W. An, Y.S. Kim, S.I. Hong, Mechanical properties and microstructures of an AZ61 Mg Alloy produced by equal channel angular pressing, Scripta Materialia 47(1) (2002) 39-44.

[44] S. Basu, E. Dogan, B. Kondori, I. Karaman, A.A. Benzerga, Ductility Enhancement in Mg Alloys by Anisotropy Engineering, in: K.N. Solanki, D. Orlov, A. Singh, N.R. Neelameggham (Eds.) Magnesium Technology 2017, Springer International Publishing, Cham, 2017, pp. 153-158.

[45] K. Xia, J.T. Wang, X. Wu, G. Chen, M. Gurvan, Equal channel angular pressing of magnesium alloy AZ31, Materials Science and Engineering: A 410-411 (2005) 324-327.

[46] D.H. Shin, B.C. Kim, Y.-S. Kim, K.-T. Park, Microstructural evolution in a commercial low carbon steel by equal channel angular pressing, Acta Materialia 48(9) (2000) 2247-2255.

[47] F. Dalla Torre, R. Lapovok, J. Sandlin, P.F. Thomson, C.H.J. Davies, E.V. Pereloma, Microstructures and properties of copper processed by equal channel angular extrusion for 1–16 passes, Acta Materialia 52(16) (2004) 4819-4832.

[48] D.H. Shin, I. Kim, J. Kim, Y.S. Kim, S.L. Semiatin, Microstructure development during equal-channel angular pressing of titanium, Acta Materialia 51(4) (2003) 983-996.

[49] D. Song, A. Ma, J. Jiang, P. Lin, D. Yang, J. Fan, Corrosion behavior of equal-channel-angular-pressed pure magnesium in NaCl aqueous solution, Corrosion Science 52(2) (2010) 481-490.

[50] H. Watanabe, T. Mukai, K. Ishikawa, K. Higashi, Low temperature superplasticity of a fine-grained ZK60 magnesium alloy processed by equal-channel-angular extrusion, Scripta Materialia 46(12) (2002) 851-856.

[51] R.Y. Lapovok, The role of back-pressure in equal channel angular extrusion, Journal of Materials Science 40(2) (2005) 341-346.

[52] W.J. Kim, S.I. Hong, Y.S. Kim, S.H. Min, H.T. Jeong, J.D. Lee, Texture development and its effect on mechanical properties of an AZ61 Mg alloy fabricated by equal channel angular pressing, Acta Materialia 51(11) (2003) 3293-3307.

[53] A. Chatterjee, G. Sharma, A. Sarkar, J.B. Singh, J.K. Chakravartty, A study on cryogenic temperature ECAP on the microstructure and mechanical properties of Al–Mg alloy, Materials Science and Engineering: A 556 (2012) 653-657.

[54] L.B. Tong, M.Y. Zheng, X.S. Hu, K. Wu, S.W. Xu, S. Kamado, Y. Kojima, Influence of ECAP routes on microstructure and mechanical properties of Mg–Zn–Ca alloy, Materials Science and Engineering: A 527(16) (2010) 4250-4256.

[55] J. Suh, J. Victoria-Hernández, D. Letzig, R. Golle, W. Volk, Effect of processing route on texture and cold formability of AZ31 Mg alloy sheets processed by ECAP, Materials Science and Engineering: A 669 (2016) 159-170.

[56] M. Janeček, M. Popov, M.G. Krieger, R.J. Hellmig, Y. Estrin, Mechanical properties and microstructure of a Mg alloy AZ31 prepared by equal-channel angular pressing, Materials Science and Engineering: A 462(1) (2007) 116-120.

[57] K.-T. Park, H.-J. Lee, C.S. Lee, D.H. Shin, Effect of post-rolling after ECAP on deformation behavior of ECAPed commercial Al–Mg alloy at 723K, Materials Science and Engineering: A 393(1) (2005) 118-124.

[58] E. Dogan, I. Karaman, G. Ayoub, G. Kridli, Reduction in tension–compression asymmetry via grain refinement and texture design in Mg–3Al–1Zn sheets, Materials Science and Engineering: A 610 (2014) 220-227.

[59] A. Ma, J. Jiang, N. Saito, I. Shigematsu, Y. Yuan, D. Yang, Y. Nishida, Improving both strength and ductility of a Mg alloy through a large number of ECAP passes, Materials Science and Engineering: A 513-514 (2009) 122-127.

[60] H.K. Lin, J.C. Huang, T.G. Langdon, Relationship between texture and low temperature superplasticity in an extruded AZ31 Mg alloy processed by ECAP, Materials Science and Engineering: A 402(1) (2005) 250-257.

[61] R.B. Figueiredo, P.R. Cetlin, T.G. Langdon, The processing of difficult-to-work alloys by ECAP with an emphasis on magnesium alloys, Acta Materialia 55(14) (2007) 4769-4779.

[62] Y. Yuan, A. Ma, X. Gou, J. Jiang, F. Lu, D. Song, Y. Zhu, Superior mechanical properties of ZK60 mg alloy processed by equal channel angular pressing and rolling, Materials Science and Engineering: A 630 (2015) 45-50.

[63] D.C. Foley, M. Al-Maharbi, K.T. Hartwig, I. Karaman, L.J. Kecskes, S.N. Mathaudhu, Grain refinement vs. crystallographic texture: Mechanical anisotropy in a magnesium alloy, Scripta Materialia 64(2) (2011) 193-196.

[64] S.X. Ding, W.T. Lee, C.P. Chang, L.W. Chang, P.W. Kao, Improvement of strength of magnesium alloy processed by equal channel angular extrusion, Scripta Materialia 59(9) (2008) 1006-1009.

[65] S.M. Razavi, D.C. Foley, I. Karaman, K.T. Hartwig, O. Duygulu, L.J. Kecskes, S.N. Mathaudhu, V.H. Hammond, Effect of grain size on prismatic slip in Mg–3Al–1Zn alloy, Scripta Materialia 67(5) (2012) 439-442.

[66] R.B. Figueiredo, T.G. Langdon, Grain refinement and mechanical behavior of a magnesium alloy processed by ECAP, Journal of Materials Science 45(17) (2010) 4827-4836.

[67] R.A. Lebensohn, C.N. Tomé, A self-consistent anisotropic approach for the simulation of plastic deformation and texture development of polycrystals: Application to zirconium alloys, Acta Metallurgica et Materialia 41(9) (1993) 2611-2624.

[68] C.N. Tomé, R.A. Lebensohn, U.F. Kocks, A model for texture development dominated by deformation twinning: Application to zirconium alloys, Acta Metallurgica et Materialia 39(11) (1991) 2667-2680.

[69] R.A. Lebensohn, C.N. Tomé, A study of the stress state associated with twin nucleation and propagation in anisotropic materials, Philosophical Magazine A 67(1) (1993) 187-206.

[70] S.H. Choi, E.J. Shin, B.S. Seong, Simulation of deformation twins and deformation texture in an AZ31 Mg alloy under uniaxial compression, Acta Materialia 55(12) (2007) 4181-4192.

[71] G. Proust, C.N. Tomé, A. Jain, S.R. Agnew, Modeling the effect of twinning and detwinning during strain-path changes of magnesium alloy AZ31, International Journal of Plasticity 25(5) (2009) 861-880.

[72] T. Walde, H. Riedel, Modeling texture evolution during hot rolling of magnesium alloy AZ31, Materials Science and Engineering: A 443(1) (2007) 277-284.

[73] A. Ostapovets, P. Molnár, A. Jäger, Visco-plastic self-consistent modelling of a grain boundary misorientation distribution after equal-channel angular pressing in an AZ31 magnesium alloy, Journal of Materials Science 48(5) (2013) 2123-2134.

[74] T. Walde, H. Riedel, Simulation of earing during deep drawing of magnesium alloy AZ31, Acta Materialia 55(3) (2007) 867-874.

[75] A. Jain, S.R. Agnew, Modeling the temperature dependent effect of twinning on the behavior of magnesium alloy AZ31B sheet, Materials Science and Engineering: A 462(1) (2007) 29-36.

[76] W. Nasim, J.S. Herrington, A.A. Benzerga, J. Wang, I. Karaman, Inverse Optimization to Design Processing Paths to Tailor Formability of Mg Alloys, in: V.V. Joshi, J.B. Jordon, D. Orlov, N.R. Neelameggham (Eds.) Magnesium Technology 2019, Springer International Publishing, Cham, 2019, pp. 239-246.

[77] I. Karaman, H. Sehitoglu, A.J. Beaudoin, Y.I. Chumlyakov, H.J. Maier, C.N. Tomé, Modeling the deformation behavior of Hadfield steel single and polycrystals due to twinning and slip, Acta Materialia 48(9) (2000) 2031-2047.

[78] W. Wen, M. Borodachenkova, C.N. Tomé, G. Vincze, E.F. Rauch, F. Barlat, J.J. Grácio, Mechanical behavior of Mg subjected to strain path changes: Experiments and modeling, International Journal of Plasticity 73 (2015) 171-183.

[79] I.J. Beyerlein, R.A. Lebensohn, C.N. Tomé, Modeling texture and microstructural evolution in the equal channel angular extrusion process, Materials Science and Engineering: A 345(1) (2003) 122-138.

[80] I.J. Beyerlein, C.N. Tomé, A dislocation-based constitutive law for pure Zr including temperature effects, International Journal of Plasticity 24(5) (2008) 867-895.

[81] A.L. Oppedal, H. El Kadiri, C.N. Tomé, S.C. Vogel, M.F. Horstemeyer, Anisotropy in hexagonal close-packed structures: improvements to crystal plasticity approaches applied to magnesium alloy, Philosophical Magazine 93(35) (2013) 4311-4330.

[82] M. Zecevic, R.A. Lebensohn, R.J. McCabe, M. Knezevic, Modelling recrystallization textures driven by intragranular fluctuations implemented in the viscoplastic self-consistent formulation, Acta Materialia 164 (2019) 530-546.

[83] R.A. Lebensohn, M. Zecevic, M. Knezevic, R.J. McCabe, Average intragranular misorientation trends in polycrystalline materials predicted by a viscoplastic self-consistent approach, Acta Materialia 104 (2016) 228-236.

[84] A.V. Hershey, The elascitiy of an isoptrpic aggregate of anisotropic cubic crystals, Journal of Applied Mechanics 21 (1954) 236-240.

[85] A. Yamashita, D. Yamaguchi, Z. Horita, T.G. Langdon, Influence of pressing temperature on microstructural development in equal-channel angular pressing, Materials Science and Engineering: A 287(1) (2000) 100-106.

[86] M. Bobeth, G. Diener, Static elastic and thermoelastic field fluctuations in multiphase composites, Journal of the Mechanics and Physics of Solids 35(2) (1987) 137-149.

[87] P. Ponte Castañeda, Second-order homogenization estimates for nonlinear composites incorporating field fluctuations: I—theory, Journal of the Mechanics and Physics of Solids 50(4) (2002) 737-757.

[88] R.A. Lebensohn, Y. Liu, P. Ponte Castañeda, On the accuracy of the self-consistent approximation for polycrystals: comparison with full-field numerical simulations, Acta Materialia 52(18) (2004) 5347-5361.

[89] M.A. Meyers, O. Vöhringer, V.A. Lubarda, The onset of twinning in metals: a constitutive description, Acta Materialia 49(19) (2001) 4025-4039.

[90] M. Zecevic, W. Pantleon, R.A. Lebensohn, R.J. McCabe, M. Knezevic, Predicting intragranular misorientation distributions in polycrystalline metals using the viscoplastic self-consistent formulation, Acta Materialia 140 (2017) 398-410.

[91] C. Tome, R.A. Lebensohn, Manual for Code Visco-Plastic Self-Consistent (VPSC), (2009).

[92] S.M. Keralavarma, A.A. Benzerga, An approximate yield criterion for anisotropic porous media, Comptes Rendus Mécanique 336(9) (2008) 685-692.

[93] A.A. Benzerga, J. Besson, A. Pineau, Coalescence-Controlled Anisotropic Ductile Fracture, Journal of Engineering Materials and Technology 121(2) (1999) 221-229.

[94] R. Hill, A theory of yielding and plastic flow of anisotropic solids, Proc. R. Soc. Lond. A(193) (1948) 281-297.

[95] A.A. Benzerga, J. Besson, Plastic potentials for anisotropic porous solids, European Journal of Mechanics - A/Solids 20(3) (2001) 397-434.

[96] V. Herrera-Solaz, J. Llorca, E. Dogan, I. Karaman, J. Segurado, An inverse optimization strategy to determine single crystal mechanical behavior from polycrystal tests: Application to AZ31 Mg alloy, International Journal of Plasticity 57 (2014) 1-15.

[97] B.H. Lee, S.H. Park, S.-G. Hong, K.-T. Park, C.S. Lee, Role of initial texture on the plastic anisotropy of Mg–3Al–1Zn alloy at various temperatures, Materials Science and Engineering: A 528(3) (2011) 1162-1172.

[98] H. Somekawa, A. Kinoshita, A. Kato, Effect of alloying elements on room temperature stretch formability in Mg alloys, Materials Science and Engineering: A 732 (2018) 21-28.

[99] G. Proust, C.N. Tomé, G.C. Kaschner, Modeling texture, twinning and hardening evolution during deformation of hexagonal materials, Acta Materialia 55(6) (2007) 2137-2148.

[100] Armines and Onera The French Aerospace Lab, Zset Non-Linear Material and Structure Analysis Suite, http://www.zset-software.com/ (2020).

[101] P.T. Boggs, J.W. Tolle, Sequential Quadratic Programming, Acta Numerica 4 (1995) 1-51.

[102] H.S. Kim, M.H. Seo, S.I. Hong, On the die corner gap formation in equal channel angular pressing, Materials Science and Engineering: A 291(1) (2000) 86-90.

[103] H.S. Kim, M.H. Seo, S.I. Hong, Plastic deformation analysis of metals during equal channel angular pressing, Journal of Materials Processing Technology 113(1) (2001) 622-626.

[104] C.W. Su, L. Lu, M.O. Lai, Mechanical behaviour and texture of annealed AZ31 Mg alloy deformed by ECAP, Materials Science and Technology 23(3) (2007) 290-296.

[105] B. Selvarajou, S.P. Joshi, A.A. Benzerga, Void growth and coalescence in hexagonal close packed crystals, Journal of the Mechanics and Physics of Solids 125 (2019) 198-224.